



# DISSERTATION

## Detection of weak magnetic fields: The TMR fluxgate sensing technology and its limits

Ausgeführt zum Zwecke der Erlangung des akademischen  
Grades einer  
Doktorin der technischen Wissenschaften

unter der Leitung von  
Priv.-Doz. Dr. techn. Dieter Süss  
Institut für Festkörperphysik - E138  
eingereicht an der Technischen Universität Wien  
Fakultät für Physik  
von

**DI Leoni Breth**

Matrikelnummer 0325410

Chimanistraße 34/5  
1190 Wien

Gutachter:

\_\_\_\_\_  
Priv.-Doz. Dr. techn. Dieter Süss

\_\_\_\_\_  
Prof. Dr. Andreas Hütten

Wien, am 20.10.2016

\_\_\_\_\_  
Kandidatin

# Erklärung zur Verfassung der Arbeit

DI Leoni Breth  
Chimanistraße 34/5, 1190 Wien

Hiermit erkläre ich, dass ich diese Arbeit selbstständig verfasst habe, dass ich die verwendeten Quellen und Hilfsmittel vollständig angegeben habe und dass ich die Stellen der Arbeit einschließlich Tabellen, Karten und Abbildungen, die anderen Werken oder dem Internet im Wortlaut oder dem Sinn nach entnommen sind, auf jeden Fall unter Angabe der Quelle als Entlehnung kenntlich gemacht habe.

---

Ort, Datum

---

DI Leoni Breth

*Now I'm lookin' to the sky to save me,  
Lookin' for a sign of life,  
Lookin' for something to help me burn out bright.  
I'm lookin' for a complication,  
Lookin' 'cause I'm tired of lyin',  
Make my way back home when I learn to fly high.*

*(Foo Fighters)*

# Kurzfassung

Tunnelmagnetowiderstandstands-Sensoren (*tunneling magnetoresistance* - TMR) findet man sich heute in einer Reihe technischer Anwendungen, wobei Leseköpfe in modernen Festplattenlaufwerken das wohl prominenteste Beispiel darstellen. TMR-Sensoren bestehen aus einem Stapel dünner Schichten magnetischer und nicht-magnetischer Materialien, wobei der magnetische Tunnelkontakt selbst aus zwei magnetischen Schichten aufgebaut ist, die durch eine isolierende Schicht von nur einigen Nanometern voneinander getrennt sind. TMR-Sensoren weisen einen hohen Magnetowiderstandseffekt auf, ihr Widerstand ist also für die parallele Ausrichtung der Magnetisierungen in den beiden Schichten deutlich niedriger als für antiparallele Ausrichtung. Zur Zeit ist es leider nicht möglich, sehr schwache Magnetfelder im niederfrequenten Bereich mit konventionellen TMR-Sensoren zu messen, da diese ausgeprägtes intrinsisches  $1/f$ -Rauschen aufweisen. Dieser Umstand verhindert aktuell, dass TMR-Sensoren - trotz ihrer erwiesenen Tauglichkeit für kostengünstige Massenproduktion - für biomedizinische Anwendungen eingesetzt werden können, da hier Detektivitäten von nur einigen Pico-Tesla/ $\sqrt{\text{Hz}}$  erforderlich sind. Aus diesem Grund ist dieser Markt von SQUID-Sensoren (*Superconducting Quantum Interference Devices* - SQUID) beherrscht, welche allerdings technisch aufwändige Kühlung mit flüssigem Stickstoff oder sogar Helium für ihre Funktionsweise benötigen.

In dieser Arbeit wird eine neuartige Sensortechnologie im Hinblick auf ihre Fähigkeit untersucht, schwache Magnetfelder im Pico-Tesla-Bereich zu messen. Sie basiert auf einem magnetischen Tunnelkontakt, welcher nach dem Prinzip des Fluxgate-Magnetometers betrieben wird, indem zusätzlich zum zu messenden Feld ein magnetisches Wechselfeld angelegt wird, welches den Kontakt periodisch in Sättigung treibt. Der Umfang dieser Arbeit umfasst die Herstellung mikrostrukturierter TMR-Fluxgate-Sensoren durch Sputterdeposition und Standardmethoden der optischen Lithographie sowie den Aufbau eines Messsystems, um die Funktionsweise des Fluxgate-Messprinzips an einem magnetischen Tunnelkontakt zu verifizieren. Mittels der Messung der zweiten Harmonischen der Tunnelkontaktspannung mit einem Lock-In-Verstärker wurden Sensorkennlinien aufgezeichnet. Es konnte bei der Untersuchung des Signals des periodisch schaltenden magnetischen Tunnelkontaktes im Zeitbereich festgestellt werden, dass sich das Schaltverhalten bei Anlegen eines kleinen Stabilisierungsfeldes entlang der harten Achse deutlich verbesserte und

das Rauschniveau im Vergleich zum Betrieb ohne Stabilisierungsfeld herabgesetzt werden konnte.

Um das Detektionslimit der TMR-Fluxgate-Sensortechnologie abzuschätzen, wurde ein theoretisches Modell entwickelt, welches sich auf das thermisch aktivierte Schalten über Energiebarrieren von Eindomänen-Teilchen mit uniaxialer Anisotropie stützt. Dadurch wird das periodische Ummagnetisieren der freien Schicht im magnetischen Tunnelkontakt beschrieben. Thermische Fluktuationen sind ein wesentlicher Grund für die Abhängigkeit des Koerzitivfeldes von der Feldrate und es wird in dieser Arbeit gezeigt, dass dies zu der Entstehung einer statistischen Verteilung von Schaltfeldern führt, wenn mehrere Schaltzyklen beobachtet werden. Diese Schaltfeldverteilung wurde analytisch abgeleitet durch Lösen der Master-Gleichung für die zeitliche Entwicklung der Schaltwahrscheinlichkeit des Teilchens, wenn ein der aktuellen Magnetisierung entgegengesetztes Feld entlang der leichten Achse angelegt wird. Darüberhinaus wurde eine Monte-Carlo-Simulation programmiert, mit welcher eine Schaltfeldverteilung in Übereinstimmung mit dem analytischen Ergebnis erzeugt werden konnte. Die Simulation wurde auch genutzt, um das TMR-Fluxgate-Sensorsignal im Zeitbereich zu erzeugen. Durch gemeinsame Auswertung der Simulationsergebnisse und der experimentellen Daten mithilfe digitaler Signalverarbeitungsmethoden konnte ein unteres Limit für die Detektivität der getesteten Sensoren in der Größenordnung von  $100 \text{ nT}/\sqrt{\text{Hz}}$  ermittelt werden.

# Abstract

Tunneling magnetoresistance (TMR) sensors are nowadays widely used in applications such as read heads in modern hard disk drives, which is probably the most prominent example. TMR sensors consist of a thin film sandwich of magnetic and non-magnetic materials, in which the active junction region - the magnetic tunnel junction (MTJ) - is formed by two magnetic layers separated by an insulating barrier of only a few nanometers. TMR sensors have a large magnetoresistance effect, which means that their resistance is considerably lower when the magnetizations of the two layers in the MTJ are aligned parallel as compared to the antiparallel state. Unfortunately, at present conventional TMR sensors lack the capability to detect very weak magnetic fields in the low frequency range because of their intrinsic  $1/f$ -noise. This prevents TMR sensors, despite their compatibility with cheap mass production processes, from being used in biomedical applications such as magnetocardiography, where detectivities of only several pico-Tesla/ $\sqrt{\text{Hz}}$  are required. Hence, this market is dominated by sensors based on Superconducting Quantum Interference Devices (SQUIDs), which need sophisticated cooling technology with liquid nitrogen or helium for their operation.

In this thesis, a novel sensing technology based on a MTJ and the measurement technique of the fluxgate magnetometer is investigated with regard to its ability to detect weak magnetic fields in the pico-Tesla range. Additionally to the field to be measured, an alternating magnetic field is applied to the MTJ, so that it is periodically driven to saturation. The scope of the thesis covers the fabrication of microstructured TMR-fluxgate sensors using thin film sputter deposition and standard photolithographic patterning methods as well as the design of a measurement setup to test the operation of the fluxgate measurement principle on a MTJ. Sensor characteristics were measured by detecting the second-harmonic voltage with a lock-in amplifier. By investigating the time-domain switching signal of the MTJ it was found that a small bias field applied along the hard axis stabilized the switching and led to a reduced noise level as compared to switching along the easy axis without a bias field.

To estimate the detection limit of the TMR fluxgate sensing technology a theoretical model was developed, which is based on the thermally activated switching of a single domain particle with uniaxial anisotropy over an energy barrier. This represents

the periodic reversal of the free layer of the MTJ. Thermal fluctuations are a known reason for the field rate dependence of the coercivity of magnetic materials and it is shown in this work that this leads to a distribution of switching fields, when several switching cycles are observed. The switching field distribution was derived analytically by solving the master equation for the time evolution of the switching probability, when an opposing easy axis field is applied. Furthermore, a Monte Carlo simulation was programmed, which yielded a switching field distribution that coincides well with the analytical model and was also used to simulate the TMR fluxgate time domain signal. By evaluating the simulation data together with experimental time domain data using digital signal processing techniques, a lower limit for the detectivity in the order of  $100 \text{ nT}/\sqrt{\text{Hz}}$  was found.

# Contents

<b>1</b>	<b>Introduction</b>	<b>1</b>
<b>2</b>	<b>Detection of magnetic fields</b>	<b>3</b>
2.1	Noise in magnetic field sensors . . . . .	4
2.1.1	The fluctuation-dissipation theorem . . . . .	6
2.1.2	Electronic noise . . . . .	7
2.1.3	Magnetic noise . . . . .	13
2.2	SQUIDs . . . . .	15
2.2.1	Flux quantization in a superconducting ring . . . . .	15
2.2.2	The Josephson junction . . . . .	16
2.2.3	DC SQUID . . . . .	17
2.3	Fluxgate sensors . . . . .	18
2.4	Magnetoresistance sensors . . . . .	21
2.4.1	Anisotropic magnetoresistance . . . . .	22
2.4.2	Giant magnetoresistance . . . . .	24
2.4.3	Tunneling magnetoresistance . . . . .	26
<b>3</b>	<b>Motivation</b>	<b>30</b>
3.1	Biomagnetism . . . . .	30
3.2	The tunneling magnetoresistance fluxgate magnetometer . . . . .	34
<b>4</b>	<b>Theoretical Modeling</b>	<b>38</b>
4.1	The Stoner-Wohlfarth model . . . . .	39
4.2	Thermally activated magnetization switching . . . . .	45
4.2.1	Field-rate dependent coercivity . . . . .	48
4.2.2	Derivation of a thermal switching field distribution . . . . .	50
4.2.3	Properties of the switching field distribution . . . . .	52
4.2.4	Consideration of the field dependence in the attempt frequency . . . . .	57
4.3	Monte Carlo Simulation . . . . .	59
4.3.1	Thermodynamic background . . . . .	60
4.3.2	Implementation . . . . .	61
4.3.3	Results . . . . .	65



<b>5</b>	<b>Methods</b>	<b>68</b>
5.1	Fabrication techniques . . . . .	68
5.1.1	Sputter deposition . . . . .	69
5.1.2	Ion beam etching . . . . .	69
5.1.3	Plasma Enhanced Chemical Vapor Deposition . . . . .	70
5.1.4	Reactive ion etching . . . . .	70
5.1.5	Photolithography process . . . . .	71
5.2	Digital Signal Processing . . . . .	82
5.2.1	Discrete Fourier Transformation . . . . .	82
5.2.2	Laplace and Z-Transformation . . . . .	83
5.2.3	Zeropadding . . . . .	85
5.2.4	Window functions . . . . .	86
5.2.5	Aliasing . . . . .	88
5.3	Measurement Setup . . . . .	89
5.3.1	Magnetoresistance measurements . . . . .	90
5.3.2	I-V measurements . . . . .	97
5.4	Fluxgate operation mode measurements . . . . .	100
5.4.1	Dynamic magnetoresistance loops . . . . .	101
5.4.2	Sensor characteristics . . . . .	104
<b>6</b>	<b>Discussion of Results</b>	<b>108</b>
6.1	Estimation of the detection limit . . . . .	111
<b>7</b>	<b>Outlook and Conclusion</b>	<b>113</b>
	<b>Appendices</b>	<b>116</b>
<b>A</b>	<b>Theory</b>	<b>117</b>
A.1	Derivation of the Stoner-Wohlfarth astroid . . . . .	117
A.2	Derivation of the switching field distribution with field-dependent attempt frequency . . . . .	117
A.3	Monte Carlo Simulation Code . . . . .	118
<b>B</b>	<b>Fabrication details</b>	<b>121</b>
B.1	Photolithography Mask . . . . .	121
B.2	Sputter parameters . . . . .	122
B.3	IBE Settings . . . . .	123
	<b>Bibliography</b>	<b>124</b>

# Introduction

Almost sixty years have passed since Richard Feynman's famous speech entitled "There's plenty of room at the Bottom", which he gave at Caltech in 1959. This speech is considered to be the first publicly announced vision of a research area which is nowadays known as nanotechnology. While Feynman originally addressed the possibility of manipulating single atoms to assemble nanometer (nm) scale machines and devices in a "bottom-up" approach, nanotechnology in today's scientific understanding more generally covers phenomena that occur in chemical, biological and physical systems due to their reduced dimensionality. Ever since then, a vast amount of innovations has emerged reaching from profane things such as sunblockers using nanoparticles that absorb ultraviolet radiation to the scanning tunneling microscope developed at the IBM labs in Zurich, which can indeed be used to move around single atoms.

Modern integrated circuits are assembled from devices comprising thin films of a variety of materials and are another omnipresent technology that uses the physical properties originating from film thicknesses in the nm-range. On this scale, the device characteristics become largely dominated by the interfaces between the materials. Magnetoresistive sensing elements make use of the effects that only become relevant when their constituting materials are present as thin films consisting only of a small number of atomic monolayers. Giant and tunneling magnetoresistance (GMR/TMR) sensors are prominent examples for advanced nanotechnology finding their way into consumer products such as wheel speed sensors in cars, read heads in hard disk drives and compasses in cell phones. They are used in these applications to measure magnetic fields originating from the gear wheel, the magnetic recording medium or the earth in the micro- to milli-Tesla range. However, they have not entered the market for medical diagnostics of the human heart or brain yet, which probe fields in the pico- or even femto-Tesla range. This has only been achieved so far with SQUID (Superconducting Quantum Interference Device) sensors and hence this technology is the method of choice for applications such as magnetocardio- (MCG) or magnetoencephalography, in which the biomagnetic fields originating from neural activity are measured.

The main disadvantage of SQUIDs with respect to GMR/TMR sensors is that they cannot be operated at room temperature, because the superconducting sensing element of the SQUID - the Josephson junction - only works at low temperatures, which requires cooling with liquid nitrogen or even helium. This makes SQUIDs unsuitable for the production of cheap, easy-to-use and portable devices that could

be installed and operated by non-expert personnel. Therefore, diagnostic methods such as MCG remain restricted in their availability despite their proven clinical relevance especially for prenatal diagnostics. For monitoring of the fetal heartbeat MCG outperforms standard electrocardiography (ECG) due to the shielding of the electrical potentials by the human body, which is less pronounced for MCG.

In this thesis, the possibility of reaching pico-Tesla (pT) resolution with a room temperature sensing technology based on the TMR effect and the measurement principle of the fluxgate magnetometer will be explored. The fact that fields down to the pT range cannot be measured at present with magnetoresistance sensors is due to their intrinsic high noise levels. In Chapter 2 the origins of the noise sources in thin film magnetic sensors will be discussed as well as the most relevant sensing technologies for the low-field and low-frequency regime. To overcome the limitations of magnetoresistive sensors at low frequencies the idea presented in this thesis is to apply the fluxgate measurement method to a magnetic tunnel junction, which permits the measurement of DC fields at higher carrier frequencies and reduced bandwidth. The measurement principle of the TMR fluxgate and MCG, which is the motivating application, are the subject of Chapter 3.

In order to determine a theoretical detection limit of the TMR fluxgate sensor it will be investigated in Chapter 4 how thermal fluctuations affect the measurement principle. Starting from the Stoner-Wohlfarth model, stochasticity will be introduced within a transition state theory framework, which allows to derive a distribution that determines the minimum detectable field.

Chapter 5 covers the methods used for experimental fabrication of TMR fluxgate sensors as well as for data analysis. The characterization of the magnetic tunnel junctions that form the sensing element of the TMR fluxgate is discussed as well as the lithography process. Furthermore, the data analysis methods which are necessary to evaluate the TMR fluxgate signals and to determine the noise level are presented. In Chapter 6 the results from Chapters 4 and 5 are interpreted in order to derive a detection limit for the TMR fluxgate sensor.

## Detection of magnetic fields

In this chapter, we will introduce the sensing technologies for the detection of magnetic fields as well as the theoretical background of noise sources in solid state devices in general. Within the framework of this thesis the focus is on the low-field regime reaching down to field strengths of only several femto-Tesla (fT). Such weak fields occur for example as the result of neural activity in the human brain or heart (see Sec. 3.1). In Sec. 2.1 we will first introduce a quantity, that is used to compare the capability of several sensors technologies to measure a certain field - the detectivity. This quantity gives the field noise of the sensor within a certain bandwidth and allows a comparison of different sensing technologies independently of their measurement bandwidths. In Tab. 2.1 we give an overview on the detectivities of the sensing technologies discussed later on in this chapter. Without further going into detail here, this gives a first impression of their performance: Superconducting Quantum Interference Devices (SQUIDs) are the only available sensing technology at present, that can measure down to the fT-range. However, SQUIDs have to be operated at low temperatures (low- $T_C$ -SQUIDs at 4.2 K and high- $T_C$  SQUIDs at 77 K) and are therefore limited in their versatility and portability. The SQUID sensing technology will be discussed in Sec. 2.2. Fluxgate sensors are a well-known and robust technology, that can operate at room temperature down to the pT-regime (Sec. 2.3). Their main drawback is their performance degradation when they are to be integrated with standard CMOS fabrication technology. If compromises can be made regarding the sensitivity and power consumption and cost per part is the bigger issue, thin film magnetoresistance sensors are the technology of choice. Sensors based on anisotropic magnetoresistance (AMR) outperform giant and tunneling magnetoresistance (GMR and TMR) sensors in their detectivity at present, because despite the fact that GMR and TMR sensors have higher MR ratios their intrinsic high noise level is also higher. These technologies will be discussed in Sec. 2.4.

It should be noted that there exist further sensing technologies like mixed superconductor-GMR sensors [1], magnetoresistance sensors using MEMS (micro-electro-mechanical system) technology for flux guides, that are able to modulate external fields at high frequencies [2] as well as sensors based on optical pumping of atomic transitions [3], that have shown to reach fT resolution and are hence competitive to the SQUID. However, they have similar drawbacks, for example the requirement for cooling and/or lack of compatibility to CMOS fabrication technologies and are not established yet outside the laboratory. The focus of this thesis is put on

sensor type	detectivity at 10 Hz [T/ $\sqrt{\text{Hz}}$ ]	reference
low- $T_C$ SQUID	$\sim 1 - 10 \cdot 10^{-15}$	[7]
high- $T_C$ SQUID	$36 \cdot 10^{-15}$	[7]
Fluxgate	$10 \cdot 10^{-12}$	[8]
AMR	$5 \cdot 10^{-10}$	[9]
GMR	$\approx 1.5 \cdot 10^{-9}$	[9]
TMR	$\approx 1.5 \cdot 10^{-9}$	[9]
Micro-fluxgate	$5 \cdot 10^{-9*}$	[10]

Tab. 2.1. – Detectivities for various sensor types, \*averaged over a range of 64 mHz-10 Hz

the magnetoresistive technologies, more precisely on tunneling magnetoresistance, which appears to be a promising candidate for achieving pT-resolution at room temperature using CMOS compatible fabrication methods [4–6].

## 2.1 Noise in magnetic field sensors

The minimum field, that can be detected by a magnetic field sensor is determined by the ratio of the signal power to noise power, i.e. the signal-to-noise ratio (SNR) in a given bandwidth. The signal power can be increased by amplification, however, amplifiers will also amplify the noise and may even add new noise sources to the measurement, so the intrinsic noise power of the detector will be the ultimately limiting factor for the detection of small measurement quantities. In order to push a detection technology to its limits it is necessary to understand the underlying physical processes, that are the origin of the noise in the detector. The detector, which is in the focus of this thesis, is a magnetic tunnel junction (MTJ). In this section, the contributions to the noise in MTJs will be reviewed. At first a very general relation from statistical physics is introduced - the fluctuation dissipation theorem (sec. 2.1.1) - which is frequently applied to various noise phenomena. Because in MTJs, the electronic and the magnetic properties are interconnected due to spin-dependent transport of electrons, there are electronic and magnetic contributions to the total noise power, which are discussed in sections 2.1.2 and 2.1.3.

The noise power of an electronic device is determined in practice by measuring the mean square voltage  $\sqrt{V^2}$  in a given bandwidth  $\Delta f$ , which is determined by the components in the measurement setup. In Fig. 2.1 a schematic of a noise measurement setup is sketched: The device under test (DUT) can be represented by an ideal noiseless resistor  $R_{\text{ideal}}$  and a noise voltage source  $S_V$ . The DUT is connected to a low noise amplifier and the output signal is measured with an FFT Analyzer or a voltmeter at a load resistance  $R_L$  which also includes all resistive contributions from the circuitry and the internal voltmeter resistance. Then the noise

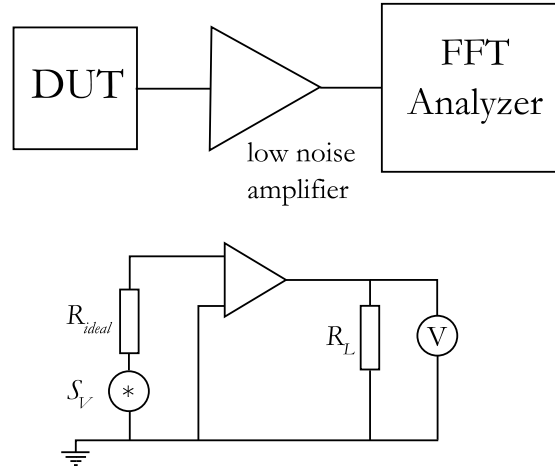


Fig. 2.1. – Schematic of a noise measurement circuit.

power  $P_{\text{noise}}$  generated by the DUT obtained in such a measurement is defined as:

$$P_{\text{noise}} = \frac{1}{R_L} \int_{f_1}^{f_2} S_V(f) df \approx \frac{1}{R_L} S_V(f_1) \cdot \Delta f = \frac{\bar{V}^2}{R_L} \quad (2.1)$$

with  $\Delta f = f_2 - f_1$ . If  $S_V(f)$  is flat the approximation in Eq. 2.1 is exact, which is the case for thermal noise but not for  $1/f$  noise (see Sec. 2.1.2). In Fig. 2.2 an example for noise measurements on magnetic tunnel junctions is shown. When a spectrum analyzer or FFT analyzer is used to carry out the noise measurement, the bandwidth refers to the spacing of the datapoints in the plot, which is also called the resolution bandwidth.  $\Delta f$  can be deduced from the fact that for  $N$  samples taken at the sampling frequency  $f_S$  the corresponding frequency spectrum that is displayed by the analyzer consists of  $N/2$  equally spaced lines. At zero Hz the DC average voltage is displayed and the next line is at lowest detectable frequency  $f_{\text{min}} = 1/\tau$ , which is determined by the length of the time record  $\tau$ . Hence, the spacing for all lines is

$$\Delta f = \frac{1}{\tau} \quad (2.2)$$

The upper limit of the frequency spectrum is determined by the Nyquist-Shannon sampling theorem, which says that the highest representable frequency for a time record sampled at a rate  $f_S$  is  $f_{\text{max}} \equiv f_{\text{Nyquist}} = f_S/2$  (see also Sec. 5.2). In order to compare the capabilities of various sensors to detect magnetic fields with field strength  $B$ , the measure of the detectivity  $D$  was introduced, which sets the sensitivity of the transduced voltage signal  $dV/dB$  into relation with the noise power  $P_{\text{noise}}$ . The mean square voltage detected in a certain bandwidth  $\Delta f$  is equal to the voltage taken from the DC sensor characteristics  $V = \frac{dV}{dB} \cdot B$  at the corresponding

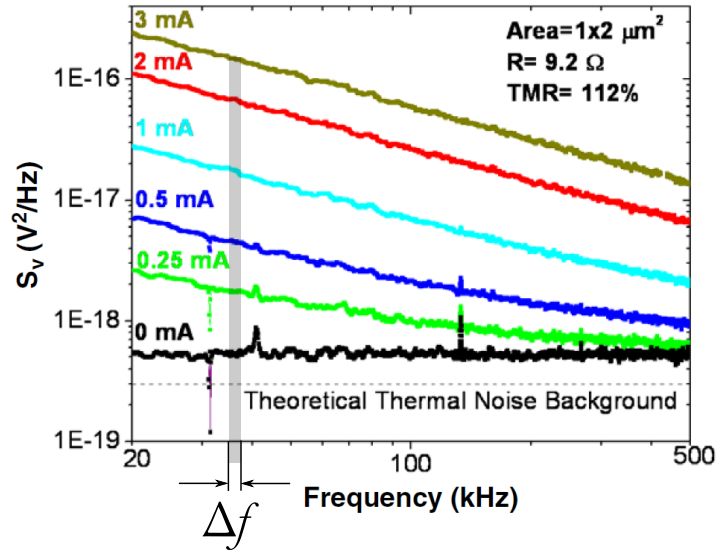


Fig. 2.2. – Noise spectra of magnetic tunnel junctions with different bias currents (adapted from [11]).

field strength when the averaging time for obtaining a datapoint of the sensor characteristics equals the length of the time record:

$$\sqrt{V^2} = \sqrt{S_V(f) \cdot \Delta f} = \frac{dV}{dB} B \quad (2.3)$$

When carrying out dimension analysis of this equation we come up with an expression for the minimum detectable field

$$B_{\min} = \frac{\sqrt{S_V(f) \left[ \frac{V^2}{\text{Hz}} \right]}}{\frac{dV}{dB} \left[ \frac{V}{T} \right]} \cdot \sqrt{\Delta f [\text{Hz}]} = D \left[ \frac{T}{\sqrt{\text{Hz}}} \right] \cdot \sqrt{\frac{1}{\tau} [\text{Hz}]} \quad (2.4)$$

This shows that either by increasing the measurement time for better averaging or reduction of the bandwidth by better filtering contribute to making  $B_{\min}$  as small as possible.

### 2.1.1 The fluctuation-dissipation theorem

The response of a thermodynamic system in equilibrium to a perturbation is described by the susceptibility  $\chi$ . The time average of an observable  $x(t)$  that fluctuates around a mean value of  $\langle x \rangle_0$  under the influence of a time-dependent field, i.e. the perturbation  $f(t)$  is defined by [12]

$$\langle x(t) \rangle = \langle x \rangle_0 + \int_{-\infty}^t f(\tau) \chi(t - \tau) d\tau \quad (2.5)$$

The fluctuation-dissipation theorem (FDT) states, that the power spectral density  $S_x(\omega) = \hat{x}(\omega)^* \hat{x}(\omega)$  of the observable  $x(t)$  can be linked to the dissipative (imaginary) part of the susceptibility  $\chi$  [13]:

$$S_x(\omega) = \frac{2k_B T}{\omega} \chi''(\omega) \quad (2.6)$$

The FDT states, that for each physical process which dissipates energy (e.g. in the form of heat) there has to be a reverse process caused by thermal fluctuations. A good example is thermal noise in a resistor: If a current is passed through a wire of finite resistance, the wire will heat up. The reverse process to this is the non-zero current that is generated in the wire due to thermal fluctuations of the electrons [14]. The theory behind this phenomenon will be discussed in the following section.

## 2.1.2 Electronic noise

### Thermal noise

Thermal noise arising from fluctuations of the conduction band electrons was discovered by John B. Johnson at Bell Labs and explained by his colleague Harry Nyquist [15]. Nyquist assumed a circuit of two conductors, each with a resistance  $R$  (see Fig. 2.3). The current  $I$  in the circuit is generated by the voltage  $V$  arising

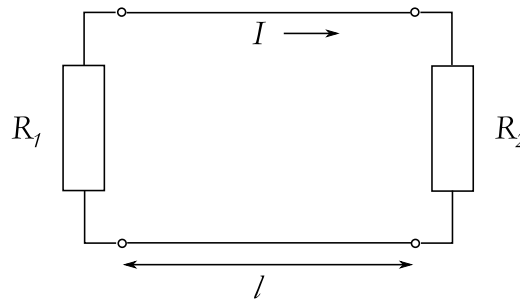


Fig. 2.3. – Circuit of two resistors connected by lines of length  $l$ .

from an inhomogeneous charge distribution generated by the thermally agitated electrons. Because the circuit contains two resistors in series and the current will be the important conserved quantity, we have

$$I = \frac{V}{2R} \quad (2.7)$$

To deduce the thermal power contained in the circuit, he proceeded as follows:



1. Introduce a line of length  $l$  between the two conductors, which does not have a resistance on its own as well as a propagation velocity  $v$  of the current.
2. After thermal equilibrium has been established, the system will be at a temperature  $T$ .
3. When thermal equilibrium is reached, the line becomes isolated from the conductors. This trick is used to determine, how much energy is contained in the line during the propagation time interval  $l/v$ .
4. The fact that the line is isolated corresponds to the reflection on the open end for a standing wave with eigenmodes  $f_n = \frac{nv}{2l}$ . Therefore, the number of eigenmodes available in a frequency interval  $\Delta f$  will be  $N = \frac{2l}{v} \Delta f$ .
5. Due to the equipartition law of thermodynamics each eigenmode has an energy of  $k_B T$  and the total energy of all modes in the interval  $\Delta f$ , that is transferred from **both** conductors to the line during the time of transit  $l/v$  will be

$$\Delta E = \frac{2l}{v} k_B T \Delta f$$

6. The average power from **each** conductor dissipated during the time of transit  $l/v$  is then given by

$$P_{\text{therm}} = k_B T \Delta f \quad (2.8)$$

7. Because the dissipated thermal power  $P_{\text{therm}}$  has to be equal to the power measured electrically  $P_{\text{elec}} = I^2 R$ , where  $I$  is given by eq. 2.7, we get

$$\frac{V^2}{4R^2} R = k_B T \Delta f$$

from which directly follows the well-known relation for Johnson-Nyquist noise

$$V^2 = 4Rk_B T \Delta f \quad (2.9)$$

## Shot noise

Classical shot noise originates from the fact, that electrical current consists of discrete portions of charge, namely the electrons. Walter Schottky observed in 1918 that electrons are emitted from the heated cathode in a vacuum tube according to a Poissonian process [16]. This means that the observed events (the emission of the electrons) have to be independent of each other with a large possible variation in

each observed time interval. Schottky arrived at a very simple expression for the mean square value of the current per unit bandwidth  $S_I = \bar{I}^2/\Delta f$ :

$$S_I = 2qI \quad (2.10)$$

If low bias voltages are assumed the system cathode - vacuum barrier - anode is in thermal equilibrium. Then the total current from the cathode to the anode will consist of a forward and a backward current

$$I = I_0 \left( e^{\frac{qV_B}{k_B T}} - 1 \right) \quad (2.11)$$

which gives for the total current noise power spectral density (mean squares are added):

$$\bar{i}^2 = S_I = 2qI_0 e^{\frac{qV_b}{k_B T}} + 2qI_0 = 4qI_0 \quad (2.12)$$

for a barrier voltage  $V_b = 0$  V. With a dynamic resistance  $r = (dI/dV_b)^{-1}$  the current noise power spectral density becomes

$$S_I = \frac{4k_B T}{r} \quad (2.13)$$

which is an alternative representation of eq. 2.9 for the thermal mean square noise voltage. Scattering theory [17] arrives at a result for shot noise, that considers Fermi-Dirac statistics with the transmission and reflection probabilities  $T_n$  and  $R_n = 1 - T_n$  over all transmission channels:

$$S_I = \frac{e^3 |V|}{\pi \hbar} \sum_n T_n (1 - T_n) \quad (2.14)$$

For low transmission  $T_n \ll 1$  in all channels and by using the multi-channel generalization of the Landauer formula for the conductance

$$G = \frac{e^2}{2\pi \hbar} \sum_n T_n \quad (2.15)$$

eq. 2.14 reduces to the Schottky formula (eq. 2.10). It became common to quantify the ratio of the actually present noise to the pure-Poissonian noise by the so called Fano factor

$$F = \frac{\sum (1 - T_n)}{\sum T_n} \quad (2.16)$$

In magnetic tunnel junctions with a crystalline MgO barrier it was observed in shot noise measurements, that the Fano factor is significantly reduced when the magnetizations in the electrodes are aligned parallel to each other [18] [19] [20]. This supports the validity of the coherent tunneling model described in later in Sec. 2.4.3, where the  $\Delta_1$ -state in the band gap leads to the high TMR ratios of

> 200% [21]. The generalized formula for the equilibrium and the non-equilibrium noise contributions to shot noise reads as follows:

$$S_I = \frac{e^2}{\pi\hbar} \left[ 2k_B T \sum_n T_n^2 + eV_b \coth \frac{eV_b}{2k_B T} \sum_n T_n (1 - T_n) \right] \quad (2.17)$$

Here, the first term arises from Fermi statistics and gives the non-equilibrium contribution to shot noise. For the case of a barrier with low transparency in all transmission channels  $T_n \ll 1$  and at room temperature eq. 2.17 reduces to the widely used expression for the mean square noise voltage per unit bandwidth given by Egelhoff et al. [4]:

$$S_V^{\text{shot}} = 2eIR^2 \coth \frac{eV_b}{2k_B T} \quad (2.18)$$

For low barrier voltages  $V_b$  and hence  $\coth \frac{eV_b}{k_B T} \approx \frac{2k_B T}{eV_b}$  eq. 2.18 reduces also to expression 2.13 for Johnson noise, which holds up to voltages of approx. 50 mV [4]. A mathematically less rigorous yet more intuitive derivation for shot noise in a tunnel barrier is given in reference [22]: Consider two metallic layers  $A$  and  $B$  separated by an insulation barrier. The net current  $\langle I \rangle$  generated by one electron with charge  $q$  passing the barrier during the sampling time  $\tau$  will consist of the sum of  $I_{AB} = (q/\tau) \cdot P_{AB}$  and  $I_{BA} = -(q/\tau) \cdot P_{BA}$  with probability weights  $P_i$ :

$$\langle I \rangle = I_{AB} + I_{BA} = \frac{q}{\tau} (P_{AB} - P_{BA}) \quad (2.19)$$

We have  $P_{AB} + P_{BA} < 1$ , because we also have to account for the case that no electron passes the barrier during  $\tau$ . For the mean square of the current we get

$$\langle I^2 \rangle = \sum_i I_i^2 P_i = \frac{q^2}{\tau^2} (P_{AB} + P_{BA}) \quad (2.20)$$

If detailed balance is given, which means that thermal equilibrium is achieved after each sampling time interval, the occupation numbers  $n_i$  of the energy levels in the conduction band of layers  $A$  and  $B$  and the transition probabilities  $P_i$  follow a Maxwell-Boltzmann distribution:

$$\frac{P_{AB}}{P_{BA}} = \frac{n_B}{n_A} = e^{-\frac{qV}{k_B T}} \quad (2.21)$$

Using these expressions for  $P_i$  in equations 2.19 and 2.20 we get

$$\langle I \rangle = \frac{q}{\tau} \left( P_{BA} e^{\frac{qV}{k_B T}} - P_{AB} e^{-\frac{qV}{k_B T}} \right) \quad (2.22)$$

$$\langle I^2 \rangle = \frac{q^2}{\tau^2} \left( P_{BA} e^{\frac{qV}{k_B T}} + P_{AB} e^{-\frac{qV}{k_B T}} \right) \quad (2.23)$$

Combining these two equations and using the fact that the sampling time  $\tau$  and the bandwidth  $\Delta f$  are connected by the Shannon sampling theorem  $f_S = 1/\tau = 2\Delta f$  results in

$$\langle I^2 \rangle = 2q \langle I \rangle \coth \frac{qV}{2k_B T} \Delta f \quad (2.24)$$

which is equivalent to eq. 2.18.

### Electronic 1/f noise

1/f noise or pink or flicker noise is abundant in electronic devices and metallic thin films and poses serious challenges to measurements at low frequencies. The PSD in homogeneous samples was defined by F. N. Hooge [23] as

$$\frac{S_V}{G^2} = \frac{\alpha}{N_c f} \quad (2.25)$$

in order to compare the results of a series of experiments carried out on semiconductors. Here,  $N_c$  is the number of charge carriers in the conductor,  $G$  is the conductance and  $\alpha$  the Hooge parameter. For inhomogeneous samples,  $N_c$  has to be replaced by a volume or cross section area element. Surprisingly,  $\alpha$  turned out to be a constant in the investigated samples. There is still much controversy about the underlying physical processes that produce 1/f noise. In field of semiconductor research, the two main directions to interpret 1/f noise are based either on fluctuations in the number of charge carriers or fluctuations in the mobility of the electrons [24]. Which model actually gives the correct interpretation depends critically on the observed physical system. A model frequently cited in the literature on magnetoresistance sensors (e.g. [25]) and which mathematically yields a 1/f spectrum is the McWorther model [26]. It was originally developed for metal-oxide-semiconductor-transistors (MOSTs), where noise in the source-drain current arises from charge traps in the gate oxide. The trapping and detrapping of the electrons is described by a time constant

$$\tau = \tau_0 \exp\left(\frac{z}{\lambda}\right) \quad (2.26)$$

with the distance  $z$  of a trap from the surface of the gate electrode and the Wenzel-Kramer-Brillouin attenuation length  $\lambda = h/(4\pi)(2m^*\Phi_B)^{-1/2}$  ( $h$  ... Planck's constant,  $m^*$  ... effective mass,  $\Phi_B$  ... tunneling barrier height) [24]. An arbitrary quantity that has noise can be written as

$$X(t) = \langle X \rangle + \Delta X(t) \quad (2.27)$$

with

$$\Delta X(t) = \sum_n a_n e^{i\omega t} + a_n^* e^{-i\omega t} \quad (2.28)$$

and  $\langle(\Delta X)^2\rangle$  being constant for stationary noise. The auto correlation function

$$\phi_X(t) = \langle\Delta X(t_0)\Delta X(t_0 + t)\rangle \quad (2.29)$$

describes the decay of the fluctuation  $\Delta X(t)$  and is linked to the spectral density  $S_X(\omega)$  by the Wiener-Khintchine theorem:

$$S_X(\omega) = 4 \int_0^\infty \phi_X(t) \cos \omega t dt \quad (2.30)$$

If the fluctuation now decays according to

$$\frac{d\Delta X}{dt} = -\frac{\Delta X}{\tau} \quad (2.31)$$

we get for the autocorrelation function

$$\phi_X(t) = \langle(\Delta X)^2\rangle e^{-\frac{t}{\tau}} \quad (2.32)$$

and by using eq. 2.30 a Lorentzian spectrum for the spectral density

$$S_X(\omega) = \langle(\Delta X)^2\rangle \frac{4\tau}{1 + \omega^2\tau^2} \quad (2.33)$$

Summing up a large number of such Lorentzian spectra that have relaxation times between  $\tau_1$  and  $\tau_2$  with statistical weights according to the distribution

$$g(\tau)d\tau = \frac{1}{\ln \tau_2/\tau_1} \frac{1}{\tau} \quad (2.34)$$

directly leads to a 1/f spectrum in the frequency range  $\tau_2^{-1} < \omega < \tau_1^{-1}$ :

$$\begin{aligned} S_X(\omega) &= \int_{\tau_1}^{\tau_2} g(\tau) \langle(\Delta X)^2\rangle \frac{4\tau}{1 + \omega^2\tau^2} d\tau \\ &= \frac{\langle(\Delta X)^2\rangle}{\ln(\tau_2/\tau_1)} \frac{4}{\omega} [\arctan(\omega\tau_2) - \arctan(\omega\tau_1)] \end{aligned} \quad (2.35)$$

because

$$\int \frac{1}{1 + x^2} dx = \arctan(x) \quad (2.36)$$

Evaluating the integral using the relations

$$|x| < 1 : \arctan(x) = \sum_{k=0}^{\infty} (-1)^k \frac{x^{2k+1}}{2k+1} \approx x - \frac{x^3}{3} \quad (2.37)$$

$$|x| > 1 : \arctan(x) = \pm \frac{\pi}{2} + \sum_{k=0}^{\infty} (-1)^{k+1} \frac{1}{(2k+1)x^{2k+1}} \quad (2.38)$$

$$\approx \pm \frac{\pi}{2} - \frac{1}{x} + \frac{1}{3x^3} \quad (2.39)$$

yields in fact one particular range for the frequency  $\omega$ , where 1/f noise is observed:

$$\omega < \tau_2^{-1} \quad S_X(\omega) = \frac{\langle(\Delta X)^2\rangle 4\tau_2}{\ln(\tau_2/\tau_1)} \quad (2.40)$$

$$\tau_2^{-1} < \omega < \tau_1^{-1} \quad S_X(\omega) = \frac{\langle(\Delta X)^2\rangle 1}{\ln(\tau_2/\tau_1) \omega} \quad (2.41)$$

$$\tau_1^{-1} < \omega \quad S_X(\omega) = \frac{\langle(\Delta X)^2\rangle 1}{\ln(\tau_2/\tau_1) \pi^2 \tau_1 \omega^2} \quad (2.42)$$

It has to be mentioned that McWorther's model did not turn out to work very well as an explanation for the physical mechanisms leading to 1/f noise in MOSTs. However, it can be applied successfully to discontinuous metal films deposited onto an insulator, where electrons tunnel from one island to another. Apart from the direct tunneling between the two conductors there exists another process, where electrons tunnel from the conductor to traps in the insulator. This creates a number fluctuation of charge carriers in the tunneling current. The time constant of these fluctuations is (cp. Eq. 2.26)

$$\tau(x) \propto \exp \frac{4\pi \sqrt{2m(E_C - E_F)}x}{h} \quad (2.43)$$

where  $E_C$  is the energy level of the conduction band of the insulator and  $E_F$  is the Fermi level. As the tunneling of the electrons to the traps is an uncorrelated process, the procedure described before can be used to derive a 1/f spectrum by summing up Lorentzian spectra with a certain distribution of time constants. In magnetic tunnel junctions the tunneling between interface states and traps in the oxide layer contribute to the overall low frequency noise [27] [28]. The Hooge parameter  $\alpha$  varies among various MTJs, but is known to be dependent on the resistance-area-product of the device [4].

### 2.1.3 Magnetic noise

Magnetic noise in magnetoresistance sensors (see Sec. 2.4) is the sum of thermal and 1/f magnetic noise and manifests itself in voltage fluctuations due to the coupling of the magnetic to the electronic properties. In these sensors, the fluctuations of the magnetization couple to resistance fluctuations, because these sensors change their electrical resistance when the relative alignment of two magnetic layers (the pinned layer and the free layer) is modified by an external magnetic field. Thermal magnetic noise  $S_M(f)$  originates (mainly) from fluctuations of the free layer's magnetization and can be expressed by a fluctuation-dissipation relation (see Eq. 2.6) [25] in SI units as

$$S_M = \frac{2k_B T}{\pi \mu_0 f} \chi_M''(f). \quad (2.44)$$

This translates to a voltage noise by  $S_V \equiv (dV_J/dM)^2 S_M$  with  $V_J$  as the junction bias voltage and gives [4, 29]

$$S_V = \left( \frac{V_J(\Delta R/\bar{R})}{2M_S} \right)^2 = \frac{4k_B T \alpha}{\mu_0 \gamma H_K^2 M_S V}, \quad (2.45)$$

where a linear magnetoresistance sensor transfer curve was assumed, so that  $dV_J/dM = dV_J/dR \cdot dR/dM \approx V_J/\bar{R} \cdot \Delta R/(2M_S)$ .  $(\Delta R/\bar{R})$  is the relative change of the resistance upon rotation of the free layer's magnetization,  $M_S$  is the saturation magnetization and  $V$  is the particle volume.  $\alpha$  is the dimensionless Gilbert damping parameter from the Landau-Lifshitz-Gilbert (LLG) equation (see also Eq. 4.20 in Sec. 4.2),  $\gamma$  is the electron gyromagnetic ratio in A/(m · s) and  $H_K$  is the anisotropy field in A/m. Eq. 2.45 holds for low frequencies far below the resonance frequency  $f \ll f_{\text{res}} \sim 10^9$  Hz given by the LLG equation, which is the microscopic equation of motion of a single spin in an external magnetic field, and yields a white noise spectrum.

1/f-type magnetic noise is explained by Egelhoff et al. [4] through magnetization hopping between metastable states of domains in the free layer. Adding up the Lorentzian type spectra of isolated two-level-fluctuators will yield directly a 1/f spectrum, if the escape times have a distribution  $\propto \tau$  as described before in sec. 2.1.2. For a small number of such fluctuators random telegraph signal noise was observed, which is  $\propto \omega^{-\beta}$  with  $\beta > 1$ . Ingvarsson et al. [25] could give an explanation of their experimental data taken from micron-scale MTJs based on the fluctuation dissipation theorem. The data showed that the noise power spectral density  $S_R$  changed proportionally to the derivative  $\partial R/\partial H$  of the magnetoresistance loop. This is because the linear response to the field, i.e. the real part of the susceptibility  $\chi' = (\partial M/\partial H) = (\partial M/\partial R)(\partial R/\partial H)$ , is linked to its imaginary part via the Kramers-Kronig relation

$$\chi'(\omega = 0) = \frac{2}{\pi} \int_0^\infty \frac{\chi''(\omega)}{\omega} d\omega \quad (2.46)$$

Together with Eq. 2.44 in the representation for magnetization fluctuations in SI units and by using  $(\partial M/\partial R) \approx 2M/\Delta R$  the relation between the measured DC susceptibility and the 1/f-noise spectrum  $S_R$

$$\frac{\partial R}{\partial H} = \frac{2\mu_0 m}{k_B T \Delta R} \int_0^\infty S_R(\omega) d\omega \quad (2.47)$$

could be explained by using the a fluctuation dissipation relation.

## 2.2 SQUIDS

Superconducting quantum interference devices (SQUIDs) are currently the most sensitive magnetic field sensors available and are able to detect magnetic field changes in the femto-Tesla range. Their operating principle is based on the magnetic flux quantization and the Josephson effects.

Superconductivity was discovered by Kamerlingh-Onnes in 1911, when he observed that the electrical resistance of mercury dropped to an infinitesimal small value below a critical temperature  $T_C$  of 4.2 K. This temperature could be obtained after increased effort has been put into the development of helium liquefaction by Kamerlingh-Onnes and his co-workers [30, 31]. During the transition from the normal to the superconducting regime the electrons in the metal start to form a Bose-Einstein condensate [32–34] of Cooper pairs. Cooper pairs are pairs of electrons, that are created when the attractive potential of the surrounding lattice on one electron attracts another electron of opposite spin. These two electrons then become correlated and form a boson with zero spin [35]. As there are a large number of electrons that could form a Cooper pair, a collective state is created that permits resistanceless exchange of electrons over the whole conductor, as explained by the Bardeen-Cooper-Schrieffer (BCS) theory [36]. In 1986 Bednorz and Müller discovered a new class of superconducting materials that have significantly higher transition temperatures, so that liquid nitrogen with a boiling point of 77 K can be used as a coolant instead of liquid helium [37]. The most prominent material among the high temperature superconductors (HTS) is  $\text{YBa}_2\text{Cu}_3\text{O}_{7-\delta}$  (YBCO) [38, 39]. HTS are typically ceramic oxides, whereas low temperature superconductors (LTS) are metallic [40, 41]. An important property of superconductors was observed by Meissner and Ochsenfeld in 1933: Magnetic field lines are not able to penetrate deeply into a superconductor, they are screened by surface currents, that cause a rapid damping of the magnetic field [42]. The Meissner-Ochsenfeld effect was explained by Fritz and Heinz London by their phenomenological London equations [43]. In the following chapters it will be explained how the Meissner-Ochsenfeld effect together with the quantization of the magnetic flux in a superconducting ring is used in SQUIDs. Furthermore, the Josephson junction will be discussed as the transducer element of the SQUID which converts magnetic flux to a voltage signal.

### 2.2.1 Flux quantization in a superconducting ring

The wave function of a quantum mechanical particle traveling inside a region with zero magnetic field ( $\mathbf{B} = 0$ ) along a path  $P$ , but a non-zero vector potential  $\mathbf{A}$  (with  $\nabla \times \mathbf{A} = \mathbf{B}$ ) acquires a phase

$$\delta = \frac{q}{\hbar} \int_P \mathbf{A} d\mathbf{x}, \quad (2.48)$$



where  $\hbar = 1.05 \cdot 10^{-34}$  J/s is Planck's constant  $h$  divided by  $2\pi$  and  $q$  is the charge. In a superconducting ring enclosing an area  $S$  the macroscopic wave function is a standing wave, implying that a phase change along a path inside the ring can only be a multiple of  $2\pi$ . Hence, it can be deduced that also the magnetic flux  $\Phi = \mathbf{B} \cdot \mathbf{S}$  inside the ring with area  $S$  is a positive integer multiple  $n$  of the magnetic flux quantum  $\Phi_B$ :

$$\delta = \frac{q}{\hbar} \int_P \mathbf{A} dx = \frac{q}{\hbar} \int_S \nabla \times \mathbf{A} d\mathbf{S} = \frac{q}{\hbar} \mathbf{B} \mathbf{S} = \frac{q}{\hbar} \Phi = \frac{2e}{\hbar} \cdot \Phi_B \cdot n = 2\pi n \quad (2.49)$$

$$\Rightarrow \Phi_B = \frac{2\pi\hbar}{2e} = \frac{h}{2e} = 2.07 \times 10^{-15} \text{T} \cdot \text{m}^2 \quad (2.50)$$

Here, the particle of interest is a Cooper pair and hence  $q = 2e$  [41].

## 2.2.2 The Josephson junction

A Josephson junction is created when two superconductors are connected by a thin layer of a non-superconducting material (also called a weak link) [41, 44, 45]. The quantum mechanical description of the tunneling of the Cooper pairs through the barrier makes use of the macroscopic wave functions

$$\Psi_1 = \Psi_0 \exp(i\theta_1) \quad \text{and} \quad \Psi_2 = \Psi_0 \exp(i\theta_2) \quad (2.51)$$

of the superconductor (SC) 1 and SC 2, respectively. If there should be a current through the junction, the phases of the tunneling Cooper pairs from SC 1 have to match to the phase of the Cooper pairs in SC 2. During their transport through the barrier they will either obtain the necessary phase shift or they will be reflected, which can be described mathematically by the Schrödinger equation  $i\hbar\partial\Psi/\partial t = \mathcal{H}\Psi$ :

$$i\hbar \frac{\partial\Psi_1}{\partial t} = \hbar\omega\Psi_2, \quad i\hbar \frac{\partial\Psi_2}{\partial t} = \hbar\omega\Psi_1 \quad (2.52)$$

This leads to a DC current  $I$  at the junction, which depends on the phase difference  $\delta = \theta_1 - \theta_2$  of  $\Psi_1$  and  $\Psi_2$ :

$$I = I_0 \sin \delta \quad (2.53)$$

Eq. 2.53 is the first Josephson equation describing the DC Josephson effect at zero bias voltage to the junction.  $I_0$  denotes the maximum current that can flow over the junction without a breakdown of the superconducting properties. If a bias voltage  $V$  is applied the Cooper pair changes its energy by  $qV$  with  $q = 2e$  from SC 1 to SC 2. Hence, we can assume that the Fermi levels change by  $\pm eV$  on each side of the junction and Eqs. 2.52 now read

$$i\hbar \frac{\partial\Psi_1}{\partial t} = \hbar\omega\Psi_2 - eV\Psi_1, \quad i\hbar \frac{\partial\Psi_2}{\partial t} = \hbar\omega\Psi_1 + eV\Psi_2 \quad (2.54)$$

From this, the second Josephson equation for the AC Josephson effect can be deduced which treats the time evolution of the phase difference  $d\delta/dt$ :

$$V = \frac{\hbar}{2e} \frac{d\delta}{dt} \quad (2.55)$$

This is an ordinary differential equation with the solution  $\delta(t) = \delta_0 + (2e/\hbar)Vt$  which can be used to rewrite Eq. 2.53 as

$$I = I_0 \sin \left( \delta_0 + \frac{2e}{\hbar} V \cdot t \right) \quad (2.56)$$

where  $2eV/\hbar$  has the dimension of a frequency and adds an AC component to the total current flowing through the junction.

### 2.2.3 DC SQUID

The basic DC SQUID consists of a superconducting ring with two identical Josephson junctions located opposite of each other. Through the ring a bias current  $I_{\text{tot}}$  is fed which splits up into two separate components  $I_1$  and  $I_2$ . Without an external magnetic field the current in one of the Josephson junctions is fully determined by the properties of the two superconductors, i.e. the wave functions of the tunneling Cooper pairs which led to Eq. 2.53 as a result. Hence, we can write

$$I_1 = I_0 \sin \delta_1 \quad \text{and} \quad I_2 = I_0 \sin \delta_2$$

In order for the current to be conserved the phase difference of the currents in junction 1 and junction 2 must be multiples of  $2\pi$ :

$$\delta_2 - \delta_1 = 2\pi n \quad \text{with} \quad n = 0, 1, 2, \dots$$

For  $n = 0$  we define  $\delta_1 = \delta_2 \equiv \delta_0$ .

If a magnetic field is applied we also have a vector potential which gives an additional contribution to the phase difference of  $I_1$  and  $I_2$  (see also Eq. 2.48) [46]:

$$\delta = \theta_1 - \theta_2 - \frac{2e}{\hbar} \int_a^b \mathbf{A} d\mathbf{x}$$

If the path integral is carried out once over junction 1 and once over junction 2 the current phases can now be written as

$$\delta_1 = \delta_0 + \frac{e}{\hbar} \Phi \quad \text{and} \quad \delta_2 = \delta_0 - \frac{e}{\hbar} \Phi$$

for two identical Josephson junctions ( $\delta_0 = \theta_1 - \theta_2$ ) [41]. More intuitively, this result can be explained by the Meissner-Ochsenfeld effect: A shielding current  $J$  flows inside the superconducting ring when a magnetic field is applied.  $J$  adds to

the current in one junction, but counteracts the current in the other.

The total current in the SQUID takes the form

$$I_{\text{tot}} = I_1 + I_2 = I_0 \left[ \sin \left( \delta_0 + \frac{e}{\hbar} \Phi \right) + \sin \left( \delta_0 - \frac{e}{\hbar} \Phi \right) \right] = 2I_0 \sin \delta_0 \cos \left( \frac{e\Phi}{\hbar} \right) \quad (2.57)$$

For fixed  $\delta_0$   $I_{\text{tot}}$  shows an oscillatory behavior depending on the applied flux  $\Phi$ . Once the flux is an integer multiple of the magnetic flux quantum  $\Phi_B$  the current (or the measured voltage (see Fig. 2.4 b)) reaches a maximum. The read-out of

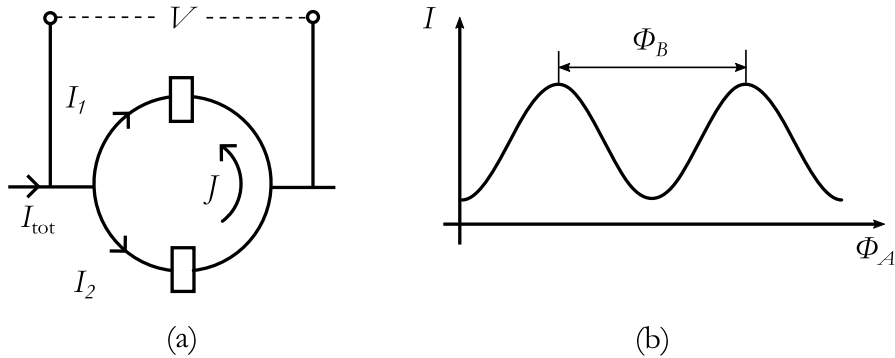


Fig. 2.4. – (a) Sketch of a DC SQUID: Two superconductors are connected by two identical Josephson junctions on opposite sides of the ring. (b) The cosine-like output signal is derived from the interference of the Cooper pair wave functions and the law of current conservation for  $I_{\text{tot}}$  when  $\Phi$  is increased (see Eq. 2.57). The period of  $I_{\text{tot}}$  is the magnetic flux quantum  $\Phi_B$  from Eq. 2.50.

the SQUID is usually realized with a flux-locked loop (FLL) shown in Fig. 2.5. The SQUID works as a flux-to-voltage converter and therefore an alternating bias flux signal (typ. 100 kHz) is applied. The SQUID is operated at a point where the output signal has the steepest slope (see Fig. 2.4 b)). With the the modulated signal added here small shift from the operating point can be detected using a lock-in amplifier where the frequency of the modulated signal is used as the reference signal. The resulting output current can be used as a feedback current, which is fed to a coil that provides the necessary flux to drive the SQUID back to its operating point. Like this, the dynamic range of the SQUID can also be notably increased [45, 47].

## 2.3 Fluxgate sensors

The first patent for a fluxgate sensor dates back to 1931 [40], but these type of sensors are still competing with the most sensitive magnetic field sensing technology, which is the SQUID (see Sec. 2.2). Fluxgate sensors are reliable devices, which work over a wide range of temperatures and reach a resolution of 10 pT [10]. A basic setup for a fluxgate sensor is sketched in Fig. 2.6. It consists of a rod-shaped core made of a soft-magnetic material with two coils wound around it. One coil

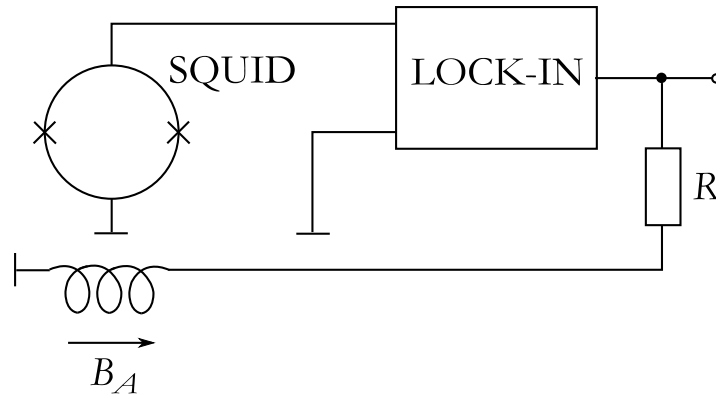


Fig. 2.5. – Flux locked loop (FLL): The modulated output signal is fed into a lock-in amplifier with the frequency of the modulated input flux as a reference. The lock-in signal is used as a measurement signal and as a means to drive the SQUID back to its operating point.

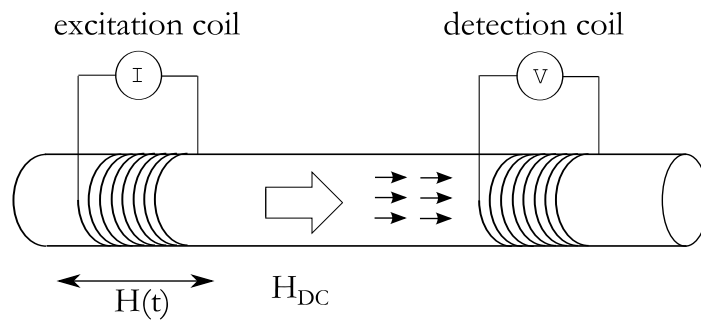


Fig. 2.6. – Schematic setup of a fluxgate magnetometer: The alternating field  $H(t)$  generated by the excitation coil periodically saturates the soft-magnetic core. An applied constant field  $H_{DC}$  adds a magnetic bias, so that the core gets saturated earlier in one direction than the other. The output signal of the fluxgate magnetometer is the induced voltage in the pick-up coil.

serves as the excitation coil, through which an alternating current is passed that generates the sinusoidal field  $H(t) = H_0 \sin \omega t$ , where  $\omega = 2\pi f$  denotes the angular frequency of the driving current. The field periodically drives the core to saturation, which means that  $H_0 > H_{sat}$ , when  $H_{sat}$  is the saturation field of the core. The second coil serves as a pick-up coil and detects the periodic change in magnetic flux driven by the excitation coil. The fluxgate magnetometer is used to measure DC or low frequency fields, which would not be possible with a classical induction coil operating without a soft-magnetic core. If a DC field  $H_{DC}$  is now applied in the long axis of the core, the magnetic flux detected by the pick-up coil gets “biased”. This results in a harmonic distortion of the induced voltage signal caused by  $H_{DC}$ , which represents the quantity to be measured.

In Fig. 2.7 the fluxgate signal generation is shown in more detail. In the left panels of Figs. 2.7 a) and b) the hysteresis loop of the core  $M(H)$  and the driving field  $H(t)$

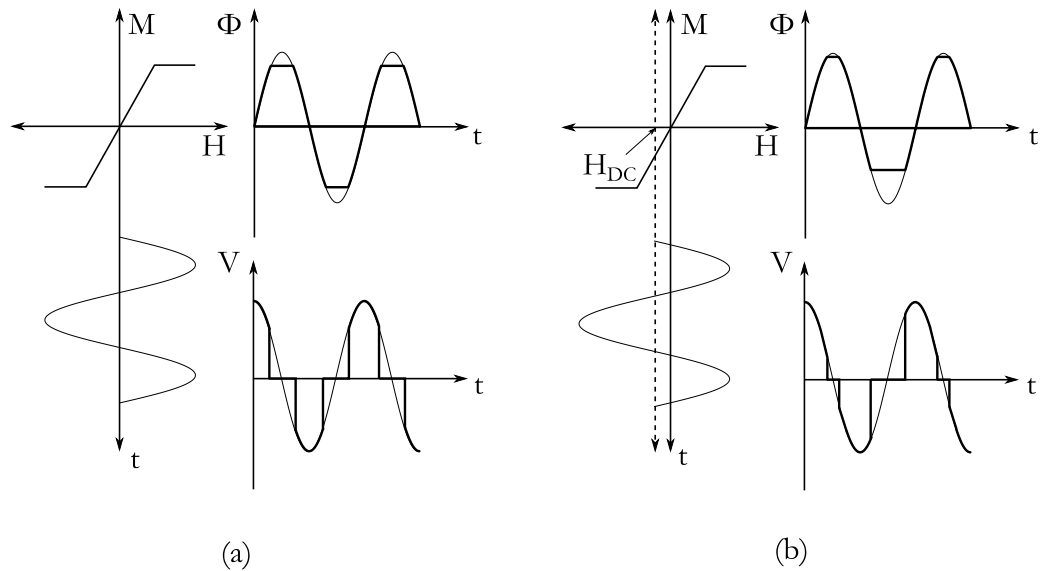


Fig. 2.7. – Fluxgate signal generation: (a) no bias field  $H_{DC}$  applied, equidistant voltage peaks in the  $V(t)$ -signal, (b) With  $H_{DC}$  applied,  $V(t)$  becomes asymmetric.

from the excitation coil are sketched. When the  $M(H)$  characteristic is run through by  $H(t)$  this translates to a magnetic flux signal  $\Phi(t)$  and an induction voltage  $V(t) \propto d\Phi/dt$  in the pick-up coil. Fig. 2.7 a represents the unbiased case with no additional field  $H_{DC}$  applied. The peaks in the  $V(t)$ -signal occur at equidistant time intervals, which is changed, when  $H_{DC}$  turned on. Then, a shift is introduced to the driving signal reading now  $\mathbf{H}(t) = \mathbf{H}_0 \sin \omega t + \mathbf{H}_{DC}$ . The core is now saturated earlier in one field direction than in the other, which we refer to as the bias. In the voltage signal, this is reflected in a developing asymmetry in the time intervals between the induction voltage peaks. If a Fourier analysis is carried out, the asymmetry in the time domain is reflected in the appearance of even harmonics in the frequency spectrum. This can be understood by imagining the Fourier decomposition as adding up elementary sine-waves with weighted amplitudes to form a desired waveform. Then, a wave form with a symmetric duty cycle can be fully represented by uneven harmonics of the base frequency, because the third, fifth etc. harmonics have zero crossings at the same points as the first harmonic. The even harmonics have maxima, when the odd harmonics are zero, and are therefore only needed to describe the waveform if an asymmetry is introduced to the duty cycle. A detailed mathematical analysis of the harmonic components as is presented in Sec. 3.2 for the TMR fluxgate

signal, in which the fluxgate principle is applied to a magnetic tunnel junction. Using an apparent permeability  $\mu_a$  according to [48]

$$\mu_a(t) = \frac{\mu_r(t)}{1 + D(\mu_r(t) - 1)} \quad (2.58)$$

$$\approx \frac{1}{2}(\mu_{a,\max} + \mu_{a,\min}) + \frac{1}{2}(\mu_{a,\max} - \mu_{a,\min}) \cos(2\omega t + \Delta\phi) \quad (2.59)$$

$$\text{where } \mu_r = 1 + \chi = \frac{B}{\mu_0 H} \quad (2.60)$$

the output voltage for the classical fluxgate reads

$$V = NA\mu_0 H_{\text{DC}} \frac{d\mu_a}{dt} = -NA\omega(\mu_{a,\max} - \mu_{a,\min})\mu_0 H_{\text{DC}}, \quad (2.61)$$

where  $N$  is the number of windings in the pick-up coil and  $A$  is the coil diameter. In Eq. 2.59 the fact was used, that the permeability of the core is a function that changes with half the periodicity of the driving field  $H(t)$ .

Classical fluxgate sensors are commonly used in measurement instrumentation, where robustness is rated higher in importance than power consumption and overall fabrication costs. Therefore, they are frequently used for geophysical and space applications. Furthermore, the ‘‘Förster’’ probe was used for non-destructive testing of ferromagnetic materials [40]. The main drawback of fluxgate magnetometers is their incompatibility with standard CMOS fabrication techniques, which makes them unsuitable for cheap mass production. Several attempts have been made to fabricate fully integrated CMOS fluxgates with planar coils (e.g. [49, 50]), but with decreasing size of the core the noise level increases by several orders of magnitude (see also Tab. 2.1). However, they are the best selection if resolution in the nT range is required, in which they outperform high- $T_C$  SQUIDs due to their larger dynamic range.

## 2.4 Magnetoresistance sensors

In this section we will give an overview of the three most relevant magnetic field sensing technologies for industrial applications - anisotropic, giant and tunneling magnetoresistance. The information given here follows Refs. [40, 51, 52], if not stated otherwise.

A general definition of magnetoresistance in terms of a relative change in electrical resistivity  $\rho$  of a material can be given as

$$\frac{\Delta\rho}{\rho} = \frac{R(H) - R(0)}{R(0)}. \quad (2.62)$$

Here,  $R(H)$  is the measured resistance when a magnetic field  $H$  is applied and  $R(0)$  is the resistance in zero field.  $\Delta\rho/\rho$  is in general expected to be a positive quantity,

because the electrons in a metal are forced onto a circular path due to the Lorentz force, that is generated by the magnetic field. This path will differ from the ideal path they usually take in order to minimize scattering. The observation of negative magnetoresistance (MR) in ferromagnets therefore requires a different model of explanation, which was first given by Mott [53, 54]. In Fig. 2.8 the density of states for a ferromagnetic material is sketched. In a metal, the electrical transport is always carried by the electrons in the unfilled shells, which are the s- and d-orbitals (orbital momentum  $\mathbf{L} = 0$  for s and  $\mathbf{L} = 2$  for d) in the transition metal group. Ferromagnetism in Fe, Co and Ni occurs due to the competition between the energy contributions from quantum mechanical exchange due to the Pauli principle and Coulomb interaction. In the transition metals or 3d-elements the inner 3d orbitals are filled after the outer 4s-orbitals have been filled. Then, the 3d-orbitals are filled with electrons of the same spin in order to minimize their Coulomb interaction. This leads to the development of a magnetic moment on the atom. The conductivity of a ferromagnetic metal is given by

$$\sigma = \frac{n_s e^2 \tau_s}{m_s^*} + \frac{n_d e^2 \tau_d}{m_d^*}, \quad (2.63)$$

where  $n_s, n_d$  are the number of electrons in the s and d bands and  $\tau_s, \tau_d$  are the scattering times. In the conductivity the first term is dominant, because for the effective masses we have  $m_d^* \gg m_s^* \approx m_e$  and hence transitions from the s to the d band will induce the larger change on the conductivity than the other way. If we consider that spin flip processes are very unlikely to occur it can be argued that with a magnetic field applied s-d-transitions are more unlikely than in zero field and so  $R(H) > R(0)$ , which leads to negative magnetoresistance. The absence of spin flip processes allows for a separate treatment of spin-up and spin-down currents, which is a common approach to explain anisotropic (AMR), giant (GMR) and tunneling (TMR) magnetoresistance. XMR sensors have numerous applications in consumer products such as wheel speed sensors in cars or compasses in cell phones. The discovery of the GMR effect by P. Grünberg and A. Fért in 1988 led to the development of the billion dollar business of magnetic recording industry. Hard disk read heads could then be downscaled by several orders of magnitude from coil sensors to microstructured GMR sensors. The rapid implementation of this new discovery as an industrial product was an important point for the Nobel committee to award Grünberg and Fért with the Nobel Prize in Physics in 2007.

### 2.4.1 Anisotropic magnetoresistance

Anisotropic magnetoresistance (AMR) occurs in a ferromagnetic material when a magnetic field is applied perpendicular to the direction into which an electrical current is flowing. Due to the crystal field, i.e. the electrical potential that is seen by the free electrons, the electronic wave function loses symmetry and s-d-scattering

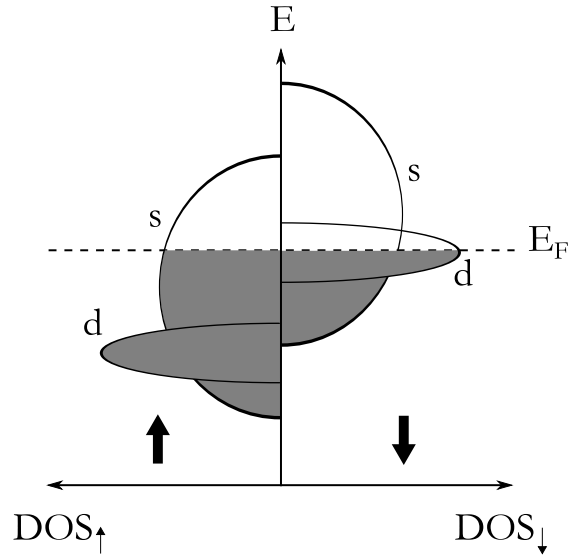


Fig. 2.8. – Schematic densities of states (DOS) for a ferromagnetic material ( $\text{DOS}_{\uparrow\downarrow}(E)$  ... DOSs for spin-up and spin-down electrons). The spin-split s- and d-bands in a ferromagnetic material have a different number of states available for spin-up and spin-down electrons at the Fermi energy  $E_F$ .

becomes anisotropic. The anisotropic part of the electrical resistance depends on the exact shape of the Fermi surface, which is not exactly known in general. Therefore, the magnitude of the AMR effect can hardly be predicted by theory and is almost exclusively found through experiments. An AMR sensor element usually consists of a rectangular ferromagnetic thin film through which a current is passed in the long axis. If a field  $\mathbf{H}$  is applied perpendicular to the current direction in the film plane, the magnetization is rotated out of its equilibrium position towards the field. The magnetization removes degeneracy for the orbital states by defining a quantization axis for the spin, which in interaction with the magnetocrystalline anisotropy forms a surrounding with different scattering probabilities in the spatial directions. If  $\theta$  is the angle between the current direction and the magnetization, the resistivity of an AMR element is given by

$$\rho(\theta) = \rho_{\perp} + (\rho_{\parallel} - \rho_{\perp}) \cos^2 \theta, \quad (2.64)$$

where  $\rho_{\perp} = \rho(\theta = 90^\circ)$ . Typical materials for AMR sensors are e.g. amorphous ferromagnets, which have a low anisotropy field  $H_K$  (the magnetization rotates easily, which gives high sensitivity), large  $\rho$  (high signal) but only  $\Delta\rho/\rho \approx 0.07\%$ . Most commonly used is Permalloy (81at.%Ni/19at.%Fe), which has  $\Delta\rho/\rho \approx 4\%$  and almost zero magnetostriction, but higher  $H_K$ .

The output characteristics from Eq. 2.64 of an AMR sensor can be linearized by depositing a so-called Barber pole structure onto the film. The “Barber poles” are stripes of a highly conductive material such as Al or Cu, which are deposited at  $45^\circ$



to the long axis of the sensor. Then, the current will also flow in a zig-zag pattern at  $45^\circ$ , thereby taking a longer path in the high-conductivity metal and the shortest possible path in the ferromagnetic material. With  $\sin \theta = H/H_K$  Eq. 2.64 can be written for the Barber-Pole-AMR sensor as

$$R(H) = R_0 \pm \Delta R \frac{H}{H_K} \sqrt{1 - \left(\frac{H}{H_K}\right)^2}. \quad (2.65)$$

## 2.4.2 Giant magnetoresistance

*“If GMR is to work, structures consisting of layers that are only a few atoms thick have to be produced. For this reason GMR can also be considered one of the first real applications of the promising field of nanotechnology.” [55]*

The giant magnetoresistance (GMR) effect can be observed in a multilayered system of nonmagnetic and magnetic metallic layers, which are only a few nm thick. When a current is applied to a sandwich of two magnetic layers separated by a nonmagnetic but metallic spacer layer, the electrical resistance measured will depend on the relative alignment of the magnetizations. In a spin valve GMR sensor one magnetization can rotate freely in an external magnetic field, whereas the other is fixed in space up to a certain field. The mechanisms by which one layer’s magnetization can be kept fixed are explained in Sec. 5.3.1, where measurement data on magnetic tunnel junctions (see also Sec. 2.4.3) are presented. An intuitive picture of physics of the GMR effect is given in Fig. 2.9. As already mentioned at the beginning of this section, the conduction electrons in a ferromagnetic material carry a magnetic moment or spin, which is either “up” or “down”. Due to the molecular field which originates from the atomic interactions, one spin orientation is lowered in energy with respect to the other. This gives rise to different densities of states (DOS) at the Fermi level  $E_F$  (see Fig. 2.8) for spin-up and spin-down electrons. The DOS at  $E_F$  determines the transport properties of a metal and is plays an important role when solving the Boltzmann equation for a ferromagnet (FM)-non-magnet (NM) layer system. In a GMR multilayer there are two possible ways to apply the current: in the film plane (current in plane (CIP) GMR) and perpendicular to the film plane (current perpendicular to plane (CPP) GMR). For each of these geometries a solution for the Boltzmann equation exists [56–58], which gives a higher conductivity if the magnetizations are aligned parallel than for the antiparallel state. This is due to the reduced number of available states at  $E_F$  in the antiparallel case. The spin-down electrons are the majority carriers in the left FM, but they do not find as much available states in the right FM and so are partly backscattered. The minority electrons with spin down give a smaller contribution anyway to the total current from left to right. Hence, for the antiparallel case the transport for both majority

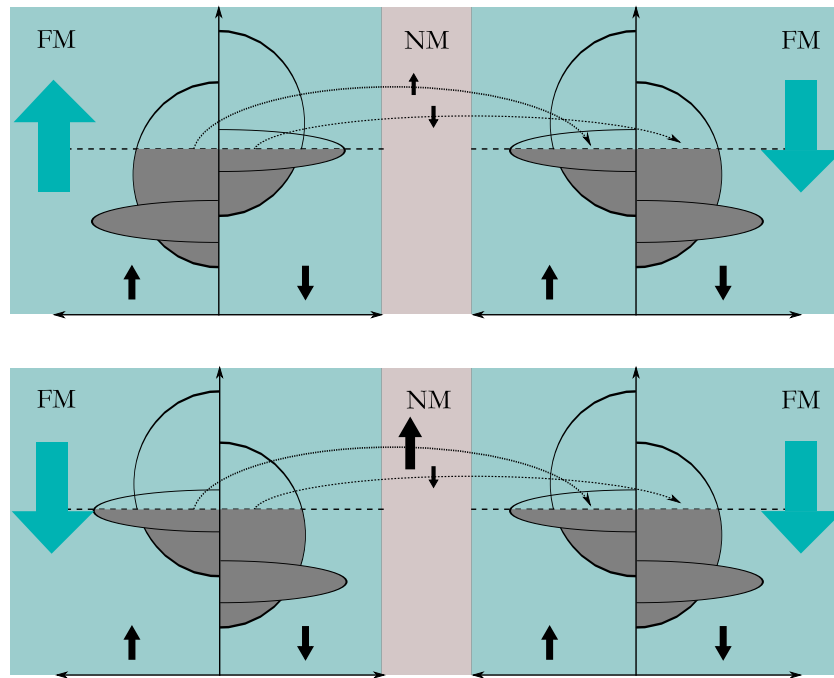


Fig. 2.9. – Intuitive explanation of the GMR effect: In a sandwich of two magnetic layers with a nonmagnetic spacer layer the resistivity depends on the relative alignment of the magnetizations. This is due to the spin-dependent band splitting in the ferromagnets, which leads to a higher DOS of at the Fermi energy (dashed line) for one spin channel. The current transport depends on the DOS on both sides of the spacer layer, hence for antiparallel alignment (top) the current is low for both spin channels, whereas for parallel alignment the current is high for one spin channel which results in an overall lower resistance as compared to the antiparallel state. (axes have the same physical units as in Fig. 2.8)

and minority carriers is low. For the parallel case, the conductivity of the channel for the majority spins increases significantly, because now enough electronic states are available on the right side. This is a very simplified picture and the microstructure of the films as well as the interfaces between the layers and the detailed bandstructure play an important role[59, 60]. GMR sensors found their way into industry when it was shown that GMR ratios as high as 65 % could be achieved at room temperature using antiferromagnetically coupled sputtered Co/Cu multilayers [61]. In contrast to spin valve sensors in this type of sensor the FM layers are aligned antiparallel at zero field and are twisted towards a 90° alignment in an external field [62]. These sensors are also very widely used in biomedical applications for the sensing of functionalized magnetic beads (e.g. [63]). MR ratios of GMR spin valves reach up to 21 %, but are typically in the 10 % range [64]. These MR ratios are calculated from a slightly different definition to Eq. 2.62, because they are normalized to the low resistance value:

$$\text{MR}[\%] = \frac{R_{\uparrow\downarrow} - R_{\uparrow\uparrow}}{R_{\uparrow\uparrow}} \cdot 100. \quad (2.66)$$

As for GMR and TMR this is the most commonly used definition, all MR values mentioned in the following will be based on Eq. 2.66.

### 2.4.3 Tunneling magnetoresistance

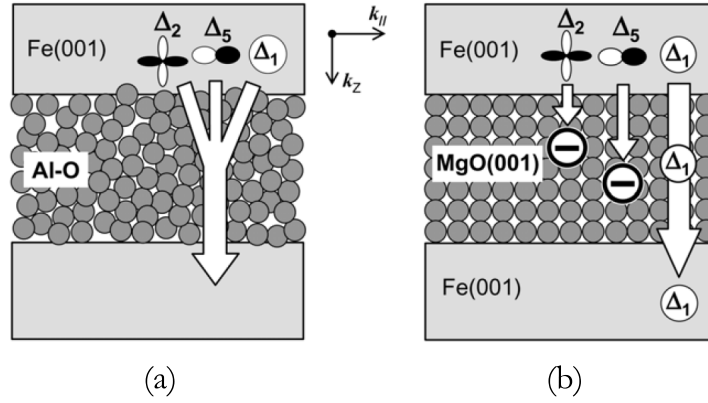


Fig. 2.10. – (a) Incoherent tunneling in amorphous barriers (eg. aluminum oxide  $\text{Al}_2\text{O}_3$ ) and (b) coherent tunneling in an MgO barrier, where only states with a certain symmetry tunnel efficiently and the others are blocked. Adapted from [21]

Tunneling magnetoresistance (TMR) was first discovered in 1975 by M. Jullière in Fe/Ge-O/Co tunnel junctions, who observed an MR ratio of 14 % at 4.2 K [65]. This work had only received broader attention after the discovery of GMR [21], and TMR at room temperature was finally measured in magnetic tunnel junctions (MTJs) with  $\text{Al}_2\text{O}_3$  barriers in 1995 [66, 67]. In this type of MTJ, which have an amorphous barrier (see Fig. 2.10 a)), the tunneling can be described by Jullière’s original model, in which the polarization  $P$  of the FM electrodes at the Fermi energy  $E_F$  is defined through the DOSs of spin-up ( $D_{\uparrow}(E_F)$ ) and spin-down ( $D_{\downarrow}(E_F)$ ) electrons by

$$P = \frac{D_{\uparrow}(E_F) - D_{\downarrow}(E_F)}{D_{\uparrow}(E_F) + D_{\downarrow}(E_F)}. \quad (2.67)$$

The tunneling currents for parallel ( $j_{\uparrow\uparrow}$ ) and antiparallel ( $j_{\uparrow\downarrow}$ ) alignment of the upper and the lower electrodes are related to  $D_{\uparrow}(E_F)$  and  $D_{\downarrow}(E_F)$  by

$$j_{\uparrow\uparrow} \sim D_{\uparrow}^{\text{upper}}(E_F)D_{\uparrow}^{\text{lower}}(E_F) + D_{\downarrow}^{\text{upper}}(E_F)D_{\downarrow}^{\text{lower}}(E_F), \quad (2.68)$$

$$j_{\uparrow\downarrow} \sim D_{\uparrow}^{\text{upper}}(E_F)D_{\downarrow}^{\text{lower}}(E_F) + D_{\downarrow}^{\text{upper}}(E_F)D_{\uparrow}^{\text{lower}}(E_F). \quad (2.69)$$

Then, the TMR ratio can be written in terms of the Fermi level polarizations of the upper and lower electrodes  $P_{\text{upper}}$  and  $P_{\text{lower}}$  as

$$\frac{j_{\uparrow\uparrow} - j_{\uparrow\downarrow}}{j_{\uparrow\uparrow}} = \frac{2P_{\text{upper}}P_{\text{lower}}}{1 - P_{\text{upper}}P_{\text{lower}}}. \quad (2.70)$$

Measured spin polarizations of FM electrodes are in the range of  $0 < P < 0.6$  and yield maximum TMR ratios of 100 % at low temperatures, which leads to a reduced TMR of  $\approx 70\%$  at room temperature. To obtain higher TMR ratios, half metallic Heusler alloys (e.g.  $\text{Co}_2\text{MnSi}$ ) which have full spin polarization  $P(E_F) = 1$  were considered to be promising candidates as electrodes. However, significantly increased TMR could not be observed at room temperature in MTJs with amorphous  $\text{Al}_2\text{O}_3$  barriers [21].

In order to achieve very high TMR ratios of theoretically  $> 1000$  % at room temperature, the barrier properties were found to play a crucial role. This was first shown in a band structure calculation by Butler *et al.* [68] for an epitaxial  $\text{Fe}(100)|\text{MgO}(100)|\text{Fe}(100)$  layer system. The crystalline MgO barrier has an additional spin filtering effect in comparison to the amorphous barrier and permits coherent tunneling of the electronic states (see Fig. 2.10 b)). The electronic states in the Fe electrodes are represented by wave functions with certain spacial symmetries, which are called  $\Delta_1$ ,  $\Delta_2'$  and  $\Delta_5$ . For incoherent tunneling through an amorphous barrier the symmetry of the electronic states is not conserved, whereas for coherent tunneling the majority-spin  $\Delta_1$ -states have an increased tunneling probability with respect to the other states. The calculated DOSs in the Fe electrodes for majority- and minority spins are given in Fig. 2.11 a)). The most interesting feature is the change of the DOS depending on the distance to the MgO layer. For the majority spins, the DOS is notably reduced at  $E_F$  in the interface layer, whereas for the minority spins it has a sharp peak. This is a strong indication for the importance of the detailed interface structure, which is indeed one of the big challenges in the fabrication of high-TMR MTJs. In Fig. 2.11 b), the tunneling DOSs (tDOS) are shown, which show the decay of states with different symmetry through the barrier. The tDOS is defined so that the incoming flux of wave functions on the very left defines  $\text{tDOS} \equiv 1$  and then becomes superimposed with the electronic waves reflected at the interfaces. The states from the left Fe electrode decay inside the MgO barrier and in the right electrode the tDOS is given by the transmitted states. It is shown, that the  $\Delta_1$ -state in the majority-spin channel has the slowest decay rate. This  $\Delta_1$ -state is not present in the minority-spin channel (not shown here), where state with the slowest decay in the minority-spin channel is the  $\Delta_5$ -state. This means that the overall conductivity of the MTJ is dominated by the  $\Delta_1$ -state in the majority spin-channel and its decay inside the MgO barrier, which also predicts an increasing TMR ratio with increasing barrier thickness for coherent tunneling.

Experimentally, the Fe-MgO-Fe system suffers from the problem of the formation of FeO at the Fe-MgO interface, which dramatically lowers the TMR. Therefore, it was tried to replace Fe by Co or CoFe, which is easier to grow without oxidation of the FM electrodes. DFT calculations predicted similarly high TMR for bcc Co-MgO-Co and CoFe-MgO-CoFe MTJs, however, Co rich electrodes tended not to grow as required in (100) texture, but rather (110) [69]. Another problem was that single crystalline MTJs did not meet the requirements for application in devices such as hard disk

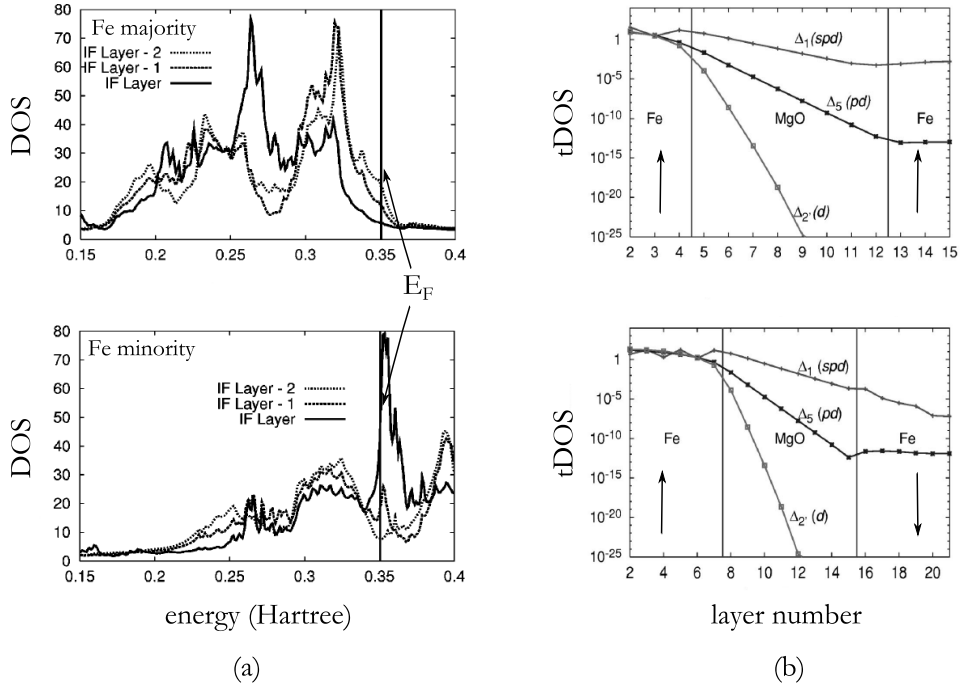


Fig. 2.11. – Density functional theory results for an epitaxial Fe(100)|MgO(100)|Fe(100) structure: (a) DOS in states/Hartree (1 Hartree  $\approx$  27 eV) for the Fe majority and minority electrons. The DOS at  $E_F$  differs significantly depending on the distance from the interface. In the interfacial layer (solid curve) the majority DOS is low whereas the minority DOS peaks, which corresponds to an inversion of the bulk properties. (b) Evolution of the tunneling DOS (tDOS) for the majority states (upper: parallel alignment, lower: antiparallel alignment): An incoming unit flow from the left has different decay rates depending on the wave function symmetry ( $\Delta_1$ ,  $\Delta_2$ ,  $\Delta_5$ ). The  $\Delta_1$  states are responsible for the high TMR ratio, because they decay quickly in the right Fe layer for antiparallel alignment. Adapted from [68]

drive (HDD) read heads, because in such applications MTJs have to work as spin valves. Therefore, a certain layer sequence is needed in order to achieve pinning of one of the magnetizations with exchange bias and interlayer exchange coupling (see Sec. 5.3.1). Furthermore, methods like molecular beam epitaxy for the fabrication of single crystalline MTJs do not meet the industrial requirements for high throughput rates. A TMR of  $\approx$  220 % was reported in 2004 for polycrystalline sputtered CoFe-MgO-CoFe junctions [70]. Reliable fabrication of MTJs with a crystalline MgO barrier using sputter deposition could be achieved with CoFeB electrodes, which are amorphous in the as-deposited state [71]. When the junctions are annealed to a temperature of at least 300°C the CoFeB electrodes start to crystallize from the MgO interface, which provides the necessary conditions for coherent tunneling [72]. To date, the most prominent application of TMR sensors is as magnetoresistive read heads in hard disk drives. TMR outperform CIP-GMR read heads due to their better signal-to-noise ratio and the easier fabrication of the magnetic shield, which is needed to read back the magnetic medium with high resolution [73]. In other

fields such as automotive applications, GMR is still the preferred technology, because tunnel barriers are sensitive to deterioration due to voltage peaks. Furthermore, the barrier itself represents a source of noise phenomena, that are not present in all-metallic systems (see Sec. 2.1). This higher MR ratio of TMR sensors often does not compensate the increased complexity in the fabrication of robust MTJs with low resistances.

## Motivation

The biomedical application and the preceding work on TMR fluxgate sensors were the motivation for pursuing the research on TMR fluxgate sensors at the AIT (Austrian Institute of Technology). Biomagnetism and magnetocardiography (MCG) in particular (Sec. 3.1) as well as the first theoretical results on TMR fluxgate sensors are the subject of this chapter. Also, based on the information given in Chapter 2 the TMR fluxgate sensing principle will be explained in detail in Sec. 3.2.

### 3.1 Biomagnetism

Biomagnetic fields are produced by neural activity in human tissue and organs such as the heart and the brain. Ionic currents are the result of the metabolism of the cells in the human neural system and hence represent a transformation from chemical to electric energy. The biomagnetic field of the human heart was first detected by Baule and McFee [74] in 1963, who used a setup of coils with 2 million windings and ferrite cores. With the invention of the Superconducting Quantum Interference Device (SQUID) several years later the measurement could be improved to become comparable to state-of-the-art electrocardiogramms (ECGs) [75]. Magnetocardiography (MCG) is based on the same biophysical phenomena in the human body as electrocardiography (ECG). The latter is a very popular and well understood method used by physicians to monitor the heart rate and to get information about possible cardiac diseases by investigating the shapes (morphology) of the single beats. For the ECG, the voltage measured on a single lead can be modelled as

$$V_{LE} = \int_V \mathbf{j}_{LE} \cdot \mathbf{j}^i dV \quad (3.1)$$

where  $\mathbf{j}_{LE}$  is the surface current on the conductor - i.e. the human torso - that is connected between the leads of the ECG device and  $\mathbf{j}^i$  are the biological current source distributed inside the volume  $V$  [76]. Eq. 3.1 is a representation of the Maxwell equations for the electrical field:

$$\nabla \cdot \mathbf{E} = \frac{\rho}{\epsilon_0} \quad (3.2)$$

$$\nabla \times \mathbf{E} = -\frac{\partial \mathbf{B}}{\partial t} \quad (3.3)$$

Here,  $\rho$  denotes a charge density and  $\mathbf{B}$  a magnetic field. Maxwell's equations for the corresponding magnetic field  $\mathbf{B}$  read

$$\nabla \cdot \mathbf{B} = 0 \quad (3.4)$$

$$\nabla \times \mathbf{B} = \mu_0 \mathbf{j} + \mu_0 \epsilon_0 \frac{\partial \mathbf{E}}{\partial t} \quad (3.5)$$

Eq. 3.5 is also known as Ampère's Law with an additional term for the displacement current and is the physical basis of biomagnetism. The biomagnetic fields observed in humans range from femto-Tesla for the neural currents generated by the brain to several pico-Tesla for an adult heart. The magnetic fields measured at the body surface have one important advantage over the electrical fields detected by ECG: They are less affected by the surrounding medium - i.e. human tissue etc. - and hence undergo less distortion. This is of special importance for the prenatal monitoring of the fetal heart activity.

The heart rate is an important indicator for the fetal condition. The commonly

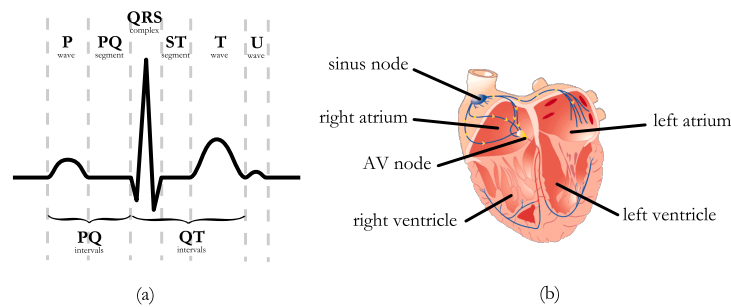


Fig. 3.1. – (a) typical ECG signal, P-wave: atrial depolarization from the sino-atrial node to the atrio-ventricular (AV) node, PR interval: time, that the electrical pulse takes to travel from the sinus node to the AV node, QRS complex: rapid depolarization of the left and right ventricles, ST interval: depolarization of the ventricles, T-wave: repolarization of the ventricles, QT interval: varies with heart rate, U-wave: low amplitude, not present in most cases. (b) human heart with electrophysiologically relevant parts, adapted from [77].

used method to monitor the fetal heart rate is Doppler sonography. However, this method cannot resolve the beat-to-beat variability. The amplitudes of a fetal electrocardiogram (fECG) vary to a large degree with gestational age. During the 28<sup>th</sup> and the 32<sup>nd</sup> week the fECG signals do not give reliable information about the actual fetal heart rate. This is due to the appearance of the vernix caseosa, a layer which protects the fetus from infections during the late pregnancy and during delivery and with isolating electrical properties. Oostendorp and van Oosterom [78] show, that in contrast to the fECG the amplitudes of a fetal magnetocardiogram (fMCG) do not undergo a comparable attenuation. Therefore, the prenatal diagnosis of congenital cardiac diseases such as the QT syndrome is made possible using fMCG [79].

The QT syndrome is an inherited disease and is considered to be one of the causes



for sudden infant death. Its name stems from a characteristically prolonged QT interval. For the diagnosis of a number of congenital diseases it is important to have an exact measurement of the waveform characterizing the human heart activity (see 3.1) as well as high beat-to-beat accuracy. Here, the fECG is still the method of choice, which at present is also the only method suitable for long-term domiciliary monitoring of the fetal heart rate. Because for MCG Superconducting Quantum Interference Devices (SQUIDs) are the only available sensors at present which reach the required detectivities, an fMCG can only be recorded in the clinic as SQUIDs require cooling down to 4 K using liquid helium. As for the fECG, the amplitudes of the fMCG peaks cannot be used quantitatively as they depend on the distance of the sensor to the fetal heart. However, the fMCG signals can be detected with higher reliability throughout gestation and usually have a better signal-to-noise ratio [80]. In order to make fMCG an easy-to-use method in everyday clinical life, attempts have also been made to realize high- $T_C$  SQUID fetal heart rate monitors without magnetic shielding and standalone table-size cryocoolers. However, the required detectivity of  $10 \text{ fT}/\sqrt{\text{Hz}}$  cannot be achieved with the currently available high- $T_C$  SQUIDs. Furthermore, there is a need for multi-channel devices in order to compensate for the sensor position and orientation of the fetus. The magnitude of the QRS-complex in a fMCG is in the order of pico-Tesla, whereas for an adult MCG it is about 100 times larger. The correct classification of the type of heart disease is crucial for possible antenatal drug treatment and the choice of a specialized clinic for delivery [81]. The positioning of the sensors play a crucial role for a the proper detection of the fetal heart rate with as few signal as possible from the mother's heart. Digital filter algorithms can be applied to remove unwanted signals from the surroundings, such as the power line frequencies and their harmonics, as well as measured field gradients. Adaptive filters show a good performance in a system tested at the Biomagnetic Center in Jena [82], however, they are not suitable for real-time monitoring. Modern MCG systems consist of multi-channel devices of up to 64 SQUID sensors [83], in ref. [84] fMCG recordings from a 55-channel system are presented out of which only three channels are selected, that have the highest signal amplitude (see 3.2). Such data provide valuable information on the beat morphology variations to the clinician.

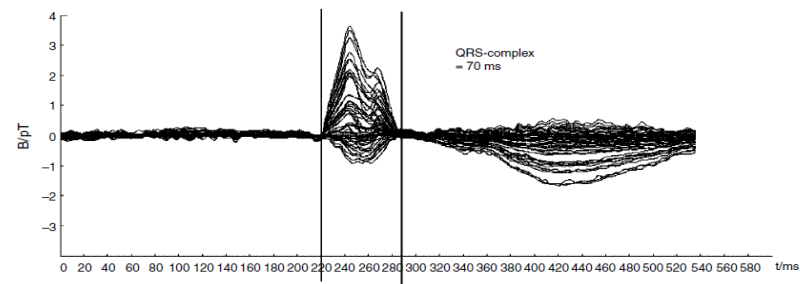
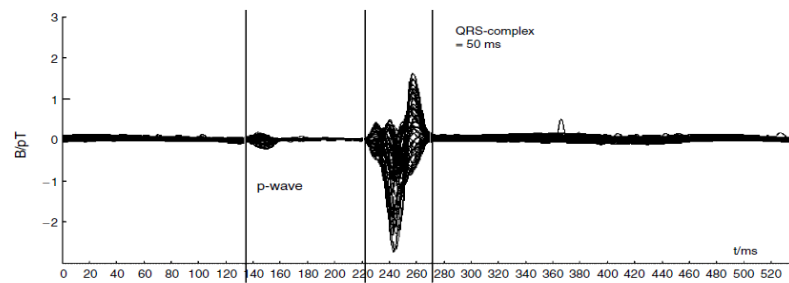
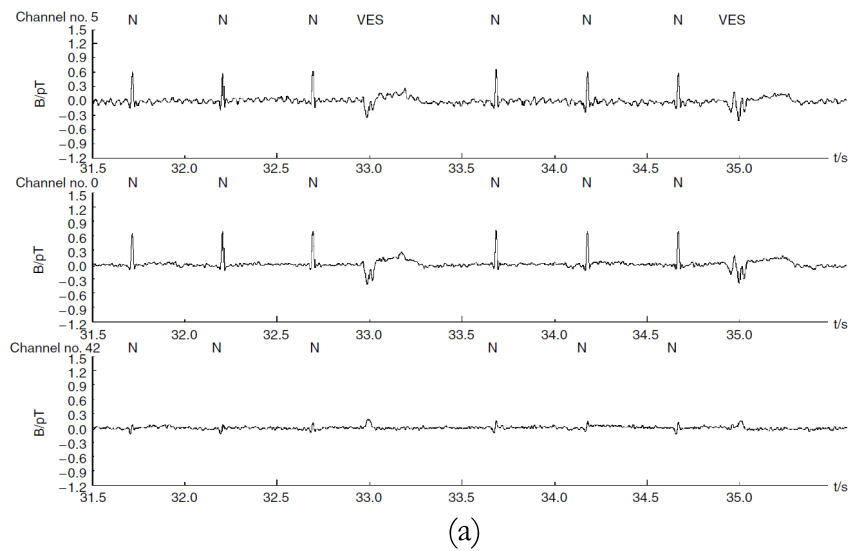


Fig. 3.2. – fMCG data recorded with a 55-channel system at the Division for Biosignals and Imaging Technologies at the University of Ulm (Germany) (adapted from [84]): (a) MCG recordings of a fetus with ventricular extrasystoles (VES) (b) top: averaged normal heart beats (marked with N in the above recordings), bottom: averaged VES beats, note the different duration of the QRS-complex. For data analysis the software package OMEGA (Open Magnetic and Electric Graphic Analysis) was used [85].

## 3.2 The tunneling magnetoresistance fluxgate magnetometer

The idea behind the tunneling magnetoresistance fluxgate magnetometer (TMR fluxgate in the following) is to combine two measurement techniques for magnetic fields in order to achieve high detectivity with a sensor that is compatible to CMOS fabrication. The sensing element is a magnetic tunnel junction as described in Section 2.4.3 to which the measurement principle of the fluxgate magnetometer (see Sec. 2.3) is applied. The fabrication of MTJs has been optimized for years in the hard disk industry to achieve low resistance-area products in order to obtain high signal-to-noise ratios for hard disk read heads. However, TMR sensors suffer from their pronounced  $1/f$  noise, which substantially limits their detectivity for near-DC magnetic fields (see also Sec. 2.1). On the contrary, fluxgate magnetometers have detectivities in the range of interest for biosensing down to  $\text{pT}/\sqrt{\text{Hz}}$ , but are in general not compatible with standard IC fabrication methods. Several prototypes for integrated fluxgate sensors have been developed reaching detectivities of  $70\text{nT}/\sqrt{\text{Hz}}$  [49] [50], but they do not reach the high signal-to-noise ratios obtained by optimized core-coil setups.

In fig. 3.3 the measurement principle of the TMR fluxgate is illustrated. Consider an

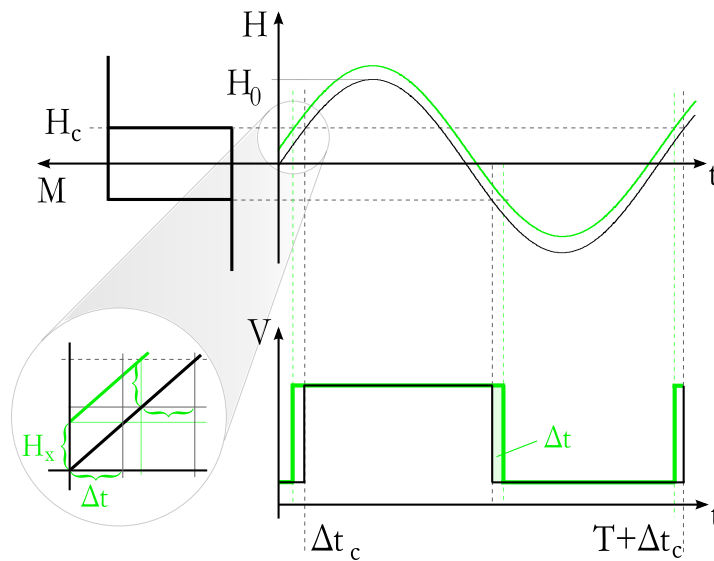


Fig. 3.3. – Generation of the TMR fluxgate signal: The MTJ is periodically switched from its high to its low resistance state by an external driving field  $H(t)$  with amplitude  $H_0$ . This generates a square-wave like voltage signal (black). If a DC field  $H_x$  is applied parallel to the driving field, the duty cycle of the voltage signal is changed (green), because the free layer of the MTJ switches earlier/later by a time interval  $\Delta t$ .

easy-axis hysteresis loop  $M(H)$  of the free layer of an MTJ with a coercive field  $H_C$ . If an alternating external field  $H(t)$  with an amplitude  $H_0$  is applied parallel to the

easy axis, the MTJ voltage switches from high to low with the frequency of  $H(t)$ . The dwell times for the high and low state is  $T/2$  in both cases, i. e. the idealized voltage signal corresponds to a square wave with a duty cycle of 50%. Furthermore, the voltage signal is shifted with respect to  $H(t)$  by a time interval  $\Delta t_C$ , that originates from the finite coercive field  $H_C$ . This phase shift can be ignored in the following, as the period  $T$  can be shifted by  $\Delta t_C$  to simplify the analysis without loss of signal power. When calculating the Fourier series of the square wave signal with a duty cycle of 50% it is found that it consists only of odd harmonics

$$V(t) = \frac{\tilde{V}_0}{2} + \tilde{V}_1 \sin(\omega t) + \tilde{V}_3 \sin(3\omega t) + \tilde{V}_5 \sin(5\omega t) + \dots \quad (3.6)$$

with  $\tilde{V}_0, \tilde{V}_1, \tilde{V}_3, \tilde{V}_5, \dots$  being the Fourier coefficients (see also sec. 5.2). With the application of an additional DC field  $H_x$  to the alternating field  $H(t)$  the duty cycle becomes asymmetric (green signals in fig. 3.3) and even harmonics occur as well in the signal in eq. 3.2. As already mentioned in sec. 2.3 the second harmonic is used as a linear measure for the strength of  $H_x$ . For the TMR fluxgate sensor the second harmonic amplitude can be calculated by modeling the time domain voltage signal as [86]

$$V(t) = V_{\text{low}} + \Delta V \cdot \Theta \left( t - \frac{T}{2} - \Delta t \right) \quad (3.7)$$

For small fields  $H_x$   $\Delta t$  will be small, too, and hence can be defined using the finite difference approximation for the first derivative of  $H(t)$  (see also the inset with the magnified view in fig. 3.3):

$$\frac{H_x}{\Delta t} = \left. \frac{dH(t)}{dt} \right|_{t=0} = H_0 \omega \cos \omega t|_{t=0} = H_0 \omega \quad (3.8)$$

$$\Rightarrow \Delta t = \frac{1}{\omega} \frac{H_x}{H_0} \quad (3.9)$$

then carrying out the Fourier transformation

$$\tilde{V}_2 = \frac{2\Delta V}{T} \int_{-\Delta t}^{T-\Delta t} \Theta \left( t - \frac{T}{2} - \Delta t \right) \cos 2\omega t dt \quad (3.10)$$

$$= \frac{2\Delta V}{T} \int_{-\Delta t}^{T/2+\Delta t} \cos 2\omega t dt \quad (3.11)$$

$$\frac{2\Delta V}{\pi} \frac{H_x}{H_0} \sqrt{1 - \left( \frac{H_x}{H_0} \right)^2} \approx \frac{2\Delta V}{\pi} \frac{H_x}{H_0}. \quad (3.12)$$

for  $H_x \ll H_0$  and for small  $\Delta t$ . Here, the period of observation was shifted by  $\Delta t_C$  because a phase lag of  $V(t)$  with respect to  $H(t)$  does not affect the absolute value of the second harmonic amplitude.

The step function approximation from Eq. 3.7 is exact for a single domain particle switched along its easy axis (see Sec. 4.1). For a micron-sized magnetic element

domains will be formed and the switching of the single domains is usually assumed to follow a Gaussian distribution

$$D(H, H_C, \sigma) = \frac{1}{\sqrt{2\pi}\sigma} e^{-\frac{(H-H_C)^2}{2\sigma^2}}. \quad (3.13)$$

Integration of the distribution and scaling with the voltage difference  $\Delta V$  that originates from the TMR effect gives the voltage signal generated by a TMR fluxgate sensor as [86]

$$\frac{\Delta V}{V_{\text{low}}} = \frac{1}{2} \operatorname{erf} \left( \frac{(H \pm H_C)^2}{\sqrt{2}\sigma} \right), \quad (3.14)$$

where  $V_{\text{low}}$  is the voltage in the low resistance state and  $H = H(t) = H_x + H_0 \sin(2\pi ft)$  comprises all external magnetic fields.  $\sigma$  is the standard deviation of the switching fields and is hence given in  $A/m$ . Using Eq. 3.14 a time domain

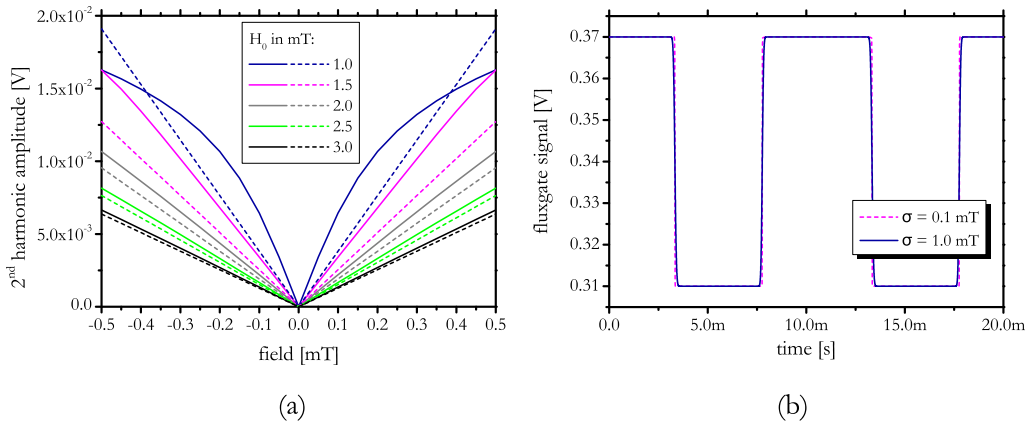


Fig. 3.4. – Sensor characteristics  $V_2(H_x)$  for varying switching field amplitude  $H_0$  (solid lines: simulation, dashed lines: analytical). Other parameters:  $\mu_0 H_C = 1$  mT,  $V_{\text{low}} = 0.31$  V,  $\Delta V = 0.06$  V,  $\mu_0 \sigma = 1$  mT

TMR fluxgate signal was generated in MATLAB<sup>®</sup> and Fourier transformed using the built-in Fast Fourier Transformation (FFT) function. From the frequency domain data, the value corresponding to the second harmonic at  $2f$  gives the output signal of the TMR fluxgate sensor. The sensor characteristics  $V_2(H_x)$  is plotted in Fig. 3.4 a together with the analytical result from Eq. 3.12 (dashed lines). Here,  $\mu_0 \sigma$  was set to 1 mT. In Fig. 3.4 b the time domain signals are shown for  $\mu_0 \sigma = 1$  and 0.1 mT.  $\mu_0 \sigma = 0.1$  mT almost exactly models a step function and for  $\mu_0 \sigma = 1$  mT the time domain signal most significantly differs at the transition to saturation, which mostly contributes to higher harmonics than the second. Nevertheless, there remains a discrepancy between the simulated (discrete) and the analytical second harmonic, and we have for the sensitivities

$$\frac{(\Delta V_2 / \Delta H_x)_{\text{analytical}}}{(\Delta V_2 / \Delta H_x)_{\text{discrete}}} \approx 1.1. \quad (3.15)$$

Therefore, the analytical sensitivity

$$\left(\frac{\Delta V_2}{\Delta H_x}\right)_{\text{analytical}} = \frac{2}{\pi} \frac{\Delta V}{H_0} \quad (3.16)$$

can be taken as an upper ideal estimate in the absence of discretization errors. This result is useful for determining the tunable factors for the sensitivity. The voltage difference  $\Delta V$  is in the numerator and hence an increasing TMR ratio is beneficial for the sensor sensitivity. For the driving field amplitude  $H_0$  the opposite is true. It has to be kept as low as possible ( $H_0 > H_C$ !) in order to detect small changes in the external DC field  $H_x$ . Sensor characteristics in Fig. 3.4 a are given for different field amplitudes  $H_0$  starting at  $\mu_0 H_0 = \mu_0 H_C = 1$  mT and increased in steps of 0.5 mT.

## Theoretical Modeling

In this chapter the theoretical models will be discussed in detail that give the foundation for the understanding of the detection limit of the TMR fluxgate sensor. During the signal generation of the sensor the magnetization of the free layer is repeatedly switched which generates the time domain magnetoresistance signal. Depending on the magnitude of an additional field applied parallel to the driving AC field the signal changes its duty cycle, which leads to a change in the spectrum. Because the additional field is supposed to be very weak ( $\sim 10^{-12}$  T) it will be important to determine the noise that is present during the switching of the magnetization. This noise will lead to jitter in the time domain signal, which accordingly affects the spectrum and hence the second harmonic detection. As already discussed in Sec. 2.1, thermal fluctuations are the root cause for systems showing noisy behavior. This is also true for magnetic systems, where the magnetic moments are subject to agitation by random thermal forces.

In the following we will derive a thermal switching field distribution for a single spin particle that serves as a model for the free layer's magnetization in the TMR fluxgate sensor. The zero temperature switching behavior of such a single domain particle is described by the Stoner-Wohlfarth model, which gives the stable states for the magnetization and the energy barrier by which they are separated (Sec. 4.1). We will then use transition state theory to model thermal activation over this energy barrier, which strongly depends on the magnitude of the external field (Sec. 4.2). The field-rate dependence of the coercivity of a magnetic material at finite temperature is a consequence of this dependence and will be discussed in Sec. 4.2.1. An important extension to the existing models is added by the explicit derivation of the switching field distribution, which also allows us to define a standard deviation of the switching fields. The standard deviation is the key to understanding the noise affecting the TMR fluxgate sensor. However, the results presented in Secs. 4.2.2 and 4.2.3 are also of broader relevance as they represent a main noise source in magnetic recording media [87].

In Sec. 4.3 we introduce modeling of the TMR fluxgate signal by the Monte Carlo simulation technique. Using the Metropolis algorithm the time domain signal of the TMR fluxgate sensor can be generated and then used for further analysis (see Chapter 6). We also retrieve the analytical result for the switching field distribution by the simulation and compare it to a simulation of the Langevin equation of a magnetic moment, which yields a result for the switching field distribution based on

the stochastic microscopic equation of motion that agrees remarkably well with the analytical results and the Monte Carlo simulation.

## 4.1 The Stoner-Wohlfarth model

A widely used model to describe the magnetization reversal is the Stoner-Wohlfarth model [88]. It describes the coherent rotation of the magnetization in a single-domain particle with uniaxial anisotropy. Such a particle with a magnetic polarization  $\mathbf{J} = \mu_0 \mathbf{M}$  ( $\mathbf{M}$  is the magnetization) is sketched in fig. 4.1. Its free energy in an external field  $\mathbf{H}$  consists of contributions from the anisotropy energy and the magnetostatic energy densities  $E_K$  and  $E_H$

$$E = E_K + E_H. \quad (4.1)$$

$E_H$  is the energy per unit volume defined by the relative alignment of the magnetization  $\mathbf{M}$  to the external field  $\mathbf{H}$ :

$$E_H = -\mu_0 \mathbf{H} \cdot \mathbf{M} \quad (4.2)$$

The anisotropy energy density  $E_K$  consists of various contributions originating from material properties and symmetry. The most relevant contributions to  $E_K$  within the framework discussed in this thesis originate from magnetocrystalline and shape anisotropy.

### 1. Magnetocrystalline anisotropy

This contribution stems from the fact that depending on the crystalline phase of the material of the particle, the magnetization will have a preferred crystallographic direction for alignment. In the crystal field of the material, i.e. the atomic surroundings, certain directions for relative atomic spin alignment are energetically more favorable. With  $a, b, c$  being the crystallographic directions in the unit cell the magnetocrystalline anisotropy energy density can be written as

$$E_{K,\text{crystal}} = K_1(a^2 + b^2) = K_1(1 - c^2) = K_1 \sin^2 \beta, \quad (4.3)$$

where in the last step  $c = \cos \beta$  was used and  $\beta$  being the azimuthal angle. This is a phenomenological model and higher order terms  $K_2 \sin^4 \beta, K_3 \sin^6 \beta, \dots$  can be included to increase accuracy [89].

### 2. Shape anisotropy

The shape anisotropy energy of a magnetic particle is determined by the interaction of the magnetic dipole moment with a magnetization  $\mathbf{M}$  with the



stray field or demagnetizing field  $\mathbf{H}_D$ . It can be written as [89] (the dimension here is [J], not [J/m<sup>3</sup>!])

$$E_{K,\text{shape}} = -\frac{\mu_0}{2} \int_V \mathbf{M}(\mathbf{r}) \cdot \mathbf{H}_D(\mathbf{r}) dV. \quad (4.4)$$

There is usually no trivial solution to this volume integral, however, for an ellipsoid of revolution that is homogeneously magnetized, the shape anisotropy energy is given by

$$E_{K,\text{ell}} = \frac{\mu_0}{2} M_s^2 (D_x \alpha_x^2 + D_y \alpha_y^2 + D_z \alpha_z^2) V \quad (4.5)$$

where  $D_i$  are the demagnetizing factors from  $\mathbf{H}_D = -D\mathbf{M}$  and  $\alpha_i$  are the direction cosines. For a thin film, the shape anisotropy energy is [51]

$$E_{K,\text{tf}} \propto \frac{\mu_0}{2} M_S^2 \cos^2 \beta V, \quad (4.6)$$

where  $\beta$  denotes the angle of the magnetization to the surface normal. This means, that for thin films the energy is minimized if the magnetization is oriented in-plane. For the ellipsoid shown in Fig. 4.1 the magnetization is in an equilibrium state when aligned along the long axis, if there is no magnetocrystalline anisotropy present.

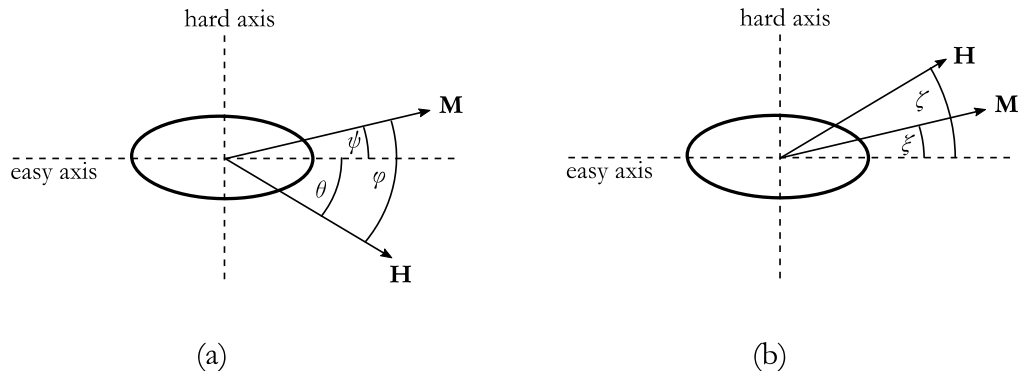


Fig. 4.1. – Sketch of a Stoner-Wohlfarth particle with uniaxial anisotropy: (a) angle names as given by Stoner and Wohlfarth in [88] and used for the free energy ansatz in Eq. 4.7, (b) angle names for the free energy ansatz from Eq. 4.8 which is more commonly found in textbooks such as [51] and [89].

The energy balance from Eq. 4.1 defines the equilibrium alignment of the magnetization  $\mathbf{M}$  with respect to the external field. When no field is applied, the magnetization of the particle will align along the direction with minimal total anisotropy energy. This direction defines a so-called easy axis for the particle, which means, that there is no cost in energy ( $E_K = 0$  J) for the magnetization to point along this axis. If we assume uniaxial anisotropy, i.e. all contributions to the anisotropy point along on axis, which corresponds to  $\psi = 0$  in Fig. 4.1 the energy minimum is achieved for

$\theta = 0$  in zero field with  $\varphi = 0$ . Alignment of  $\mathbf{M}$  along the hard axis would require a maximum of energy  $E_K = K_{\text{eff}}V$  and hence does not correspond to an equilibrium state of the magnetization.

In the Stoner-Wohlfarth model an elliptical particle is considered, in which all contributions to the anisotropy energy are aligned parallel to each other. In the case of an elliptical particle the easy axis is well defined by the long axis of the ellipse. In this configuration the stray field energy and hence the shape anisotropy energy is minimized.

Eq. 4.1 gives an energy landscape with minima and maxima and is an expression for the (Helmholtz) free energy  $F = E - TS$  at a temperature  $T = 0$  K and the entropy  $S$ . The free energy is used to study thermodynamic systems that are in contact with a heat bath and form a canonical ensemble, where the number of particles stays constant [90]. In the original paper [88] E.C. Stoner and E.P. Wohlfarth came up with the following ansatz for the normalized free energy density  $\eta$ :

$$\eta = \frac{E}{2KV} = -\frac{1}{4} \cos 2(\varphi - \theta) - h \cos \varphi. \quad (4.7)$$

$h$  is the length of the external field vector  $\mathbf{H}$  normalized by the easy axis switching field or uniaxial anisotropy field  $H_K = 2K/J_S$ ,  $\varphi$  is the angle of the magnetization  $\mathbf{M}$  with respect to the applied field and  $\theta$  is the angle between the field and the easy (long) axis of the particle. More frequently, Eq. 4.7 is written as

$$E = K \sin^2 \xi - \mu_0 H M_S \cos(\xi - \zeta) \quad (4.8)$$

which is the form most commonly found in textbooks such as Refs. [51, 89]. Here, we used the fact that the cosine function is symmetric in its argument, so that  $\cos(\zeta - \xi) = \cos(-(\xi - \zeta)) = \cos(\xi - \zeta)$ .

In order to find the equilibrium positions for the magnetization it is necessary to investigate the free energy landscape that is given by Eq. 4.7. In Fig. 4.2 the free energy is plotted with respect to  $\psi$  for the field  $h$  applied along the easy axis ( $\theta = 0$ ) and  $h$  applied along  $\theta = \pi/4$  for values of  $h$  below and above the switching or coercive field  $h_c$ . For  $h = 0$  there are two energy minima, which correspond to  $\mathbf{M}$  pointing along the unit vector of the easy axis ( $\psi = 0$  for parallel and  $\psi = \pi$  for antiparallel alignment). These two states are separated by an energy barrier. Fig. 4.2 shows the case where  $\mathbf{M}$  initially points along the positive direction of the easy axis. When  $h$  is increased in the opposing direction the energy minimum at  $\psi = 0$  gets lifted and turns into a metastable state, which means that it is no longer a global minimum of the free energy. When  $h$  is further increased eventually the maximum in the free energy separating the two minimum energy states turns into a saddle point and  $\mathbf{M}$  switches towards the direction of  $h$ . For  $\theta = 0$  this happens at  $h \equiv h_c(\theta = 0) = 1$ . For  $\theta = \pi/4$  we already see a saddle point in the free energy  $\eta$  for  $h < 1$ , which means that the switching field is notably reduced if the field is

applied at  $45^\circ$ , i.e.  $h_c(\theta = \pi/4) < h_c(\theta = 0)$ . This relation can also be read from the well-known Stoner-Wohlfarth astroid (Fig. 4.3), which will be introduced in the following. It is a graphical representation of the 2d-field components required to switch the magnetization between its two equilibrium positions.

To derive the equilibrium angular positions, the minima of the free energy functional have to be found. This is done by setting the first derivative of Eq. 4.7 to zero

$$\frac{\partial \eta}{\partial \varphi} = \frac{1}{2} \sin 2(\varphi - \theta) + h \sin \varphi = 0. \quad (4.9)$$

Furthermore, the second derivative has to be a positive number if the extremum is indeed a minimum, which gives

$$\frac{\partial^2 \eta}{\partial \varphi^2} = \cos 2(\varphi - \theta) + h \cos \varphi \geq 0. \quad (4.10)$$

If  $\partial^2 \eta / \partial \varphi^2$  is equal to zero, one of the minima in the free energy becomes a saddle point. This means that the energy barrier which is initially separating the minima vanishes and the magnetization switches to another stable position, which is lower in energy with respect to the direction of the field  $\mathbf{H}$ . The field at which this is happening is called the critical or switching field  $H_C$ .

Eqs. 4.9 and 4.10 give a set of two equations from which the angular position

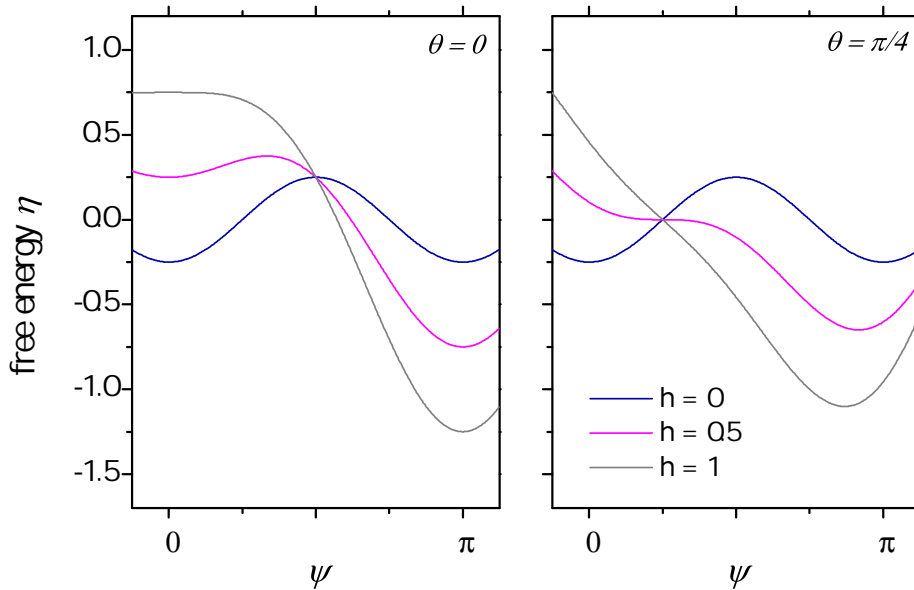


Fig. 4.2. – Free energies for the external field  $h$  applied at angles  $\theta = 0$  (easy axis) and  $\theta = \pi/4$  as a function of the angle  $\psi$  between the magnetization and the field. Uniaxial anisotropy is assumed.  $h$  has the opposing sign to the direction to which the magnetization is pointing initially, so the free energy functional plotted here reads  $\eta = -0.25 \cos 2\psi + h \cos(\psi + \theta)$ .

$\psi = \varphi - \theta$  of  $\mathbf{M}$  with respect to the easy axis can be determined for varying field

angles  $\theta$ . Multiplying Eq. 4.9 by  $\cos \varphi$  and subtracting Eq. 4.10 multiplied by  $\sin \varphi$  (see Appendix A.1) leads to the relation

$$\tan^3 \psi = \tan \theta. \quad (4.11)$$

If we consider that  $h$  has a component parallel to the easy axis  $h_x = h \cos \theta$  and a component perpendicular to the easy axis  $h_y = -h \sin \theta$  Eq. 4.11 can be written as

$$h_x = -\cos^3 \psi \quad (4.12)$$

$$h_y = \sin^3 \psi \quad (4.13)$$

because  $\tan \theta = \sin \theta / \cos \theta$ . These two equations give the switching fields in the  $xy$ -plane for the Stoner-Wohlfarth particle from Fig. 4.1. Their geometric representation is called the Stoner-Wohlfarth astroid in Fig. 4.3 b. The curves defining the astroid follow the relation

$$h_x^{2/3} + h_y^{2/3} = 1 \quad (4.14)$$

A mathematical relation of the magnetization to the external field can be derived from the Eq. 4.9. Solving Eq. 4.9 for  $h$  and defining the component of the magnetization which is parallel to  $\mathbf{H}$  as  $m \equiv \cos \varphi$  gives

$$h_{\pm} = m \cos 2\theta \pm \frac{2m^2 - 1}{2\sqrt{1 - m^2}} \sin 2\theta. \quad (4.15)$$

The two solutions with opposing signs are plotted as the inverse function of Eq. 4.15  $m(h)$  in Fig. 4.3 a for  $\theta = \pi/4$ . When  $h$  is reduced coming from positive values  $m$  will change according to the  $+$  in Eq. 4.15. When the negative switching field is reached the local minimum turns into a saddle point and  $m$  jumps to the branch with the  $-$  sign. Increasing the field from negative values causes  $m$  to follow the  $-$  branch first and jump to the  $+$  at the positive switching field.

For a given field  $h$  which lies inside the astroid, the magnetization angles corresponding to the minima in the free energy (Eq. 4.7) can be constructed by drawing the inner tangents to the astroid through  $h$ . The four tangents give the possible magnetization directions with respect to the easy axis. However, only two of them correspond to the stable solutions where the free energy has minima. The two other solutions correspond to a saddle point and a maximum [91].

Strictly spoken, the Stoner-Wohlfarth model is only applicable to single domain particles, i.e. particles which have a radius smaller than a critical value  $R_{\text{crit}}$ , which can be estimated from the energy cost to form a certain type of domain wall. For a spherical particle the single domain state energy is given by  $E_{\text{SD}} = \frac{1}{6} \mu_0 M_S^2 V$ . The energy balance when a  $180^\circ$  domain wall is formed between two domains of half the sphere's volume reads [51]

$$E_{\text{DD}} = \frac{1}{6} \mu_0 M_S^2 \frac{V}{2} + \pi r^2 \sigma_W,$$

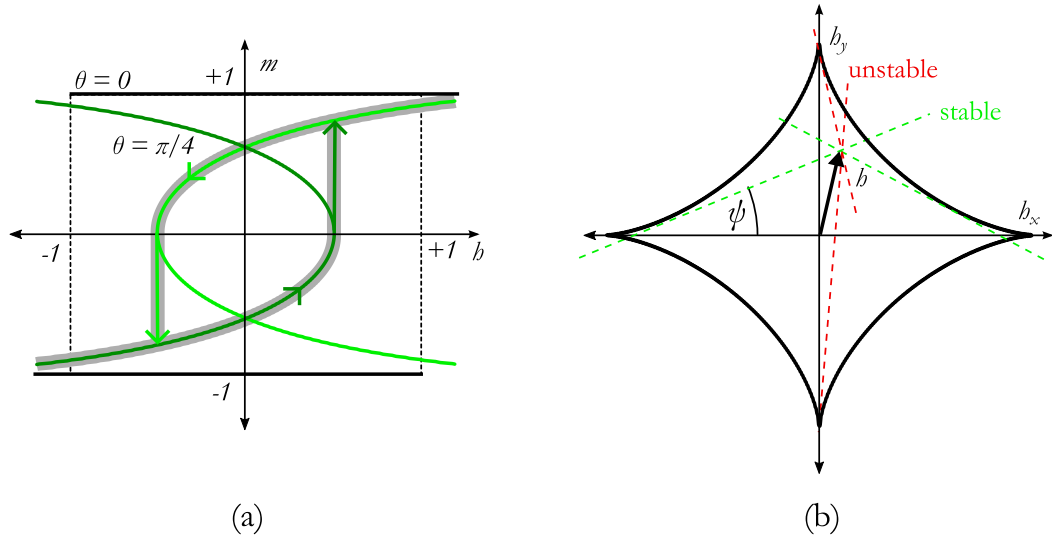


Fig. 4.3. – (a) Stoner-Wohlfarth hysteresis loops for the field applied along the easy axis ( $\theta = 0$ ) and  $\theta = \pi/4$ , where the lowest switching field is required. The green curves are the two solutions for the magnetization from Eq. 4.15. (b) Stoner-Wohlfarth astroid: This is a graphical representation of Eqs. 4.13. For a given field inside the astroid there exist in total four solutions for the magnetization, of which only two are the stable solutions corresponding to the minima in the free energy  $\eta$  from Eq. 4.7.

where  $\sigma_W$  denotes the domain wall energy per unit area in  $\text{J}/\text{m}^2$ , i.e. the energy required to rotate neighboring spins away from each other. If the single domain state is supposed to be energetically more favorable  $E_{\text{SD}} < E_{\text{DD}}$  has to apply. With  $V = \frac{4}{3}\pi R^3$  from this the critical radius can be derived as

$$R_{\text{crit}} = \frac{9\sigma_W}{\mu_0 M_S^2}. \quad (4.16)$$

Above this radius, it becomes energetically more favorable to form a domain wall in order to minimize the total energy. When applying the Stoner-Wohlfarth model to a system which has dimensions larger than  $R_{\text{crit}}$  the switching are usually larger than the measured fields. Calculation of  $R_{\text{crit}}$  is not trivial, but for spins on a cubic lattice and a simple form of the anisotropy energy density  $E = K \sin^2 \theta$  the domain wall energy can be derived as  $\sigma_W = \pi\sqrt{AK}$ , where  $A = 2JS^2/a$  is the exchange stiffness in  $\text{J}/\text{m}$ . Here,  $a$  denotes the lattice constant, and  $S$  and  $J$  are the spin quantum number and the quantum-mechanical exchange integral from the Hamiltonian of the nearest-neighbor Heisenberg model [51]

$$\mathcal{H} = - \sum_{\langle i,j \rangle} JS_i \cdot S_j. \quad (4.17)$$

For a cobalt with  $K = 5 \cdot 10^5 \text{ J}/\text{m}^3$ ,  $A = 6.5 \cdot 10^{-11} \text{ J}/\text{m}$ ,  $M_S = 1.4 \cdot 10^6 \text{ A}/\text{m}$  and  $a = 3 \cdot 10^{-10} \text{ m}$  the critical radius for the transition from the single domain to the two-domain state according to Eq. 4.16 would be  $R_{\text{crit}} = 65.2 \text{ nm}$  [92].

## 4.2 Thermally activated magnetization switching

In this section the basic framework of transition state theory will be introduced, which is used in numerous scientific areas to describe various physical phenomena. These problems are all described by transition processes between two metastable states separated by an energy barrier. The rate at which the system undergoes a transition from one metastable state to the other (escape rate) has to be much slower than the rate governing the intrinsic dynamics of the physical processes in the system and is given by the Van't Hoff-Arrhenius Law

$$f = f_0 \exp\left(-\frac{E_B}{k_B T}\right), \quad (4.18)$$

where  $E_B$  is the energy barrier separating the two metastable states and  $f_0$  is a prefactor which size depends on the dynamic properties.  $f_0$  is also called attempt frequency, which refers to an understanding of the prefactor as a rate at which the system ‘‘attempts’’ to cross the barrier.  $E_B/(k_B T)$  gives the ratio of the barrier to the energy of the thermal fluctuations  $E_{\text{noise}}$ . Eq. 4.18 holds as long as

$$\frac{E_B}{k_B T} \gg 1, \quad (4.19)$$

which provides the necessary condition for the separation of time scales, namely  $f^{-1} \gg f_0^{-1}$  [93]. In a magnetic system the intrinsic dynamics that determine  $f_0$  are described by the Landau-Lifshitz-Gilbert Equation for the precessional motion of a magnetic moment  $\mathbf{M}$  in an effective external field  $\mathbf{H}_{\text{eff}}$  [94]

$$\frac{d\mathbf{M}}{dt} = -\frac{\gamma}{(1 + \alpha^2)} [\mathbf{M} \times \mathbf{H}_{\text{eff}}] - \frac{\gamma}{(1 + \alpha^2)} \frac{\alpha}{M_S} [\mathbf{M} \times [\mathbf{M} \times \mathbf{H}_{\text{eff}}]]. \quad (4.20)$$

Here,  $\gamma = \gamma_e \mu_0 = 2.21 \times 10^5 \text{m}/(\text{As})$  is the gyromagnetic ratio,  $\alpha$  is the Gilbert damping parameter and  $M_S$  is the saturation magnetization. The stochastic fluctuations enter Eq. 4.20 by including a thermal field  $\xi(\mathbf{r}, t)$  within  $\mathbf{H}_{\text{eff}}$  that follows the fluctuation dissipation relation

$$\langle \xi_i(\mathbf{r}, t) \xi_j(\mathbf{r}', t') \rangle = 2D \delta_{ij} \delta(\mathbf{r} - \mathbf{r}') \delta(t - t'), \quad \text{where} \quad D = \frac{\alpha k_B T}{\gamma \mu_0^2 M_S V}. \quad (4.21)$$

Here,  $V$  denotes the particle volume. From this ansatz, Brown [95] derived an expression for the attempt frequency in the case of uniaxial anisotropy and the field applied parallel to the easy axis of the particle:

$$f_0 = \frac{\alpha \gamma}{1 + \alpha^2} \sqrt{\frac{H_K^3 \mu_0 M_S V}{2\pi k_B T}} \left(1 - \frac{H}{H_K}\right) \left(1 - \frac{H^2}{H_K^2}\right). \quad (4.22)$$

Thermally activated reversal over an energy barrier was first introduced to magnetism by L. Néel [96]. Hence, the theoretical model described in the following is often referred to as the Arrhenius-Néel model. The energy barrier for the magnetization of a single domain particle with uniaxial anisotropy (see also Sec. 4.1) is the difference between the maximum and the metastable minimum of the free energy density  $e$  (also see Eq. 4.8) which can be computed by setting the first derivative of the free energy density to zero:

$$E = K \sin^2 \theta - H \mu_0 M_S \cos \theta \quad (4.23)$$

$$\begin{aligned} \frac{dE}{d\theta} &= 2K \sin \theta \cos \theta + H \mu_0 M_S \sin \theta = 0 \\ \Rightarrow \theta_1 &= 0, \quad \theta_2 = \pi, \quad \theta_3 = \arccos \left( -\frac{H \mu_0 M_S}{2K} \right) \end{aligned} \quad (4.24)$$

By evaluating the second derivative of Eq. 4.23 the minima and maxima of the free energy functional are found:

$$\begin{aligned} \frac{d^2 E}{d\theta^2} &= -2K \sin^2 \theta + 2K \cos^2 \theta + H \mu_0 M_S \cos \theta \\ \left. \frac{d^2 E}{d\theta^2} \right|_{\theta_1} &= 2K + H \mu_0 M_S > 0 \\ \left. \frac{d^2 E}{d\theta^2} \right|_{\theta_2} &= 2K - H \mu_0 M_S > 0 \quad \text{for } H < \frac{2K}{\mu_0 M_S} \\ \left. \frac{d^2 E}{d\theta^2} \right|_{\theta_3} &= -2K + \frac{H^2 (\mu_0 M_S)^2}{2K} < 0 \quad \text{for } H < \frac{2K}{\mu_0 M_S} \end{aligned} \quad (4.25)$$

If the field  $H$  is applied along the easy axis at  $\theta = 0$   $E(\theta_1 = 0)$  is a global minimum, which corresponds to the state where the magnetization of the particle is aligned parallel to the external field. For the energy barrier of the switching process the relevant minimum is  $E(\theta_2 = \pi) \equiv E_{\min}$ , because in order to switch the magnetization of the particle the field is applied in the opposite direction. During the switching process the maximum  $E_{\max} = E(\theta_3)$  has to be crossed, which yields an energy density barrier

$$\begin{aligned} \Delta E = E_{\max} - E_{\min} &= K + \frac{H^2 (\mu_0 M_S)^2}{4K} - H \mu_0 M_S = \frac{1}{4K} (2K - H \mu_0 M_S)^2 \\ &= K \left( 1 - \frac{H}{H_K} \right)^2, \end{aligned} \quad (4.26)$$

where

$$H_K = \frac{2K}{\mu_0 M_S} \quad (4.27)$$

is the switching field at zero temperature, i.e. the anisotropy field for the Stoner-Wohlfarth particle in this case [88]. This means that at zero temperature  $H_K$  is the threshold value for which the energy barrier vanishes. At finite temperature,

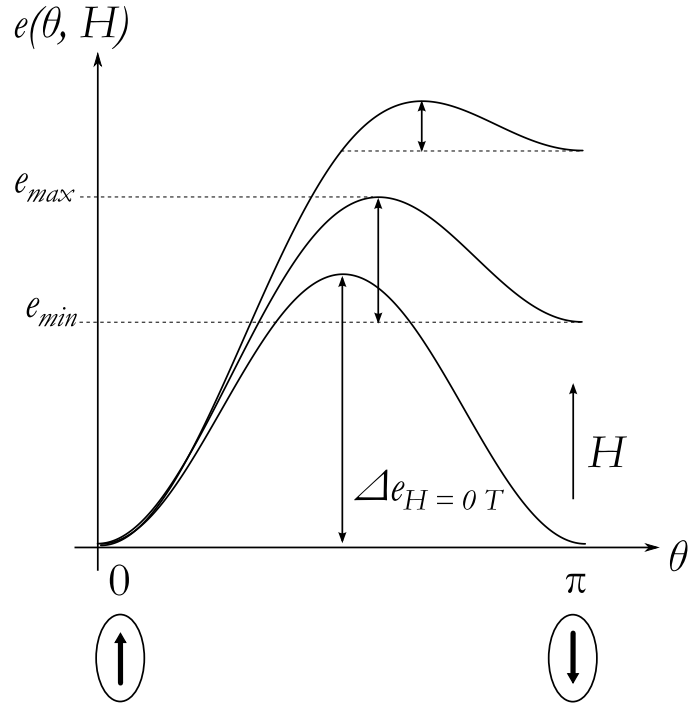


Fig. 4.4. – Energy barriers for a single domain particle with uniaxial anisotropy and the external field applied parallel to the easy axis.

however, the reversal is aided by thermal fluctuations and it is possible for the magnetization to switch at fields lower than  $H_K$ . This means that when the system is left to itself there is a certain likelihood for the magnetization to spontaneously overcome the energy barrier. The waiting time for this to occur is given by the rate equation Eq. 4.18. Plugging  $E_B = \Delta EV$  from Eq. 4.26 into Eq. 4.18 yields an expression for the temperature dependent switching field  $H_C$

$$H_C(t) = H_K \left[ 1 - \sqrt{\frac{k_B T}{KV} \ln(f_0 t)} \right], \quad (4.28)$$

where  $t = f^{-1}$  is the waiting time. Eq. 4.28 is known as Sharrock's Equation and was first derived to fit coercivities obtained from experiments for longitudinal magnetic recording media [97]. Eq. 4.28 can also be written with a generalized exponent  $1/n$  [98]:

$$H_C(t) = H_K \left\{ 1 - \left[ \frac{k_B T}{KV} \ln(f_0 t) \right]^{1/n} \right\}, \quad (4.29)$$

where depending on the model used to derive the energy barrier  $\Delta e$  the exponent varies from  $n = 1$  for reversal by weakly pinned domain walls [99] to up to  $n = 3/2$  [100, 101], where more general orientations of the external field with respect to the particles easy axis are considered as for special case of parallel alignment which is given by  $n = 2$  (see Eq. 4.26).



## 4.2.1 Field-rate dependent coercivity

Eqs. 4.28 and 4.29 provide expressions for time-scale dependent switching field in stepped field experiments, in which the field required to switch the magnetization acts over a certain time  $t$  with constant strength. The more relevant case within in the framework of the performance of the TMR fluxgate sensor is for a field, that is ramped up at a rate  $R$  so that  $H(t) = Rt$ . In the following, expressions for field-rate dependent coercivity from the literature will be given. Chantrell et al. [102] start with the phenomenological observation that the magnetization decays as

$$M(t) = M_S \exp\left(-\frac{t}{\tau}\right) \quad (4.30)$$

where  $\tau^{-1} = f_0 \exp(-\Delta E/k_B T)$  (see also Eq. 4.18). Their solution is to sum up Eq. 4.30 over small field steps  $\Delta H$ . With the justification that the largest part of the sum will be at fields close to the switching field  $H_C$  they linearize the expression from Eq. 4.26 for  $\Delta E$  and arrive at an implicit formula for the rate-dependent switching field  $H_C$ , which is useful to rewrite as a field rate with  $H_C$  as the free parameter:

$$R(H_C) = H_K f_0 \frac{\exp\left[-\beta \left(1 - \frac{H_C}{H_K}\right)^2\right]}{2\beta \left(1 - \frac{H_C}{H_K}\right)} \quad (4.31)$$

Here  $\beta = KV/(k_B T)$  is the thermal stability ratio and  $H_K = 2K/\mu_0 M_S$  is the anisotropy field. Feng and Visscher [103] also derive an implicit expression starting from a master equation for the probability to find a particle still unswitched

$$\frac{dP_{\text{not}}}{dt} = -f P_{\text{not}}. \quad (4.32)$$

Here,  $f$  is again the Arrhenius transition rate from Eq. 4.18. The master equation will be discussed in more detail in Sec. 4.3. Sorting variables and plugging in Eq. 4.18 yields

$$\ln P(t) = f_0 \int_{-\infty}^t \exp\left[-\beta \left(1 - \frac{H(t')}{H_K}\right)^n\right], \quad (4.33)$$

where an energy barrier  $\Delta E = KV(1 - H/H_K)^n$  with a generalized exponent  $n$  is used. The solution of this integral can be expressed in terms of  $y \equiv \beta^{1/n}(1 - H(t')/H_K)$  by a generalized error function defined by

$$\text{erfg}_n(y) \equiv \frac{2}{\sqrt{\pi}} \int_y^{\infty} e^{-y'^n} dy'. \quad (4.34)$$

For  $n = 2$   $\text{erfg}_2(y) = 1 - \text{erf}(y)$  applies with the (conventional) error function defined as

$$\text{erf}(x) = \frac{2}{\sqrt{\pi}} \int_0^x e^{-y^2} dy. \quad (4.35)$$

Then, the relation between the field sweep rate and the switching field reads

$$R(H_C) = \frac{\pi f_0 H_K}{2 \ln 2 \beta} \left\{ 1 - \operatorname{erf} \left[ \sqrt{\beta} \left( 1 - \frac{H_C}{H_K} \right) \right] \right\} \quad (4.36)$$

Peng and Richter [104] also derive rate-dependent coercivity for arbitrary exponents  $n$ , but avoid the use of the error function and instead solve a similar integral to Eq. 4.33 by using the expansion of the Gamma function for small arguments. This yields

$$H_C(t) = H_K \left\{ 1 - \left[ \frac{1}{\beta} \ln \left[ \frac{C}{(\ln C)^{1-1/n}} \right]^{1/n} \right] \right\} \quad (4.37)$$

where

$$C = \frac{f_0}{n \ln 2} \frac{H_K}{R} \beta^{-1/n} \gg 1. \quad (4.38)$$

In Table 4.1 the expression for rate-dependent coercivity is given for  $n = 2$ . Using for the field rate  $R = 2H_{\max}/\Delta t$  [104] Eq. 4.38 can be rewritten to derive a condition for the validity of Eq. 4.37 under the assumption that  $n \leq 2$ :

$$\begin{aligned} C &\approx \frac{f_0 H_K}{\sqrt{\beta} R} \gg 1 \Rightarrow f_0 H_K \gg \sqrt{\beta} R \\ R &= \frac{2H_{\max}}{\Delta t} \Rightarrow f_0 \Delta t \gg \frac{200H_{\max}}{H_K} \\ H_{\max} &\approx 2H_K \Rightarrow \Delta t \gg \frac{f_0}{400} \end{aligned} \quad (4.39)$$

Here, the fact was used that the growth of the right hand side of  $f_0 H_K \gg \sqrt{\beta} R$  is dominated by the increase in  $R$  for large values of  $R$  and  $\beta$ . The factor 100 stems from setting  $\beta = 10^4$  which is thermally very stable. If the common value for the attempt frequency  $f_0 = 10^9$  Hz is used in Eq. 4.39 we end up with the requirement for Eq. 4.37 to hold for  $\Delta t \gg 2.5 \times 10^{-6}$  s. This sets a lower limit for the time scale at which experimental coercivity data can be successfully interpreted by the Arrhenius-Néel model. On the other hand, this also limits the possibility of the model to predict the switching fields present at very high field rates, that can occur for example in magnetic recording applications. Although Feng and Visscher [103] succeed in fitting their Eq. 4.36 to data from a simulation based on the Landau-Lifshitz equation, it is not clear to which degree this is physically correct. In Sec. 4.2.2 a similar criterion will be derived based on a thermal switching field distribution.

All models described before neglect the fact, that the attempt frequency  $f_0$  is actually not a constant, but is strongly dependent on the material parameters as well as on the external applied magnetic field (see Eq. 4.22). Expressions for arbitrary orientations of the field to the easy axis can be found in Refs. [105] and [106].

$$R(H_C) = H_K f_0 \frac{\exp[-\beta(1-H_C/H_K)^2]}{2\beta(1-H_C/H_K)} \quad [102]$$

$$R(H_C) = \frac{\pi f_0 H_K}{2 \ln 2\beta} \left\{ 1 - \operatorname{erf} \left[ \sqrt{\beta} \left( 1 - \frac{H_C}{H_K} \right) \right] \right\} \quad [103]$$

$$H_C(R) = H_K \left[ 1 - \sqrt{\frac{1}{\beta} \ln \left( \frac{f_0 H_K}{2 \ln 2R \sqrt{\beta \ln [f_0 H_K / (2 \ln 2 \sqrt{\beta} R)]}} \right)} \right] \quad [104]$$

$$H_C(R) = H_K \left[ 1 - \sqrt{\frac{1}{\beta} \ln \left( \frac{f_0 H_K}{2R\beta} \right)} \right] \quad [107]$$

Tab. 4.1. – Overview of the analytical expressions for rate-dependent coercivity and the corresponding references

For the uniaxial anisotropy case El-Hilo et al. [107] have provided a model to fit experimental data by taking

$$f \approx \bar{f}_0 \left( 1 - \frac{H}{H_K} \right) \exp \left[ \frac{kV}{k_B T} \left( 1 - \frac{H}{H_K} \right)^2 \right],$$

where  $\bar{f}_0 = \gamma \sqrt{H_K^3 \mu_0 M_S V / (2\pi k_B T)}$ . Here, the linear dependence of the attempt frequency on the external field is being considered. This leads to an explicit expression for field dependent coercivity reading

$$H_C(R) = H_K \left[ 1 - \sqrt{\frac{1}{\beta} \ln \left( \frac{f_0 H_K}{2R\beta} \right)} \right]. \quad (4.40)$$

All discussed expressions for field-rate dependent coercivities from the literature are given in Tab. 4.1 for the quadratic field dependence of the energy barrier from Eq. 4.26. For low field rates these expressions do not significantly differ from each other. However, as it will be shown in the following sections for higher field rates these models strongly differ from each other due to the approximations assumed in their derivation.

## 4.2.2 Derivation of a thermal switching field distribution

In view of the original aim to determine the uncertainty of the switching from the high to the low resistance state of an MTJ, which will limit the performance of a TMR fluxgate magnetometer, the distribution of switching fields that is observed over a certain number of switching cycles will be a crucial parameter. The switching field distribution has its origin in the fact that the thermal fluctuations act in a way that after switching has happened at a certain field  $H_{C_1}$  the next switching event might take place at a slightly different field  $H_{C_2}$ . The two switching events are considered to be uncorrelated or memoryless, which also means that they must be separated by a time step that allows the system to settle to thermodynamic equilibrium. The

switching field  $H_C$  can be considered a stochastic variable which can take values  $H_{C_1}, H_{C_2}, \dots, H_{C_n}$ . To each of these values a probability  $p_i \geq 0$  can be assigned for which  $\sum_{i=1}^n p_i = 1$  ( $n$  can be a finite integer or  $n = \infty$ ). The probability density function (PDF) is then defined as

$$D(H_C) = \sum_{i=1}^n p_i \delta(H_C - H_{C_i}) \quad (4.41)$$

for the case that  $H_C$  can only take discrete values. For the continuous case this corresponds to the expectation that the switching field falls into an interval  $\{H_{C_1} \leq H_C \leq H_{C_2}\}$  and there exists a function  $D(H_C)$  for which

$$\text{Prob}(H_{C_1} \leq H_C \leq H_{C_2}) = \int_{H_{C_1}}^{H_{C_2}} D(H_C) dH_C. \quad (4.42)$$

The accumulated probability up to the switching field  $H_C$  is called the (cumulative) distribution function (CDF) and is given by integrating Eq. 4.42

$$P(H_C) = \int_{-\infty}^{H_C} D(H) dH. \quad (4.43)$$

In the following we will use the notation  $D(H_C) \equiv dP/dH_C$  for the switching field distribution (SFD) [12].

This is the same ansatz as used by Feng and Visscher [103], in which backswitching of particles is neglected because high energy barriers are assumed. Also, Kurkijärvi used this approach to compute an intrinsic distribution for the magnetic flux in a superconducting ring which is closed by a Josephson junction [108]. Solving the master equation leads to the integral known from Sec. 4.2.1

$$\ln P_{\text{not}} = - \int_{-\infty}^{t_0} f_0 \exp \left[ -\beta \left( 1 - \frac{H(t)}{H_K} \right)^2 \right] dt \quad (4.44)$$

The integral on the right hand side can be solved analytically by using the substitution

$$u = \sqrt{\beta} \left( 1 - \frac{H(t)}{H_K} \right), \quad H(t) = Rt,$$

where  $R$  is the field rate in A/(ms) for a linearly swept field. This yields  $dt = -H_K/(R\sqrt{\beta})du$  and by properly substituting the limits and using the fact that  $\exp(-x^2)$  is an uneven function in  $x$  leads to rewriting Eq. 4.44 as

$$\ln P_{\text{not}} = - \frac{f_0 H_K}{\sqrt{\beta} R} \int_{u_0}^{\infty} e^{-u^2} du, \quad (4.45)$$

which can be solved by noticing the definition of the complementary error function

$$\text{erfc}(x) = \frac{2}{\sqrt{\pi}} \int_x^{\infty} e^{-y^2} dy = 1 - \text{erf}(x). \quad (4.46)$$

Then, the switching probability for thermal activation over the quadratic energy barrier from the Stoner-Wohlfarth model (see Eq. 4.26) is

$$P(u_0) = 1 - P_{\text{not}}(u_0) = 1 - \exp \left\{ -\frac{f_0 H_K}{2R} \sqrt{\frac{\pi}{\beta}} [1 - \text{erf}(u_0)] \right\} \quad (4.47)$$

with

$$u_0 = \sqrt{\beta} \left( 1 - \frac{H_C}{H_K} \right).$$

$H_C = H_C(R)$  is the rate-dependent switching field where  $P = 0.5$  as it has also been defined for the other models presented in Sec. 4.2.1. Eq. 4.47 is not explicitly solvable with respect to  $H_C$ , however, it gives the cumulative distribution function (CDF) for the switching field distribution  $dP/dH_C$ , which is itself a probability density function (PDF). Differentiating Eq. 4.47 with respect to  $H_C$  gives

$$\frac{dP}{dH_C} = \frac{dP}{du_0} \frac{du_0}{dH_C} = \frac{f_0}{R} \exp \left\{ -\frac{f_0 H_K}{2R} \sqrt{\frac{\pi}{\beta}} [1 - \text{erf}(u_0)] \right\} \exp(-u_0^2) \quad (4.48)$$

In Fig. 4.5 the switching field distributions and the corresponding switching probabilities are plotted for varying thermal stability ratios  $\beta$ . The other parameters were chosen in a way to model the TMR fluxgate sensor properties. Eq. 4.48 represents an analytical solution for a more general case of a magnetic susceptibility of thermally activated single domain particle with the external field applied at an arbitrary angle, where only numerical evaluation is possible [109].

The thermal SFD presented in this section is a fundamental effect, which also occurs in granular magnetic recording media which consist of single grains with a distribution of volumes and coercivities. However, it can be shown that the SFD of the medium can be separated into an intrinsic component  $\sigma_S^{\text{in}}$  originating from grain size distributions and other material properties and a contribution originating solely from thermal fluctuations  $\sigma_S^t$ , which add up as

$$\sigma_S^2 = (\sigma_S^{\text{in}})^2 + (\sigma_S^t)^2. \quad (4.49)$$

The additional contribution  $\sigma_S^t$  becomes especially important when simulating SFDs at high field rates, that occur in the magnetic recording process [87, 110].

### 4.2.3 Properties of the switching field distribution

In order to compare the models for field-rate dependent coercivity presented in Sec. 4.2.1 to the switching field distribution derived in Sec. 4.2.2, the mean value of the SFD or  $dP/dH_C$  (Eq. 4.48) has to be computed. This will give a mean switching field  $\langle H_C \rangle$  which should show a similar rate dependence as the expressions from

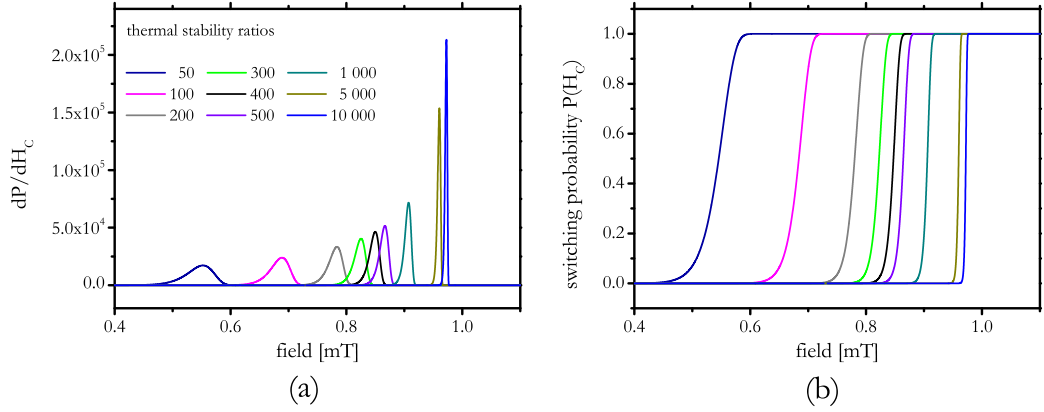


Fig. 4.5. – (a) switching field distribution (Eq. 4.48) and (b) switching probability (Eq. 4.47) for varying thermal stability ratios  $\beta$  ( $f_0 = \text{const.} = 10^9$  Hz,  $\mu_0 H_K = 1$  mT,  $R = 1$  T/s)

Tab. 4.1. The mean value of  $dP/dH_C$  is given the same way as the first moment of any probability density function [12]

$$\langle H_C \rangle = \int_{-\infty}^{+\infty} H_C \frac{dP}{dH_C} dH_C. \quad (4.50)$$

In Fig. 4.6 the mean values of the switching field distribution for varying field rates are plotted together with the expressions from the literature by Chantrell et al. [102], El-Hilo et al. [107], Feng and Visscher [103] and Peng and Richter [104]. The values for the rate-dependent switching field produced by our model, the “mean of SFD” model, are comparable to the values from the other models. It should be noted, that all models in Fig. 4.6 except El-Hilo’s model assume that the attempt frequency  $f_0$  is constant with respect to the magnitude of the external field  $H$ . However, as already shown by Brown [95]  $f_0$  is strongly dependent on parameters such as field, temperature and material constants (see Eq. 4.22). In Sec. 4.2.4 below we will show how the “mean of SFD” model can be extended to include the field dependence of the attempt frequency. However, for the estimation of the detection limit of the TMR fluxgate sensor, the exact magnitude of the mean value of the SFD will be of minor importance as compared to the magnitude of the standard deviation. The standard deviation of a stochastic variable - which is the switching field  $H_C$  here - is defined as

$$\sigma_{H_C} = \sqrt{\langle H_C^2 \rangle - \langle H_C \rangle^2}, \quad (4.51)$$

where

$$\langle H_C^2 \rangle = \int_{-\infty}^{+\infty} H_C^2 \frac{dP}{dH_C} dH_C \quad (4.52)$$

is the second moment of the switching field distribution  $dP/dH_C$  (Eq. 4.48). In Fig. 4.7a computed values of the standard deviation are given for SFDs at different field rates. The input parameters to the SFD are  $f_0 = \text{const.} = 10^9$  Hz for the attempt

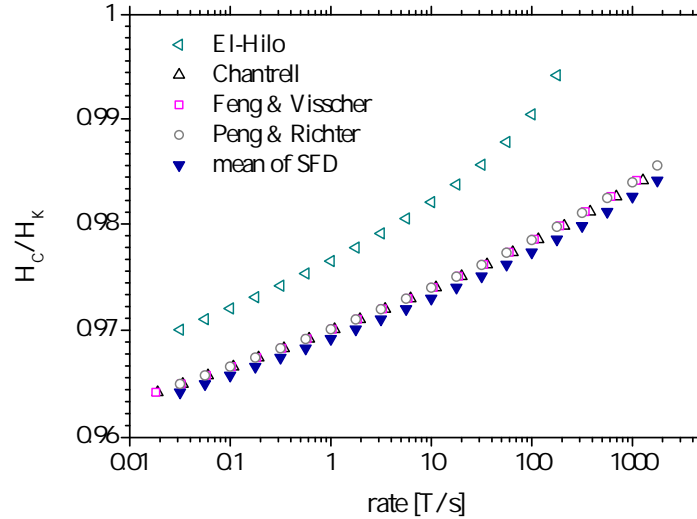


Fig. 4.6. – Comparison of the analytical models from Table 4.1 with the mean value of the switching field distribution. The datapoints for the Chantrell- and the Feng & Visscher-models were generated by taking the “mean-of-SFD” values for  $H_C$  as input data and then plotting the rate with  $H_C$  as the free parameter with the x- and y-axes interchanged. This is due to the fact, that Eqs. 4.31 and 4.36 give relations  $R(H_C)$  instead of  $H_C(R)$ . The “mean-of-SFD” model yields switching fields of approximately the same magnitude as for the other models for a constant attempt frequency of  $f_0 = 10^9$  Hz (except El-Hilo’s model, which includes the field dependence of  $f_0$ ). Input parameters:  $\beta = 10\,000$ ,  $H_K = 5$  mT.

frequency,  $H_K = 5$  mT for the zero temperature anisotropy field, and  $\beta = 10^4$  for the thermal stability ratio. These parameters give a reasonable approximation for the properties of the TMR fluxgate sensors that are the subject of this thesis. We are aware of the fact that switching of a lithographically patterned ellipse with dimensions in the order of several  $\mu\text{m}$  involves other mechanisms than coherent rotation of the magnetization with an energy barrier  $\Delta E \propto (1 - H/H_K)^2$ . However, as already mentioned at the beginning of this section other exponents can be used to model more general reversal modes. In fact, for complex structures the energy landscape would have to be modeled using micromagnetic methods in order to find the minima and the corresponding energy barriers [111, 112] which is beyond the scope of this work. The approach presented here has the advantage of providing an analytical solution for the switching probability and hence the switching field distribution.

In Fig. 4.7 b the distributions are shown at different field rates. The distributions become wider for higher field rates with the peak of distribution moving towards higher switching fields. However, as shown in Fig. 4.8 a and also above in Fig. 4.6 the mean value, which is defined by the distribution’s first moment in Eq. 4.50, does not increase further towards  $H_K$  after reaching a maximum value. In Fig. 4.8 b this is visualized in an alternative way by plotting the values of the standard deviation as percentage values of the mean normalized switching field  $H_C/H_K$ . We see, that

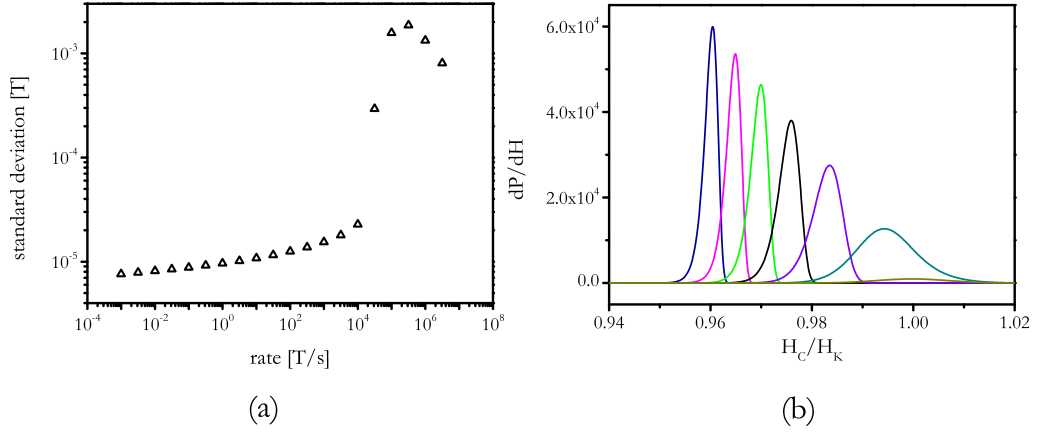


Fig. 4.7. – (a) standard deviation as a function of the field rate and (b) corresponding switching field distributions (SFDs) from which the mean (first moment) and the second moment are computed ( $f_0 = \text{const.} = 10^9$  Hz,  $\mu_0 H_K = 5$  mT,  $\beta = 10^4$ . Only every second SFD is plotted for better visibility.)

the error bars blow up within a very narrow range of field rates. This is a surprising behavior which has not yet been described before. The models for rate-dependent coercivity presented in Sec. 4.2.1 use approximations in their derivation and hence make an extrapolation from the Arrhenius-Néel model valid at low rates as present in VSM measurements up to such high rates as used in magnetic recording, where the approach based on transition state theory cannot be expected to model the underlying physical behavior appropriately anymore. In the regime of high field rates there is no more clear separation of the time scale of the intrinsic dynamics of the system and the time scale over which the system is allowed to settle to a state of local equilibrium. To investigate this crossover behavior further the Riemann sum integral value of the SFD is also plotted in Fig. 4.8 a. From the definition of the mean value of the SFD it is clear that the integral has to decrease simultaneously to  $\langle H_C \rangle$ . However, any probability density function  $D$  of a continuous variable  $x$  has to fulfill the conditions [12]

$$D(x) \geq 0, \quad \text{and} \quad \int_{-\infty}^{+\infty} D(x) dx = 1. \quad (4.53)$$

If this is not fulfilled the probability distribution cannot be expected to model the true physical behavior of the system. These conditions can also be written as a requirement to the CDF, which allow for a definition of criterion when the transition state theory based model fails to describe the behavior of the system. The CDF (Eq. 4.47)

$$P(u_0) = 1 - P_{\text{not}}(u_0) = 1 - \exp \left[ -\frac{f_0 H_K}{2R} \sqrt{\frac{\pi}{\beta}} \text{erfc}(u_0) \right]$$



has to fulfill

$$\lim_{u_0 \rightarrow \pm\infty} P(u_0) = \begin{cases} 0, & u_0 \rightarrow +\infty \\ 1, & u_0 \rightarrow -\infty. \end{cases} \quad (4.54)$$

For  $u_0 \rightarrow +\infty$  we have for the complementary error function  $\text{erfc}(+\infty) \rightarrow 0$  and hence  $P(u_0 \rightarrow +\infty) = 0$  is fulfilled for all values of the model parameters  $f_0, H_K, R$  and  $\beta$ . For the limit  $u_0 \rightarrow -\infty$  we have  $\text{erfc}(-\infty) \rightarrow 1$  and thus the requirement

$$1 - \exp\left[-\frac{f_0 H_K}{2R} \sqrt{\frac{\pi}{\beta}}\right] = 1$$

or

$$\exp\left[-\frac{f_0 H_K}{2R} \sqrt{\frac{\pi}{\beta}}\right] = 0,$$

which is fulfilled for

$$-\frac{f_0 H_K}{2R} \sqrt{\frac{\pi}{\beta}} \rightarrow +\infty.$$

This leads to the criterion for the model parameters, which they have to fulfill in order for the data of interest to qualify for a physical description based on thermally activated reversal over large energy barriers according to transition state theory

$$R\sqrt{\beta} \ll f_0 H_K. \quad (4.55)$$

Eq. 4.55 is the same relation as already given by Peng and Richter [104] (see Eq. 4.39). However, they did not set this into context with the physical range of validity for their model. Furthermore, our approach with the derivation of the SFD makes it possible to also derive this criterion for a field-dependent attempt frequency  $f_0$  (see Sec. 4.2.4).

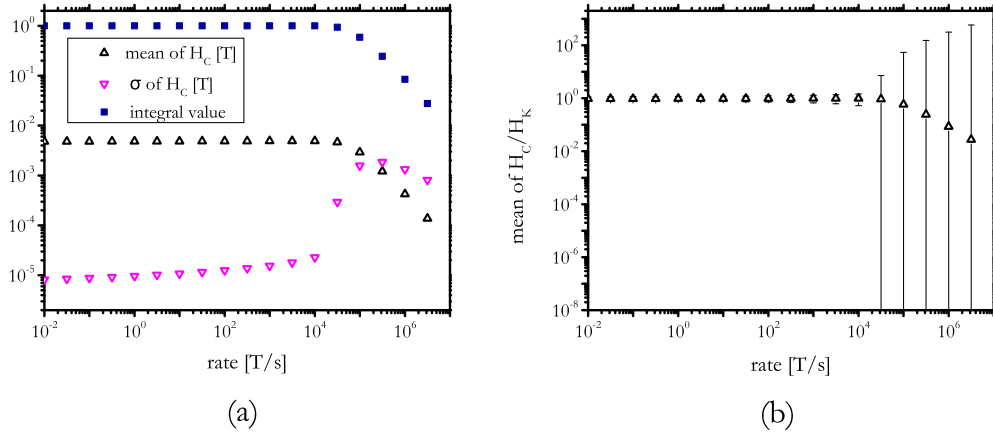


Fig. 4.8. – (a) mean value  $\langle H_C \rangle$ , standard deviation  $\sigma_{H_C}$  and the integral value of the SFD as a function of the field rate. If the SFD is a probability distribution function the area under the SFD - i.e. its integral value from  $-\infty$  to  $+\infty$  must be 1. (b)  $\langle H_C \rangle$  with respect to the zero temperature anisotropy field  $H_K$  and  $\sigma_{H_C}$  plotted as error bars with respect to  $\langle H_C \rangle$  ( $f_0 = \text{const.} = 10^9$  Hz,  $\mu_0 H_K = 5$  mT,  $\beta = 10^4$ )

#### 4.2.4 Consideration of the field dependence in the attempt frequency

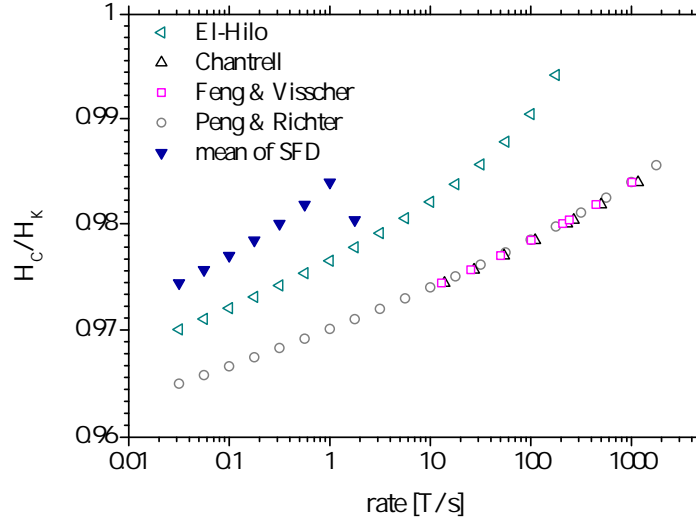


Fig. 4.9. – Comparison of the analytical models from Table 4.1 with the mean value of the switching field distribution, where the field dependence of the attempt frequency  $f_0$  is taken into account. There is a significant shift towards higher switching fields as compared to the SFD with  $f_0 = \text{const.}$  (see Fig. 4.6).

As already mentioned in Sec. 4.2.1 it is often ignored that the prefactor  $f_0$  called attempt frequency in the Arrhenius-Néel Law (Eq. 4.18) is not constant, but depends on several material parameters as well as the applied magnetic field  $H$  (see Eq. 4.22). For small fields  $H \ll H_C$  this is a valid approximation, however, when switching is studied obviously fields close to the coercive field  $H \approx H_C$  are applied. In the following we will derive the switching field distribution with a field dependent attempt frequency  $f_0 = f_0(H)$ . The discussion is restricted here to the axially symmetric case, i.e. the external field is applied parallel to the easy axis, which gives the quadratic field dependence for the energy barrier  $\Delta E = KV(1 - H/H_K)^2$ . Using the same substitution as in Sec. 4.2.2  $u = \sqrt{\beta}(1 - H/H_K)$  and Brown's formula for the attempt frequency from Eq. 4.22 the integral in Eq. 4.45 with  $f_0(H(u)) = f_0(u)$

$$\ln P_{\text{not}} = -\frac{H_K}{R\sqrt{\beta}} \int_{u_0}^{\infty} f_0(u) e^{-u^2} du \quad (4.56)$$

needs to be solved. The details of the substitution and the evaluation of Eq. 4.56 are given in the appendix A.2. The result for the SFD with field-dependent attempt frequency  $f_0$  is

$$\frac{dP}{dH_C} = P_{\text{not}} \frac{\alpha\gamma}{1 + \alpha^2} \frac{H_K}{R\sqrt{\pi\beta}} \left( 2u_0^2 - \frac{u_0^3}{\sqrt{\beta}} \right) e^{-u_0^2}, \quad (4.57)$$

where  $\alpha$  is the Gilbert damping parameter and  $\gamma$  the gyromagnetic ratio and

$$P_{\text{not}} = \exp \left\{ \frac{C'}{2\beta} e^{-u_0^2} (1 - 2\sqrt{\beta}u_0 + u_0^2) - \frac{C'\sqrt{\pi}}{2} \text{erfc}(u_0) \right\}$$

with  $C' = \frac{\alpha\gamma}{1 + \alpha^2} \frac{H_K^2}{\sqrt{\pi}\beta R}$ .

$\alpha$  and  $\gamma$  also occur in the microscopic equation of motion for the magnetic moment, which is the LLG equation (Eq. 4.20). Hence, Eq. 4.57 provides us with an understanding of the SFD based on microscopic material parameters that reflect the internal dynamics of the system, which goes beyond a “coarse grained” model based on a constant attempt frequency. Applying the same analysis with respect to the properties of a PDF or CDF (Eqs. 4.53 and 4.54) to the field-dependent SFD from Eq. 4.57 leads to a validity criterion reading

$$R\beta \ll \frac{1}{2} \frac{\alpha\gamma}{1 + \alpha^2} H_K^2. \quad (4.58)$$

This boundary of validity is also reflected in the kink of the mean switching field  $\langle H_C \rangle$  with respect to the rate which is visible in Fig. 4.9. As already explained in Sec. 4.2.3 the decrease of  $\langle H_C \rangle$  after the kink is due to the violation of the normalization condition for the SFD (Eq. 4.53), which means that the integral over the SFD becomes less than one. In Fig. 4.10 a we present the data for the field dependent SFD analogously to Fig. 4.8 a, which shows that the violation of the normalization condition is already reached at a rate of  $\mu_0 R \approx 1$  T/s, whereas for  $f_0 = \text{const.}$  the integral only starts to decrease at a rate of  $\mu_0 R \approx 10^4$  T/s. Eq. 4.57 requires the input of the Gilbert damping constant  $\alpha$  as an additional material dependent parameter as compared to Eq. 4.48. We set  $\alpha = 0.02$ , which corresponds to a relatively low damping value commonly found in soft magnetic materials such as CoFeB and Permalloy. According to Eq. 4.57 changing  $\alpha$  is a scaling factor to  $\langle H_C \rangle$ . Depending on the exact value of  $\alpha$  the “mean of SFD” values in Fig. 4.9 might also be lower than those given by El-Hilo’s model, which uses an approximation of the Brown formula (Eq. 4.22). However, the mean switching fields  $\langle H_C \rangle$  given by computing the first moment of the SFD for field dependent attempt frequency will be always be higher than those given by the other models, which do not consider any field dependence.

In Fig. 4.10 b the SFDs are plotted for different field rates, where the dashed lines denote SFDs for  $f_0 = \text{const.}$  (Eq. 4.48) and the solid lines the SFDs according to Eq. 4.57. This shows that at the same field rate the peaks of the SFDs for field dependent attempt frequency are shifted towards higher fields. A similar result was achieved by Klik et al. [113], but without an explicit analytical result.

An interesting feature is also the second peak emerging at fields above  $H_K$ . It is not clear whether this is of physical relevance or just a mathematical feature. In fact, the distribution is not normalized anymore at this field rate, but in principle

it is physically feasible that for “high” rates the particle might switch at fields  $H_C > H_K$  [114].

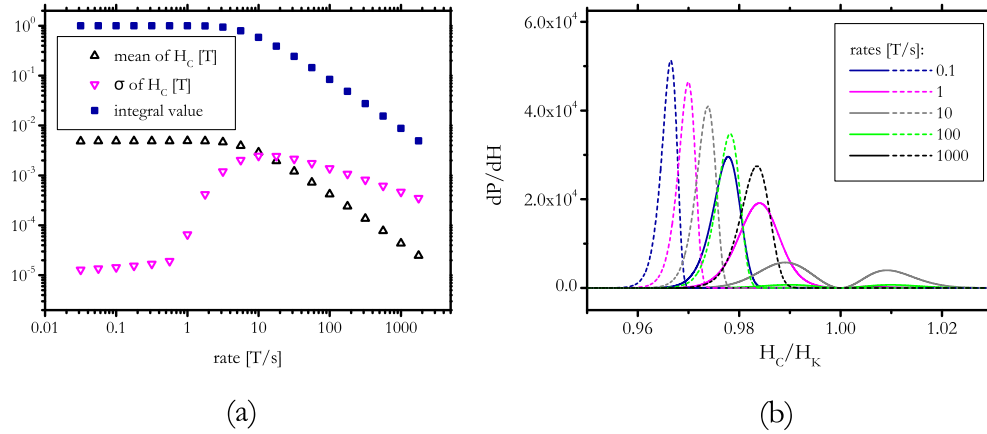


Fig. 4.10. – (a) mean value  $\langle H_C \rangle$ , standard deviation  $\sigma_{H_C}$  and the integral value of the SFD for field dependent attempt frequency as a function of the field rate. (b) SFDs for  $f_0 = \text{const.} = 10^9$  Hz (dashed lines) and SFDs according to Eq. 4.57 Hz with  $\alpha = 0.02$  (solid lines) ( $\mu_0 H_K = 5$  mT,  $\beta = 10^4$ ). The peaks of the SFDs for field dependent  $f_0$  are shifted towards higher fields.

### 4.3 Monte Carlo Simulation

A Monte Carlo simulation is used to simulate a single domain fluxgate magnetometer signal under the influence of thermal fluctuations. Monte Carlo methods in general are a set of methods that make use of random numbers in their way of problem solving. In the field of statistical physics, Monte Carlo methods were originally developed as a means to solve the Fokker-Planck equations describing the time-dependent decay of configurational probability distributions of large ensembles of identical particles. These integrodifferential equations can hardly be solved using a classical analytical approach because the microscopic degrees of freedom may strongly couple to each other. To solve the problem using the statistical approach of the Monte Carlo method, it is assumed that the probability flow described by the Fokker-Planck equation comprises deterministic and stochastic processes. The method starts at a state with a certain probability  $P_1$  and then assumes random processes acting on the given independent degrees of freedom of a set of identical particles. After a certain time  $\Delta t$  there exist a certain new probability  $P_2$  for the system to be in another state. This process is repeated several times until the probability distributions do not change significantly anymore [115]. During each of the steps the underlying physical processes must obey the detailed balance condition

$$P_1 r_{12} = P_2 r_{21}, \quad (4.59)$$

where  $P_1, P_2$  are the stationary probabilities that the system is either in state 1 or state 2 and  $r_{12}, r_{21}$  are the transition rates from  $1 \rightarrow 2$  and  $2 \rightarrow 1$ , respectively. Eq. 4.59 is a balance equation for the probability flux between any two possible states of a system and gives a condition for thermal equilibrium. A chain of processes involving transitions through several states, where the probability for the next state only depends on the current state is called a Markov chain. Such systems lack memory of their history and are called Markovian [90]. There exist a vast amount of literature on the topic and its possible application to problems also outside of statistical physics [116, 117].

### 4.3.1 Thermodynamic background

A system consisting of  $N$  particles has a certain finite thermodynamic probability to be in a particular state. This state includes all possible microscopic degrees of freedom and corresponds to a point in  $N$ -dimensional phase space. The phase space may include real or reciprocal spatial coordinates, momenta or magnetization configurations, i.e. any set of canonical variables, which occur in the  $N$ -particle Hamiltonian of the system. Within the framework of a Monte Carlo simulation it is described how the probability distribution of a system evolves from one state to another under the influence of thermal fluctuations. This is done by checking the expected energy difference  $\Delta E$  after a possible transition to another state. If  $\Delta E = E_{\text{new}} - E_{\text{old}} < 0$  the system will automatically switch to the new state. If  $\Delta E > 0$  the new state gets accepted with a probability

$$p_{\text{new}} = \frac{1}{Z_N} \exp\left(-\frac{E_{\text{new}}}{k_B T}\right), \quad (4.60)$$

where

$$Z_N = \sum_{i=1}^N \exp\left(-\frac{E_i}{k_B T}\right) \quad (4.61)$$

is the canonical partition function [12].  $Z_N$  is a sum over all possible thermodynamic realizations of the  $N$ -particle configuration and hence serves as a normalization factor for the probability  $p_{\text{new}}$  of a particular state.

If  $\Delta E > 0$ , the ‘‘Monte Carlo part’’ gets introduced by comparing the probability for the new state  $p_{\text{new}}$  to a random number  $x \in [0; 1]$ . If  $p_{\text{new}} \geq x$ , the new state gets accepted and if  $p_{\text{new}} < x$  the system will continue to search for a lower energy state at another point in phase space. This method is called the Metropolis algorithm [118]. It should be noted that the total energy  $E$  that is needed to compute  $p_{\text{new}}$  involves all contributions originating from the interactions among  $N$  particles. For a system of single domain particles this means that changing randomly the orientation of one particle changes the field sensed by the other spins. It usually takes a large number of random moves to finally find a new state for the system with relatively large energy barriers  $\Delta E > 3k_B T$  that is either lower in energy or gets

accepted by the condition given before. As described in Sec. 4.1 a single domain particle with uniaxial anisotropy has two stable states in zero magnetic field, so the orientational distribution of the magnetic moments is concentrated around these energy minima [119].

### 4.3.2 Implementation

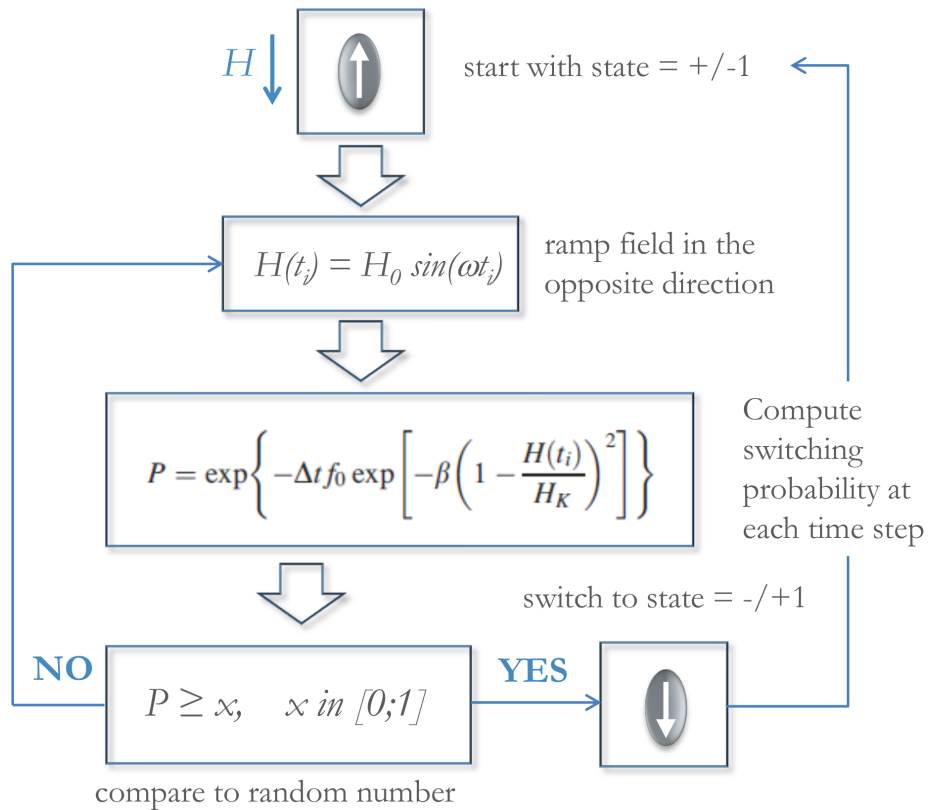


Fig. 4.11. – Flow diagram of the implemented Metropolis algorithm to model the timing jitter caused by thermal fluctuations when the free layer of the MTJ in the TMR fluxgate sensor is periodically switched by an external alternating field  $H(t) = H_0 \sin \omega t$ .

We have implemented the Metropolis algorithm to simulate the time domain signal of the TMR fluxgate sensor following the work presented in Refs. [98] and [119], where the master equation ansatz is used. The implementation of the Metropolis rule is modified here in a way, that the possible magnetization states of the single domain particle are reduced to a two-state system. This saves a large amount of computation time and can be justified by the fact that intermediate states are very unlikely to be acquired by the system because of the distinct shape of the energy landscape. The time evolution of the population probability of the two stable magnetization states, which correspond to the energy minima in the free energy (see. Sec. 4.1), is given by

the master equation (see also Eq. 4.32). If we assume state 1 to be higher in energy  $E_1$  the master equation, which describes now the population probability of state 2 ( $P_2$ ), reads

$$\frac{dP_2}{dt} = f_{12}P_1 - f_{21}P_2, \quad (4.62)$$

where  $f_{12}, f_{21}$  are the transition rates from state 1 to state 2 and vice versa. If  $E_1 \gg E_2$  we can further assume that  $f_{21} \approx 0$  and together with  $P_1 + P_2 = 1$  solve Eq. 4.62 and get for the population probability of the state with higher energy ( $P_1 \equiv P, f_{12} \equiv f$ )

$$P = \exp(-ft) = \exp \left\{ -\Delta t f_0 \exp \left( \frac{\Delta E}{k_B T} \right) \right\} = \exp \left\{ -\Delta t f_0 \exp \left[ -\beta \left( 1 - \frac{H(t_i)}{H_K} \right)^2 \right] \right\}, \quad (4.63)$$

where we have used the rate equation  $f = f_0 \exp(-\frac{\Delta E}{k_B T})$ . This is the probability during each time step  $\Delta t$  for the particle to switch to the other state, when the field  $H(t)$  is ramped up. In the TMR fluxgate sensor the “particle” is the the free layer of the magnetic tunnel junction which is modeled as a single macrospin that is switched periodically under the influence of an alternating magnetic field  $H(t) = H_0 \sin \omega t$ . The amplitude  $H_0$  has to be large enough to fully switch the magnetization. Because the TMR fluxgate sensor is switched along its easy axis  $H_0 > H_K = 2K/\mu_0 M_S$  has to apply. In Fig. 4.11 a flow diagram of the implemented algorithm is shown, which can be described as follows:

1. Start with the magnetization of the particle pointing either up (state = +1) or down (state = -1).
2. When increasing the time by  $i$  time steps of size  $\Delta t$  the field varies as a sinusoidal function  $H(t_i) = H_0 \sin \omega t_i$ .
3. At each time  $t_i$  the switching probability  $P$  is computed according to Eq. 4.63.
4. The switching probability  $P$  is compared to a random number between  $0 \leq x \leq 1$ .
5. If  $P \geq x$ , the particle switches to the other state.
6. If  $P < x$ , the field is further increased and  $P$  is computed again. This is repeated until the particle switches.

In Listing 4.1 the MATLAB<sup>®</sup> function is given, in which the Metropolis rule is implemented. The `if (stateold*H/abs(H)==-1)` statement checks if the field is applied anti-parallel to the current state. This means we are in the regime where a thermally activated transition to the other minimum is expected when the energy

barrier is lowered as the field increases. `prob(t0,f,H,Hc,H0,A)` computes the switching probability in each time (or field) step according to Eq. 4.63 and has the inverse of the attempt frequency  $t_0 = f_0^{-1}$ , the frequency  $f$  of the alternating field  $H$  with amplitude  $H_0$ , the zero temperature coercive field  $H_C \equiv H_K$  and the thermal stability ratio  $A \equiv \beta$  as input parameters.

Listing 4.1 – MATLAB<sup>®</sup> function to calculate the magnetization state according to the Metropolis rule

---

```
function [statenew, probability] = calcstate(t0,f,H,Hc,H0,A,stateold)
if (stateold*H/abs(H)==-1)
    probability = prob(t0,f,H,Hc,H0,A);
    y = rand;
    if (probability >= y)
        statenew = stateold*-1;
    else
        statenew = stateold;
    end
else
    probability = 0;
    statenew = stateold;
end
```

---

The SFD is computed from executing  $p$  switching cycles (see Listing 4.2), where one cycle involves switching once from  $-1$  to  $+1$  and once from  $+1$  to  $-1$  (see code snippet below). Then, together with the frequency  $f$  the total observation time is determined, which also defines the number of data points for given time step  $\Delta t$ . To avoid a loss in accuracy at higher frequencies a discretization factor  $x$  is introduced which ensures that the time step  $\Delta t$  scales according to the applied frequency of the external field. The `drive_field(f,H_0,t,delta_t,N,p)`-function which generates the external driving field is given in the appendix A.3 and consists of positive and negative ramps extending over half the period time  $T$  with amplitude  $H_0$ . This approach was given the preference over using sine or cosine functions for the external field, because it ensures that the rate is constant during the observation of the switching events. Furthermore, this way the results generated here are more consistent and hence better comparable to values from the literature. In any case, for the application in the TMR fluxgate sensor we assume that the field amplitude  $H_0 \gg H_C$  (here, the temperature-dependent switching field is addressed by  $H_C$ ), so a sine or cosine function can in principle be found that has the same field rate as the triangular function.

In the `for`-loop, the current state of the magnetization is calculated by the `calcstate`-function (shown above) according to the Metropolis rule. If `statenew` which is returned by `calcstate` is not equal to `statecurrent` (which is the state *before* invoking `calcstate`), the field  $H(n)$  at a time  $t_n$  is saved as a switching field.



Afterwards, the remaining zeros in the `switching_field`-array get stripped and the SFD is generated using MATLAB®'s `histc`-function, which generates a histogram. This means that the values in `switching_field_nozeros` are counted that fall into the intervals given by `hist_interval`, which in this case starts at  $\mu_0 H_C = 0.48$  mT and ends at  $\mu_0 H_C = \mu_0 H_K = 0.5$  mT with stepsize of `bin_width = 5e-3` given in Oe<sup>1</sup>.

Listing 4.2 – MATLAB® code for the evaluation of the SFD

---

```
f = 1e3; % frequency of the driving field in Hz
x = 1e5; % discretization factor
delta_t = 1/(x*f); % sampling time interval in s
H_0 = 10; % amplitude of driving field in Oe

p = 100; % number of observed cycles
t_obs = p*1/f; % overall observation time in s

rate = H_0*f*4; % field sweep rate

T = 1/f;
N = round(t_obs/delta_t); % number of data points, signal length

t = (0:delta_t:t_obs); % time vector

[H, delta_H] = drive_field(f, H_0, t, delta_t, N, p);

H_c = 5; % zero temperature coercive field in Oe
t_0 = 1e-9; % inverse attempt frequency
A = 1e4; % thermal stability ratio
statenew = 1;
switching_field = zeros(1,N);

for n = 1:N
    statecurrent = statenew;
    [statenew, probability] =
        calcstate(delta_t,t_0,H(n),H_c,A,statecurrent);
    if (statenew == statecurrent)
    else
        switching_field(n) = abs(H(n));
    end
end

% eliminate zeros from switching_field array
switching_field_nozeros = switching_field(switching_field ~= 0);
```

---

<sup>1</sup>In the outdated cgs unit system, the dimensions of the magnetic field  $H$  (Oe - Oersted) and the magnetic induction  $B = \mu_0 H$  (Gs - Gauss) are equivalent, because  $\mu_0 = 1$ . The conversion to SI units yields  $1 \text{ Oe} \equiv 1 \text{ Gs} = 10^{-4} \text{ T}$ .

```

% make histogram from switching field data
bin_width = 5e-3;
hist_interval = H_c-500*delta_H:bin_width:H_c;
sfd = histc(switching_field_nozeros, hist_interval);
sfd_norm = sfd/(sum(sfd).*bin_width);
[max_counts, max_index] = max(sfd_norm);
max_field = hist_interval(max_index);

```

---

### 4.3.3 Results

Fig. 4.12 shows simulation data (markers) and the analytical solution (lines) of the SFD from Eq. 4.48 for a typical parameter set of a TMR fluxgate sensor. The simulation data are generated from 100 switching cycles and show remarkable agreement with the analytical result. This can be explained by noticing, that the simulation is in a sense a way of integrating the master equation Eq. 4.32 numerically. The good agreement on the one hand supports our analytical model, where thermal fluctuations or randomness are not explicitly introduced, but only indirectly via the rate equation Eq. 4.18 and on the other hand provides a justification for possible extension of the simulation to model more complex systems than a single macrospin. The simulation serves as a direct demonstration of the TMR fluxgate signal generation over a number of switching cycles and hence validates, that the standard deviation of the switching fields given by the second moment of the SFD in Eq. 4.52 can be considered as a measure for determining the noise of the measurement principle.

Another validation of the selected simulation approach was obtained by comparing the data to a Langevin-dynamics simulation. The stochastic LLG equation (Eq. 4.20) can be rewritten as

$$\frac{dM_i}{dt} = A_i(\mathbf{M}, t) + B_{ik}(\mathbf{M}, t)\xi_k(t), \quad (4.64)$$

where  $\xi(t)$  is the thermal field. Eq. 4.64 gives a system of Langevin equations with multiplicative noise, which can be effectively solved using the Heun method [120–122]. In such a simulation, the exact reversal trajectory of a single spin is computed under the influence of thermal fluctuations. This creates a magnetization signal with fluctuations on a short time scale  $t \approx 10^{-13}$  s, which can switch between two stable states  $\mathbf{M} \cdot \hat{e}_z = \pm 1$  on longer time scales. Due to limitations in computation time,  $10^7$  T/s is the slowest field rate that can be simulated in a reasonable amount of time. The switching fields from the stochastic  $\mathbf{M}(t)$ -signal are extracted by checking when the signal changes from  $-1$  to  $+1$ . The Monte Carlo simulation is carried out the way described above, but with an additional function included in `calcstate`, which computes the attempt frequency according to Brown's formula (4.22) in each time step. As it is shown in Fig. 4.13 the simulation data from the stochastic LLG equation (rectangular markers) are in excellent agreement with

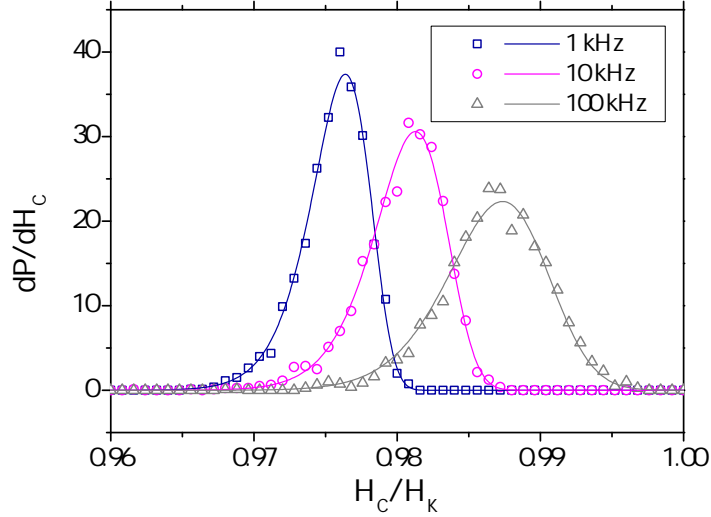


Fig. 4.12. – Simulated and analytical switching field distributions for single domain particle with a thermal stability ratio of  $f_0 = \text{const.} = 10^9$  Hz,  $\beta = 10^4$  and  $\mu_0 H_K = 0.5$  mT. The frequencies  $f = 1, 10, 100$  kHz for the external driving field with amplitude  $\mu_0 H_0 = 1$  mT relate to the field rate  $R$  by  $R = 4\mu_0 H_0 f$ .

the data generated by the Monte Carlo code (dots). The data were simulated for parameters typically found in magnetic recording media [87]. We have also plotted the analytical results from Eqs. 4.48 and 4.57. The fact that the analytical SFD with the dependence for the attempt frequency included reproduces the Langevin- and the Monte Carlo-simulation data so well does further underline the shortcomings of the rate-dependent coercivity models that use  $f_0 = \text{const.}$  (see Sec. 4.2.1).

The fact that the two simulation approaches produce the same SFDs is remarkable on the one hand, given the simplicity of the Monte Carlo simulation, but also natural on the other hand, because the Monte Carlo method of solving the master equation represents a “coarse-graining” of the rotational magnetization dynamics with additional stochasticity given by Eq. 4.20. The Monte Carlo simulation does not “see” the thermal fluctuations taking place at a time scale of  $10^{-13}$  s, but correctly models the hopping from  $-1$  to  $+1$  and vice versa by the Arrhenius-Néel Law  $\tau = \tau_0 \exp(\frac{\Delta E}{k_B T})$ , that does not contain any microscopic information at first sight. However, as we have seen, the prefactor  $\tau_0 = f_0^{-1}$  is not a constant with respect to external parameters that change the potential in which the stochastic motion is taking place. The microscopic parameters  $\alpha$  and  $\gamma$ , which govern the damping, are reflected in the switching field distribution computed by the macroscopic Monte Carlo approach, that averages over the microscopic short-time fluctuations.

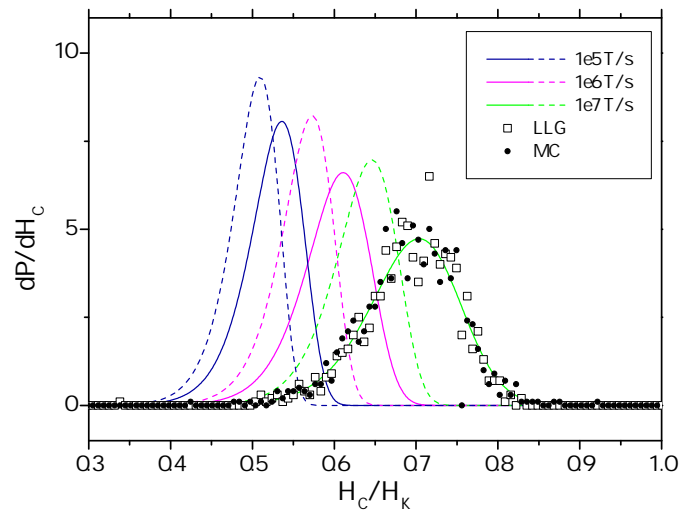


Fig. 4.13. – Analytical SFDs for field rates of  $10^5$ ,  $10^6$  and  $10^7$  T/s, where the dashed lines represent SFDs for  $f_0 = \text{const.} = 1.9 \cdot 10^{10}$  Hz according to Eq. 4.48 and the solid lines represent SFDs according to Eq. 4.57, where the field dependence of  $f_0$  is considered. The markers show simulated data at field rates of  $10^7$  T/s based on numerically solving the stochastic LLG equation (Eq. 4.20) (rectangles) and the Monte Carlo approach described in the text (dots). Further parameters:  $\mu_0 H_K = 1.508$  T,  $K = 0.3$  MJ/m<sup>3</sup>,  $V = (8 \text{ nm})^3$  ( $\Rightarrow \beta = KV/(k_B T) \approx 37$ ),  $\alpha = 0.02$

# Methods

This chapter covers the experimental methods used within this thesis. They include the fabrication of TMR fluxgate sensors (Sec. 5.1), digital data processing (Sec. 5.2), which is important for the estimation of the detectivity and the experimental characterization of the fabricated TMR fluxgate sensors (Secs. 5.3 and 5.4).

## 5.1 Fabrication techniques

In this section we will describe the methods used to fabricate the TMR fluxgate sensors. These methods include the standard microfabrication methods also used on large industrial scales for the production of modern integrated circuits. There exists a vast amount of literature on the methods described below and - if not explicitly stated otherwise - we have used here Refs. [123–125] as the main resources for this section. We will outline briefly all methods used in the fabrication process of the TMR fluxgate sensors, which starts with sputter deposition of the multilayers for the magnetic tunnel junctions and ends by the a photoresist lift-off process step to form the current line. The basic protocol for the TMR fluxgate fabrication can be summed up as follows:

1. A magnetic multilayer system is deposited on a piece of silicon wafer with 50 nm thermal oxide using sputter deposition.
2. Out of this multilayer the magnetic tunnel junctions are patterned, which have dimensions in the  $\mu\text{m}$  range.
3. An electrically insulating layer is deposited over the entire sample, through which vias are opened to the backside and top contacts of the MTJs.
4. The top contact line and contact pads are formed using a process that dissolves the photoresist under the deposited material (lift-off process).
5. A second insulator is deposited for galvanic separation of the top contacts from the current line. Vias are etched through to the top and backside contact pads.
6. The current line and contact pads are deposited and patterned using another lift-off process.

### 5.1.1 Sputter deposition

Sputter deposition belongs to the group of physical vapor deposition (PVD) methods for thin film deposition. In contrast to chemical vapor deposition (CVD) methods, in a PVD method the evaporated material does not undergo any chemical reaction, but is only physically manipulated. During sputter deposition, in an ultra-high vacuum chamber (base pressure  $p \approx 10^{-8} - 10^{-6}$  mbar) a noble gas plasma is ignited and the positively charged gas atoms are accelerated towards the target material, which serves as the cathode. The target material is sputtered off and deposited on the substrate, which is placed below the target material. The energies of the target material atoms are determined by the applied voltages, at which the plasma atoms are accelerated towards the target and the target's material properties (binding energy etc.). In order to enhance the ionization rate in the plasma, magnets are placed behind the target. The resulting Lorentz force acts mainly on the electrons in the plasma, which then propagate on circular paths around the magnetic field lines and so increases the number of generated ions. In such a magnetron sputtering system, the sputter yield is notably increased, which allows faster deposition rates. The process parameters such as base and process pressure as well as acceleration voltage significantly influence the physical properties (texture, grain size etc.) of the deposited thin film, so careful calibration is required in order to have reproducible results.

The sputtering machine used for the sample fabrication in this thesis was a customized UNIVEX 450C by Oerlikon/Leybold Vacuum consisting of two main chambers with a chamber for the robot arm for sample transfer from the load lock in between. Additionally, an oxidation chamber was available, however, this was not used as all materials were sputtered from 4 in targets. Six targets could be mounted in each chamber, however, only one chamber was fully equipped with voltage supplies for all six targets. In the other chamber, four targets were available. This provided the necessary amount of materials needed for magnetic tunnel junction multilayers.

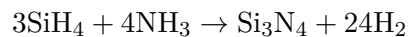
### 5.1.2 Ion beam etching

Ion beam etching (IBE) is a method used in patterning of micro- and nanostructures. It can be seen as the complementary method to sputtering with the sample being in the place of the sputtering target. A beam of argon ions is accelerated towards the sample from which the exposed material is sputtered off. Usually, parts of the sample surface are protected from milling by a mask of resist, that was previously patterned using optical or electron beam lithography. IBE is a physical etching method that produces a highly anisotropic etching profile, which makes it possible to create nanostructures with high aspect ratios. Problems in the IBE process are redeposition of sputtered material and shadowing of neighboring structures. Shad-

owing can be partly overcome by rotating the sample, redeposition effects can be controlled by the applied incident angle of the ion beam.

### 5.1.3 Plasma Enhanced Chemical Vapor Deposition

Plasma Enhanced Chemical Vapor Deposition (PECVD) is a method used in CMOS processing to deposit thin films from the range of nanometers up to several microns. In the reaction chamber the sample is usually heated up to 100–400°C. The precursor gases, that contain the desired chemical components of the film to be deposited (e.g. silane SiH<sub>4</sub> and ammonia NH<sub>3</sub>) are then let into the chamber at a controlled flow rate. In the reaction chamber a plasma is then ignited using a radio frequency voltage (150 MHz). In the following chemical reaction, a thin film is grown on the sample surface, that consists of the reaction product. The reaction is made possible at relatively low temperatures (compared to chemical vapor deposition methods without plasma), due to the creation of free radicals by the electrons in the plasma. For the deposition of silicon nitride Si<sub>3</sub>N<sub>4</sub> with the precursors silane and ammonia the chemical reaction is as follows:

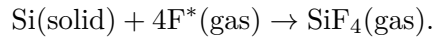


The resulting thin film is non-stoichiometric with varying hydrogen content. The high hydrogen content may reach up to 30 at% and is a main cause of degradation in CMOS devices. Hence, a low hydrogen content in the precursor gas is favorable [126], [127]. For this purpose, pure nitrogen can be used instead of ammonia, in case a electron cyclotron resonance source is available to obtain the required electron energies [127].

### 5.1.4 Reactive ion etching

Reactive ion etching (RIE) is a dry-etching method, that uses a chemically reactive plasma to enhance the etching rate. Compared to IBE, RIE is chemically selective and is widely used to etch silicon and its compounds with nitrogen and oxygen using for example sulfur hexafluoride (SF<sub>6</sub>) as etchant. The base pressure is usually a few millitorr. The main chamber consists of two parallel plates, where one is designed to serve as the substrate holder. The substrate holder is electrically isolated from the chamber. The plasma is produced by applying a radio frequency voltage (typically 13.56 MHz) to the substrate holder. The gas becomes ionized and because of the higher electron mobility the electrons will be able to follow the strong RF voltage. Electrons, that hit the walls of the chamber are fed to ground, however, on the substrate holder - as it is electrically insulated - a negative charge builds up, the so-called self bias. Due to this voltage, the positive ions in the plasma get accelerated towards the substrate and cause a physical etching additionally to the chemical

reaction. This way, the etching process can be tuned to deliver more anisotropic etching profiles compared to fully chemical etching processes. For etching of Si, SiO<sub>2</sub> and Si<sub>3</sub>N<sub>4</sub> the etching chemistry is dominated by the fluorine radicals that form in the SF<sub>6</sub> plasma given by the reaction [128]



Temperature is an important parameter to control the etching profile in RIE. The etching process with fluorine based plasmas was shown to produce more anisotropic profiles if the substrate was cooled down to  $-120^\circ\text{C}$  [129]. Also, the mask material plays an important role. In general, metallic masks are preferred, because they do not collect any charges and therefore allow to control the process more precisely via the external process parameters.

### 5.1.5 Photolithography process

The patterning of the microstructures that serve as the components for a TMR fluxgate sensor - i.e. a magnetic tunnel junction with contact leads and a current line for the alternating external field - was realized by photolithography for the pattern transfer to the substrate and the methods described in Secs. 5.1.1 to 5.1.4. As already outlined at the beginning of this section the whole patterning process consists of several process steps, where in each step the use of complex and technologically very advanced methods is required. Despite efforts to develop methods, which allow the patterning of structures with dimensions of only a few nm using electron or ion beams, photolithography still is the method of choice in the semiconductor industry. The main advantage of photolithography over direct-write methods using charged particle beams is the time needed for the exposure. With increasing silicon wafer sizes (the current industry standard diameter is 300 mm (12 inch) and was 2 inch in 1971 [130], introduction of 450 mm wafers is planned for the end of this decade [131]) the advantage of optical methods becomes even more important in competition with the aim for further miniaturization of the structures. The minimum feature size of photolithography, which is determined by the wavelength of the used light, could be pushed below 100 nm by using extreme UV light with a wavelength of 193 nm for exposure [132]. Multi-beam tools for resist- and maskless nanopatterning are just entering the market now [133].

A standard photolithography process step usually requires the following materials and machines:

- a mask with the master pattern, usually a quartz plate with a light-absorbing chromium layer, which forms the pattern to be transferred to the wafer,



- photoresist, a resin with photosensitive chemicals which becomes either soluble (positive resist) or insoluble (negative resist) in the developer after controlled exposure to an optical light source,
- a spin coater, that is used to apply the photoresist as a thin layer on the sample to which the pattern on the mask has to be transferred,
- a mask aligner, a machine used to align the mask to existing structures on the sample and to execute the controlled exposure to light,
- the developer, in which the (un-)exposed (negative) positive photoresist is dissolved.

Photolithography has to be carried out in a cleanroom environment with UV-filtered light in order to ensure controlled exposure of the resist. In the following, we will describe the lithography process step by step that was developed to fabricate a TMR fluxgate sensor out of a sputter deposited thin film multilayer on a silicon wafer. Typical multilayers are discussed in detail in Sec. 5.3.1. For the design of this lithography process, several practical parameters had to be taken into account in order to keep the fabrication as simple as possible:

- Use as few masks as possible.
- Use as few materials and methods as possible.
- Use uncritical structural dimensions, where not explicitly required for the device performance.
- Find a reasonable trade-off between the number of microstructures produced on one sample and increased fabrication complexity due to proximity effects.
- Consider the availability of the equipment in different locations and do as few transfers as possible with resist masks.

The last point mentioned refers to the fact, that not all equipment was situated in the same laboratory (AIT: sputter deposition, IBE; Vienna University of Technology: cleanroom with photolithography workbench, PECVD, RIE). The cleanroom at the Institute of Solid State Electronics at the Vienna University of Technology is of class 100 (max. 100 particles with diameter  $\geq 0.1\mu\text{m}$  in  $1\text{m}^3$  of air) in the lithography area and of class 10 000 in the PECVD/RIE areas. At AIT no classified cleanroom environment was available when this work was carried out.

In each of the following sections we give a table of photolithography parameters used in each step. They refer to the basic procedure that has to be carried out to get a photoresist mask which protects parts of the sample from the following etching or deposition of a material:

1. Clean the sample thoroughly using acetone and isopropanol in an ultrasound bath.
2. Put the sample on the chuck of the spin coater and turn on the vacuum pump to keep it fixed.
3. Apply manually a few drops of photoresist with a syringe and start the spinner immediately afterwards.
4. Put the sample on a hotplate for the softbake, that is needed to evaporate the solvent contained in the photoresist.
5. In the mask aligner, using a microscope align the sample to the mask using predefined markers.
6. When the alignment is done, the coated sample gets pressed against the mask, which needs to be very clean in order to avoid artefacts.
7. Apply the required exposure dose, which sensitively depends on a number of parameters such as structure size, resist thickness and softbake duration.
8. Put the sample to the developer solution for a distinct duration, which mostly depends on the exposure dose.
9. Rinse off the developer with DI water and dry with compressed pure air or nitrogen.

In each of these steps there is a complex interplay of process parameters, which on the one hand opens up a lot of possibilities for improvement but on the other hand can make it very tedious to find a working process in the first place. The process parameters given in the tables in the following sections were taken over from earlier works carried out in the Nano Systems group at AIT and were only modified, if considered necessary. The photolithography mask (see Appendix B.1) was fabricated at ML&C in Jena, Germany and consisted of  $3 \times 3$  array of masks for each lithography step. Additionally to the six lithography steps described below, there were two more masks with varying dimensions of the MTJ ellipses and one mask, which was used to remove the resist on the sample's edge area. Due to the interplay of the resist's viscosity, surface tension and the centrifugal forces acting during the spin coating the resist gets piled up in the corners of the square sample, which is counterproductive for uniform contact of the mask to the sample during exposure. This leads to projection errors, i.e. the pattern from the mask is not correctly transferred to the resist, which becomes increasingly important the smaller the structures are that need to be patterned. Therefore, this additional process step was not carried out for all six masks, but only for the patterning of the MTJ ellipses in Step 2 and the MTJ top contact vias with a nominal diameter of  $1\mu\text{m}$  in Step 3.

The positive photoresist AZ MIR 701 by the company Microchemicals was used throughout this process. It is photosensitive in a range of wavelengths from 310 - 440 nm, which corresponds to the i-, h- and g-lines of a Hg lamp [134].

### Step 1 - Patterning of the backside contact

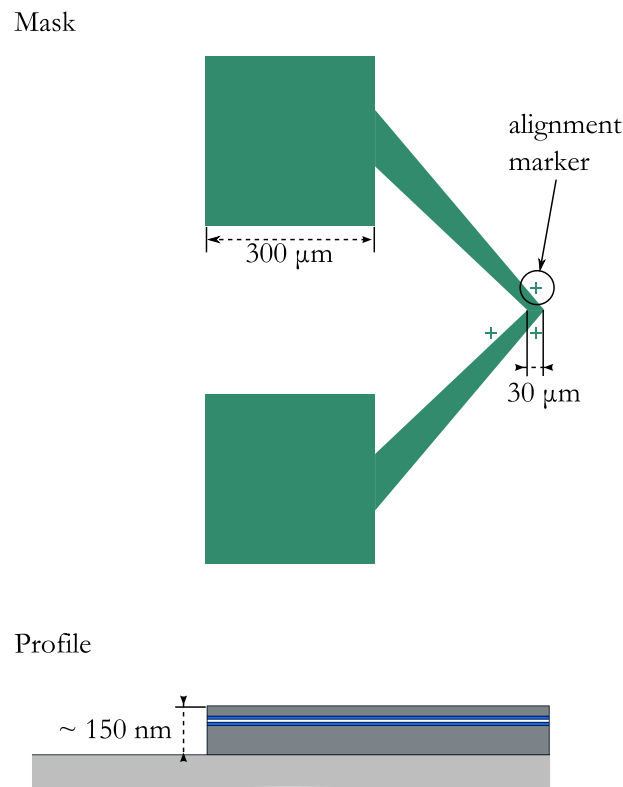


Fig. 5.1. – Photolithography mask element and profile (not to scale) of the sample after patterning of the backside contact.

In Fig. 5.1 the mask and the side profile of the backside contacts are shown which are patterned out of the sputter deposited multilayer. The sputtering parameters of a typical layer sequence are given in Appendix B.2. Such a sequence consists of a seed layer, which should provide low electrical resistance and conditions to grow the subsequent MTJ layers in the appropriate texture to achieve high TMR (see Sec. 2.4.3). The MTJ layers consist of two ferromagnetic CoFeB layers separated by a MgO layer. The layer sequence finishes with a capping that serves as a protective layer against oxidation and as a top contact. Furthermore, layers are needed that provide a pinning mechanism to keep the magnetization of one of the MTJ electrodes fixed. This will be discussed in more detail in Sec. 5.3.1.

In the first lithography step, the contact pads are designed large enough to allow wire bonding once a working device is finished. Wire bonding is a method used for creating IC interconnects to a printed circuit board using a Au or Al wire, that is

welded to the contact pads using ultrasonic power [135]. After the resist mask has been applied to the multilayer, which is deposited on a piece of a standard 4-inch Si wafer with a 50 nm thermal SiO<sub>2</sub> layer, the sample is etched using IBE (Argon ion beam with  $\approx 500$  eV and an incident angle of 90°) with a HIDEN Analytical™ secondary ion mass spectrometer (SIMS) to control the etching depth. A typical SIMS data profile is shown in Fig. 5.2, where the Mg signal originating from the MgO tunnel barrier layer has the most pronounced peak. This signal serves as a good indicator to stop the etching process in the layer that forms the backside contact. If the sample is underetched in this process step and a continuous metal film is still left on the sample surface, this will be compensated in the next process step, in which the magnetic tunnel junction elements are patterned.

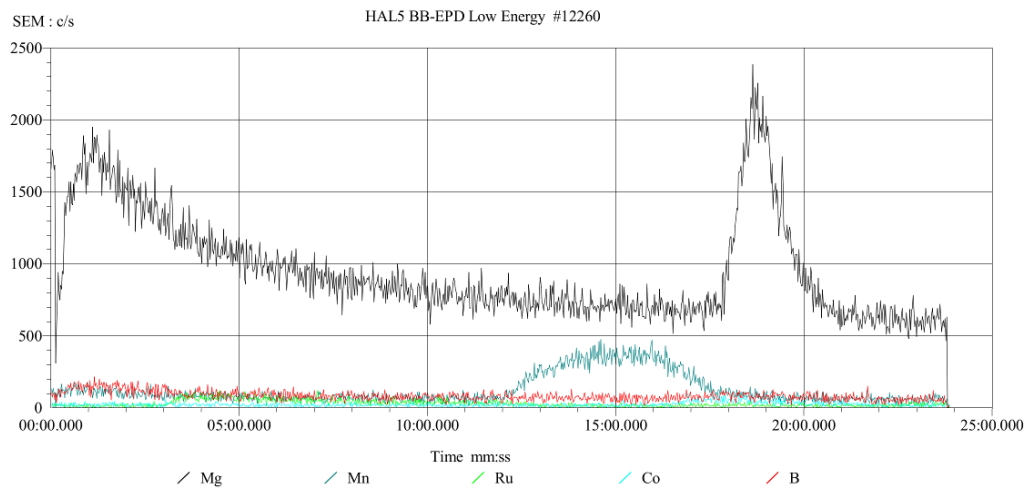


Fig. 5.2. – Mass spectrometer signal recorded during ion beam etching to monitor the etching progress.

resist	MIR 701
spin coating	35 s at 4000 rpm
ramp	255
softbake	60 s at 120°C
exposure	10 s
developer	AZ MIF 726
dev. time	40 s
H <sub>2</sub> O	10 s

Tab. 5.1. – Lithography parameters for Step 1

## Step 2 - Patterning of the magnetic tunnel junction element

The magnetic tunnel junctions are patterned out of the backside contact pillars, that were created in the first process step. As shown in the magnification in Fig. 5.3, the MTJs are ellipses with an aspect ratio 1:2 that are patterned at the centre of backside contact area. The lithography in this step is more critical than in the first one, because the dimensions of the structures to be patterned are below  $10\mu\text{m}$  as compared to a minimum lateral dimension of  $30\mu\text{m}$  in the previous step. This requires an additional exposure step to remove the resist on the edges of the sample, that gets piled up during the spin coating and inhibits a homogeneous contact of the mask to the resist. The resist-mask contact is essential to ensure a 1-to-1 master pattern transfer and is a necessary prerequisite for finding reliable exposure and development time parameters. If the contact is not good enough there will be issues with over- or underexposure of certain parts of the sample, which can lead to undesired fringing of the structures. Such uneven edges also have an impact on the magnetic behavior of the MTJs, because the fringes will cause the formation of specific domain patterns. Furthermore, the exposure and development times had been adjusted in order to obtain reproducible structures. In Fig. 5.4 a scanning

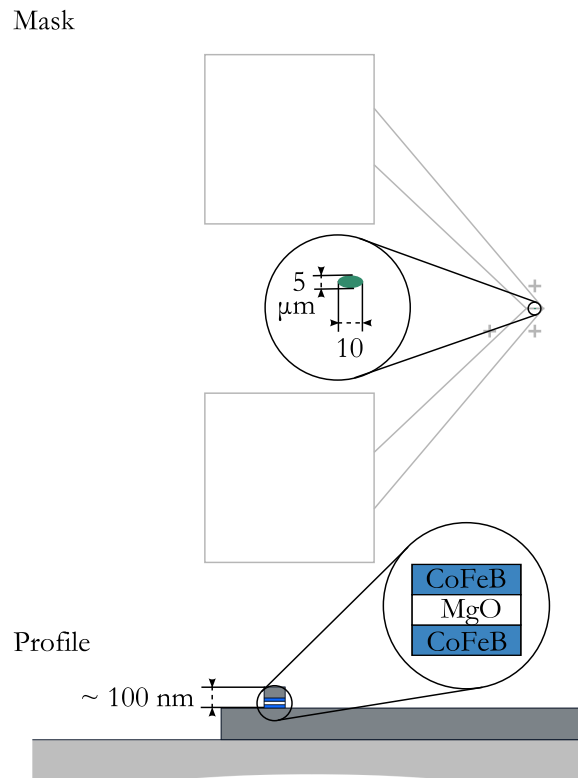


Fig. 5.3. – Photolithography mask element (ellipse) and profile (not to scale) of the sample after patterning the MTJ pillar. The mask of step 1 is sketched in gray for better orientation, where the ellipse is located, as mask 2 consist of very dilute structures.

resist	MIR 701
spin coating	35 s at 4000 rpm
ramp	255
softbake	60 s at 120°C
edge removal exp. and dev. time	20 s, 25 s
exposure	6 s
developer	AZ MIF 726
dev. time	45 s
H <sub>2</sub> O	10 s

Tab. 5.2. – Lithography parameters for Step 2

electron microscope image is shown after IBE and the mask removal using ultrasonic baths of acetone and isopropanol. The ellipses axes have the desired dimensions and even edges without notable fringes, that could have an impact on the magnetic switching behavior.

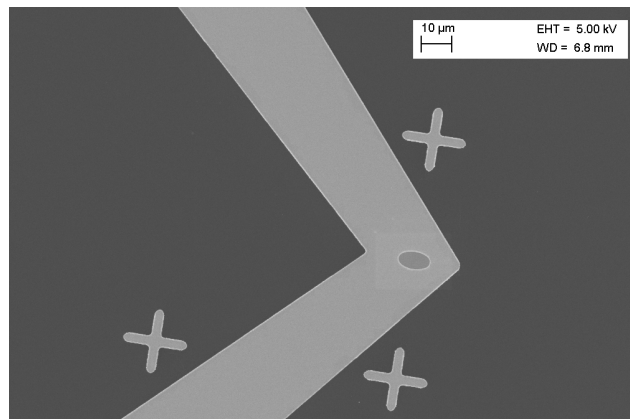


Fig. 5.4. – Scanning electron microscope image of the patterned MTJ pillar after removal of mask 2.

### Step 3 - Etching of the vias to the backside contact pads and MTJ top contact

The third mask is required to open vias through electrically insulating silicon nitride (Si<sub>3</sub>N<sub>4</sub>), that is deposited using Plasma Enhanced Chemical Vapor Deposition (PECVD, see sec 5.1.3) after the second lithography step. The Si<sub>3</sub>N<sub>4</sub> is deposited using a silane-nitrogen mixture (2%-SiH<sub>4</sub>) and ammonia (NH<sub>3</sub>) as precursor gases, which are fed to the chamber at flow rates of 700 and 18 sccm, respectively. The sample holder plate was heated to a temperature of 100°C and the deposition time was set to 10 minutes, which corresponded to a layer thickness of 120 nm. The film thickness was verified by refractometry measurements directly after the deposition. Si<sub>3</sub>N<sub>4</sub>

films are commonly used as gate dielectrics for field effect transistors (FETs) and usually deposited at temperatures above 250°C, because free hydrogen in the film significantly influences the performance of these devices. However, several studies have found that also PECVD Si<sub>3</sub>N<sub>4</sub> films deposited at temperatures even as low as room temperature meet the required properties for FET devices [136, 137]. Because elevated temperature exposure over a noticeable time span would probably have led to interlayer material diffusion in the magnetic multilayer, we chose to use low temperature PECVD. During the measurement of the processed samples we found that the film deposited this way met the requirements for electrical insulation in the frequency range where the TMR fluxgate sensors were operated. After the Si<sub>3</sub>N<sub>4</sub>

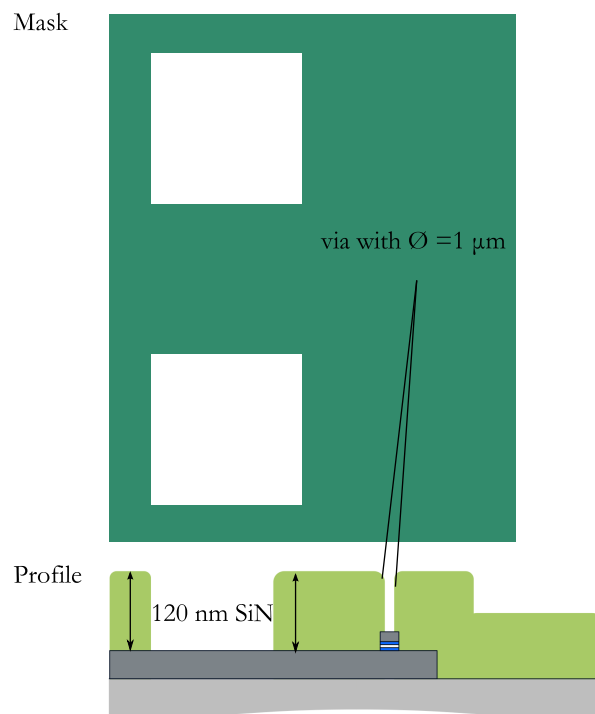


Fig. 5.5. – Photolithography mask element for step 3 (etching of the vias to the backside contact pads and the MTJ top contact), profile (not to scale) of the sample after RIE.

is deposited over the whole sample vias have to be opened to contact the backside and the top metallization of the MTJ. In Fig. 5.5 the third mask with the contact openings over the large backside contact pads and a small hole of 1 μm diameter on top of the MTJ ellipse is shown together with the side profile, that is created after the vias have been etched through. The main challenge here lies in the differences of the lateral dimensions of the 300 × 300 μm<sup>2</sup> squares for the backside contacts and the small holes for the top contact to the MTJ. In the mask design process it was decided to keep the hole to the MTJ as small as possible in order to have some tolerance for the alignment and the lithography. If the top contact opening would extend over the edge of the MTJ, a short cut is formed and no TMR can be measured. Furthermore,

resist	MIR 701
spin coating	35 s at 4000 rpm
ramp	255
softbake	60 s at 120°C
edge removal exp. and dev. time	20 s, 40 s
exposure	40 s
developer	AZ MIF 726
dev. time	60 s
H <sub>2</sub> O	10 s

Tab. 5.3. – Lithography parameters for Step 3

the lithography process parameters can be adjusted to overexpose in this process step, so that the effective diameter of the hole can be tuned to larger sizes. The fact, that a narrow-sized contact adds a considerable series resistance to the MTJ, which then limits the measured TMR amplitude was found to be of minor importance for our samples. This could be concluded from previous experiments, where MTJ pillars were fabricated in a one-step lithography process and contacted directly with tip probes. The TMR measured in these samples was not higher than in the samples patterned as TMR fluxgate sensors.

The exposure and development parameters given in Tab. 5.3 account for the

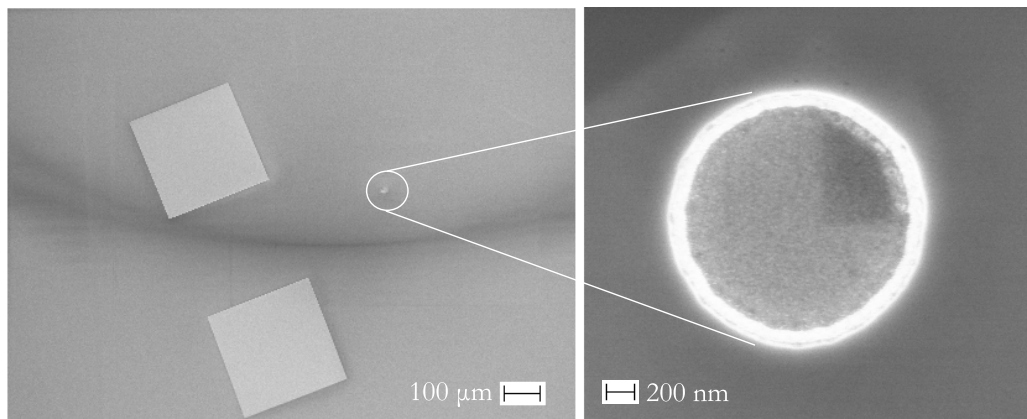


Fig. 5.6. – SEM images of a dummy sample (120 nm Si<sub>3</sub>N<sub>4</sub> on Au) after RIE and removal of mask 3.

fact, that the 1 μm-holes need overexposure in order to be properly dissolved in the developer. The overexposure of the openings for the backside contact pads do not lead to any problems regarding possible shortcuts etc., as due to the ion beam etching in the two lithography steps before the pads are now metal pillars on insulating SiO<sub>2</sub>. As in step 2, an edge removal process step was carried out to ensure good physical contact of the mask to the resist.

The etching of the vias was done using reactive ion etching (RIE, see Sec. 5.1.4) with



SF<sub>6</sub> as etchant gas. The etching time was monitored using a reflectivity measurement setup, where a laser spot had to be adjusted to hit the sample in a spot, where no resist was present. In practice, a dummy sample was used, if the etching time needed monitoring. However, the resist mask on the TMR fluxgate samples also influences the RIE rate, so the sample were left in the RIE long enough to make sure the small holes for the MTJ contacts got etched through. Because the top of the MTJ as well as the backside contact pads are both metal layers, they provided a natural etch stop for the RIE anyway. With the tolerances included in the design of the mask as mentioned before, the etching time in this step was not critical, but usually below 1 min. In Fig. 5.6 scanning electron microscope images are shown of a dummy sample of 120 nm Si<sub>3</sub>N<sub>4</sub> on Au after the RIE processing step. It shows, that the RIE process is sufficiently anisotropic to etch down to the Au surface without overetching the diameter of the hole to the MTJ top contact.

#### Step 4 - Deposition and lift-off of the top contacts

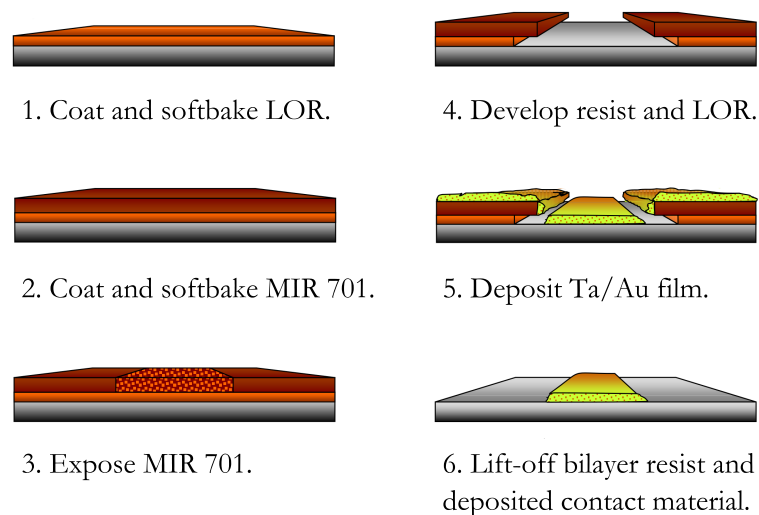


Fig. 5.7. – Illustration of the lift-off process (adapted from LOR 3A datasheet [138]).

The top contacts are created using a lift-off process after sputter deposition of a 100 nm Au film with 5 nm as a wetting layer. For a lift-off process a resist profile is needed that permits solvent to enter after the metallization has been deposited. This is illustrated in Fig. 5.7. Here, the “undercut” layer is created with LOR 3A (MicroChem<sup>®</sup>), a polymer (polydimethylglutarimide) which is not photosensitive but soluble in the used TMAH (tetramethylammonium hydroxide)-based developer. Development time in this step becomes critical with regard to the tuning of the undercut profile. After the softbake of the LOR resist the photosensitive MIR resist is spun onto the sample using the common parameters. Exposure and development time are adjusted to provide the desired undercut.

The lift-off is carried out using a heated bath (80°) of DMSO (dimethyl sulfoxide)

which serves as a less toxic alternative to the more widely used NMP (N-Methyl-2-pyrrolidone). Afterwards, the sample is cleaned in an ultrasound bath with acetone and isopropanol.

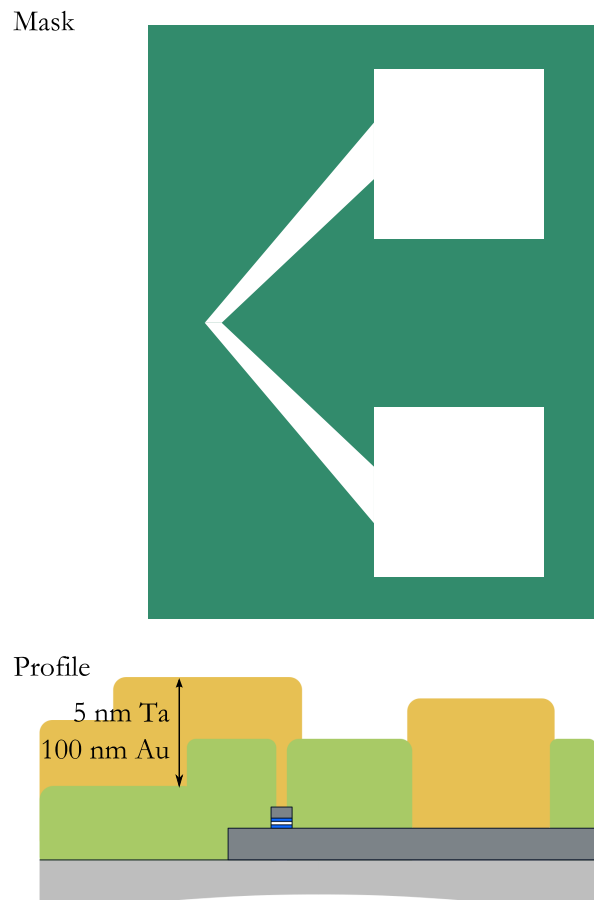


Fig. 5.8. – Photolithography mask element and profile (not to scale) after deposition of the top contact metallization and the lift-off.

### Step 5 and 6 - Vias to the backside and top contact pads and deposition of the current line

Steps 5 and 6 are basically repetitions of steps 3 and 4. After the deposition of the top contacts another 120 nm  $\text{Si}_3\text{N}_4$  are deposited by PECVD over the whole sample, which serve as an insulating separation to the current line, which is deposited in step 6. Then, vias have to be opened to the top and backside contact pads. In the last step, the current line and additional contact pad metallizations are deposited (5 nm Ta/100 nm Au) onto a LOR/MIR resist mask as described in the section before.

resist 1	LOR 3A
spin coating	35 s at 3000 rpm
ramp	155
softbake	5 min. at 170°C
resist 2	MIR 701
spin coating	35 s at 4000 rpm
ramp	255
softbake	60 s at 120°C
exposure	10 s
developer	AZ MIF 726
dev. time	35 s
H <sub>2</sub> O	10 s

Tab. 5.4. – Lithography parameters for Step 4

## 5.2 Digital Signal Processing

In this section, the fundamentals of digital signal processing will be reviewed. This is relevant for the evaluation of the data from both the simulation and the measurements. Data processing with the computer is based on the discretization of analog data from the physical sensors and measurement devices. Understanding the effects that originate from data sampling and data sets of finite lengths is important in order to compute meaningful frequency domain data.

### 5.2.1 Discrete Fourier Transformation

A time discrete signal  $f(t_j)$  is given by a series of values at equally spaced sampling points  $f_{-\frac{N}{2}}, f_{-\frac{N}{2}+1}, \dots, f_{\frac{N}{2}-1}$ . The discrete Fourier transform (DFT) assigns an equal amount of values to each sampling point following

$$\tilde{f}_n = \frac{1}{N} \sum_{j=-\frac{N}{2}}^{\frac{N}{2}-1} e^{-\frac{2\pi i n j}{N}} f_j \quad (5.1)$$

The  $\tilde{f}_n$  are called Fourier coefficients and they contain the same information as the  $f_j$ . Therefore, the inverse transformation applies:

$$f_j = \sum_{n=-\frac{N}{2}}^{\frac{N}{2}-1} e^{\frac{2\pi i n j}{N}} \tilde{f}_n \quad (5.2)$$

If a function is defined in a finite interval  $[0, T]$  at sampling points  $f_j = f(t_j) = f(j\Delta t)$  with  $\Delta t = T/N$  the sum in eq. 5.2.1 becomes an integral if we carry out the

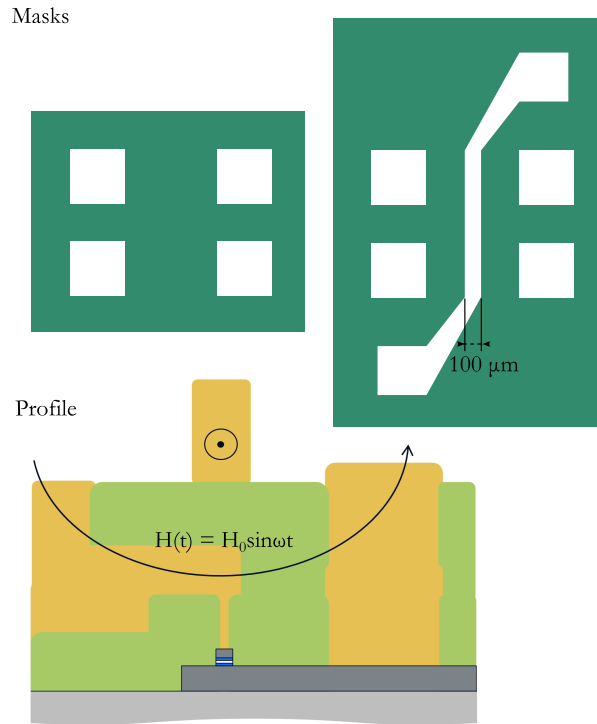


Fig. 5.9. – Step 5 (vias to backside and top contact pads) and step 6 (current line and contact pad metallization). In the profile view, the magnetic field from the current line is indicated, that is used to switch the free layer of the MTJ.

limits  $N \rightarrow \infty$  and  $\Delta t \rightarrow 0$ . The Fourier coefficients of the continuous function  $f(t)$  are then given by

$$\tilde{f}(\omega_n) = \frac{1}{T} \int_0^T e^{-i\omega_n t} f(t) dt \quad (5.3)$$

with  $\omega_n = n\Delta\omega = \frac{2\pi}{T}n$  and hence the continuous function  $f(t)$  can be expressed in terms of these coefficients as a Fourier series

$$f(t) = \sum_{n=-\infty}^{\infty} e^{i\omega_n t} \tilde{f}(\omega_n) \quad (5.4)$$

## 5.2.2 Laplace and Z-Transformation

Because the Fourier transform is only applicable to a certain set of functions (namely for which the Fourier integral (eq. 5.2.1) exists) there is a need for a more general transformation, that is not restricted to a purely imaginary transform variable  $\exp(i\omega t)$ , but uses the entire complex plane. Hence, the Laplace transformation is defined using  $s = \sigma + i\omega$

$$\mathcal{L}\{f(t)\} = F(s) = \int_0^{\infty} f(t) e^{-st} dt \quad (5.5)$$

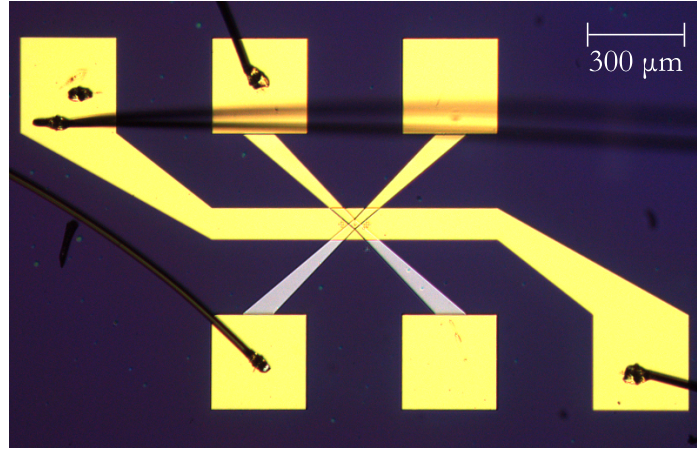


Fig. 5.10. – Optical microscope image of a TMR fluxgate sensor after annealing with bond wires.

One notable difference to the Fourier transform is that the signals fed into a Laplace transform do not have to decay anymore for  $t \rightarrow \infty$ , they can even grow exponentially if  $\sigma > 0$ . Furthermore, the integral exists only on the positive real axis, which is sufficient to model any physical system. The main application of the Laplace transform is the analysis of linear time-invariant (LTI) systems. Very generally spoken, LTI systems are a subset of physical systems where the output depends linearly on the input and the system will behave the same way at any given instant. The Laplace transform is a powerful tool to describe the relations between an input stimulus and the resulting output of a system that is modeled by a set of ordinary differential equations. Such a system could be a low-pass filter consisting of inductances and capacitances with a transfer function

$$H(s) = \frac{Y(s)}{X(s)} \quad (5.6)$$

where  $X(s)$  is the input and  $Y(s)$  is the output signal of the system [139]. For the case of time discrete signals, where the signal is only known at discrete sampling points  $f(t_j) = f(j\Delta t)$  the integral in eq. 5.2.2 reduces to a sum and by defining  $z = \exp j\Delta t$  we get the Z-transform

$$\mathcal{Z}\{f(t)\} = F(z) = \sum_{j=0}^{\infty} f(j\Delta t)e^{-j\Delta ts} = \sum_{j=0}^{\infty} f(j\Delta t)z^{-j} = f_0 + \frac{f_1}{z} + \frac{f_2}{z^2} + \dots \quad (5.7)$$

The transfer function of a system is defined analogous to the Laplace transform by  $H(z) = Y(z)/X(z)$ . More precisely, a time discrete system is described by a finite difference equation relating the output to the input and hence the z-transfer function reads

$$H(z) = \frac{b_m z^m + b_{m-1} z^{m-1} + \dots + b_1 z + b_0}{a_n z^n + a_{n-1} z^{n-1} + \dots + a_1 z + a_0} \quad (5.8)$$

### 5.2.3 Zeropadding

A digitally sampled signal in the time domain consists of  $N$  samples taken at intervals  $\Delta t$  the resulting output of the DFT will also consist of  $N$  values, which each correspond to frequencies spaced by  $1/(N\Delta t)$ :

$$\nu = \left( \frac{1}{N\Delta t}, \frac{2}{N\Delta t}, \dots, \nu_{\max} \right) \quad (5.9)$$

with

$$\nu_{\max} = \frac{\nu_S}{2} = \frac{1}{2\Delta t} \quad (5.10)$$

$\nu_{\max}$  is called the Nyquist frequency and is a fundamental upper limit for the highest frequency that can be detected in a signal sampled at a given rate  $F_S = 1/\Delta t$  (see also sec. 5.2.5). Eq. 5.2.3 is also known as the Shannon sampling theorem. From eq. 5.2.3 it follows that the resolution in the frequency domain is determined by the total length of the time record. The higher the number of samples  $N$ , the smaller the spacing of the FFT bins. Due to this fact, peak amplitudes of signal spectra may not be correctly displayed in the spectrum, because the discretization of the frequency axis according to eq. 5.2.3 is not fine enough to resolve these bins. Consider for example a signal

$$x(t) = \sin(2\pi\nu_1 t) + \cos(2\pi\nu_2 t) \quad (5.11)$$

with  $\nu_1 = 100$  Hz and  $\nu_2 = 202.5$  Hz. If this signal is discretized at an interval  $\Delta t = 1$  ms and the total length of the time record is  $N\Delta t \cdot t = 1$  s, the DFT bins will be spaced by  $1/t = 1$  Hz. The spectrum is shown in the upper graph of fig. 5.11 and

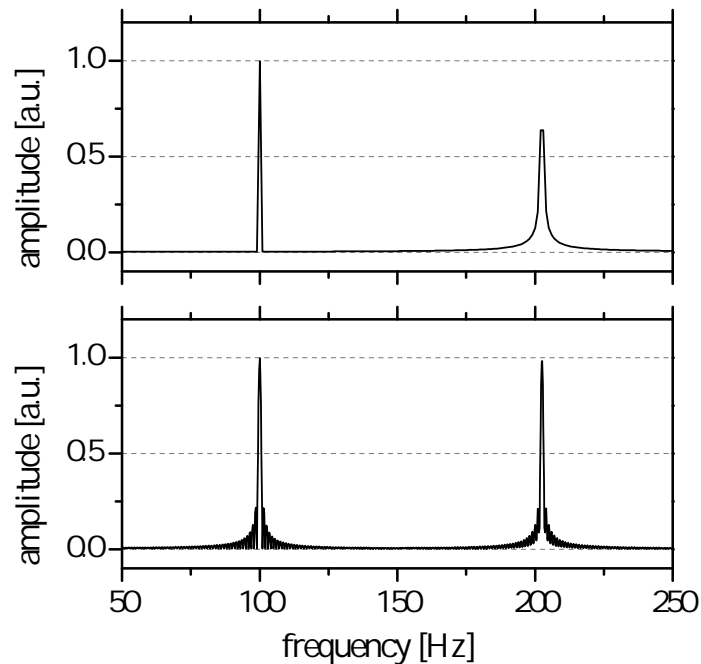


Fig. 5.11. – Effect of zero padding on the spectrum

it can be seen directly that the peak at  $\nu_2$  is not displayed correctly. Both peaks at  $\nu_1$  and  $\nu_2$  should have the same amplitude of 1. This is because the amplitude of  $\nu_2$  falls exactly into the middle between two frequency bins. In order to retrieve the  $\nu_2$  peak, the signal length  $N\Delta t$  has to be increased. Usually, there are only limited chances to simply record a longer signal, but if the power contained in the signal is of interest the time record can be increased by appending a series of zeros without adding any new information. The effect of this zeropadding is shown in the lower graph of fig. 5.11. The resolution of the frequency axis was increased by a factor 5 by appending  $4N$  zeros to  $x(t)$  and the peak at  $\nu_2$  is now displayed with its real amplitude.

## 5.2.4 Window functions

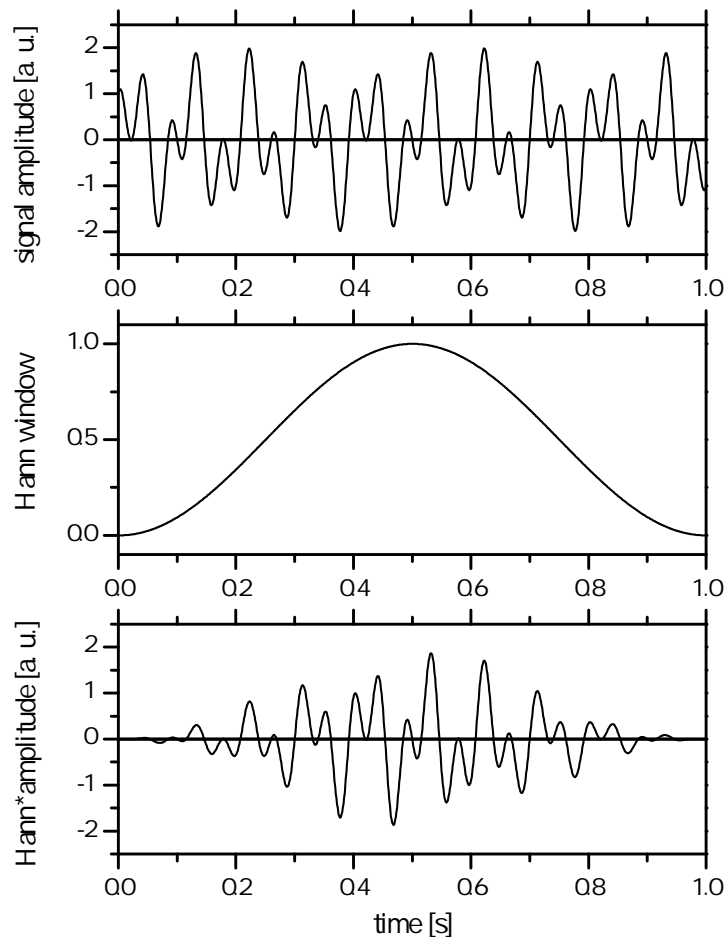


Fig. 5.12. – Effect of the Hann window function

An intrinsic property of the DFT is that its coefficients are periodic in  $N$ , i. e.  $\tilde{f}_{n+N} = \tilde{f}_n$  and likewise for the inverse DFT  $f_{j+N} = f_j$ . This means, that the DFT algorithm is fed with  $N$  repetitions of the signal appended to each other. In general, the time record does not contain full periods of all harmonics and so there will

be discontinuities appearing at the ends of each time record length. Such steps produce a broad range of harmonics, that add noise to the spectrum of the signal. Strictly speaking, any finite length time record corresponds to the infinitely long time domain signal convoluted by a rectangular window function of length  $t$ . However, a proper window function can be used to smooth out the discontinuities and hence provide a means to reveal the true noise level of the signal. In the following, the Hann (or Hanning) window will be discussed as an example in more detail. Other common window functions are the Hamming, Blackman and flat-top windows. A collection of window functions is listed in ref. [140].

The function for the Hann window is given by

$$w(t_j) = \frac{1}{2} \left[ 1 - \cos \left( 2\pi \frac{1}{(N-1)\Delta t} t_j \right) \right]; \quad t_j = j\Delta t, \quad j = 0 \dots N-1 \quad (5.12)$$

The effect of the Hann window on the time record is shown in fig. 5.12. The values at the beginning and at the end of the time record get damped, when the window function is applied. The windowed signal  $x'(t_j) = x(t_j) * w(t_j)$  is shown in the lowest graph of fig. 5.12 and will have smooth transitions when the data segment is repeatedly plotted. The resulting spectrum of  $x'(t_j)$  (see lower graph in fig. 5.13) has a considerably lower noise level compared to the spectrum of  $x(t_j)$ . Because the

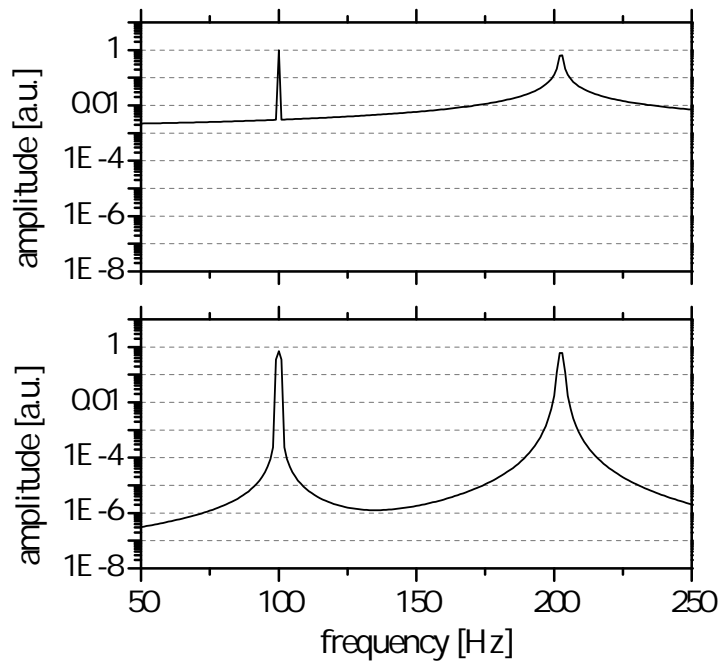


Fig. 5.13. – Effect of windowing on the spectrum. Top: Spectrum without prior application of the window function, bottom: Spectrum with the window function applied to the time domain signal. The additional noise originating from the steps in the time domain signal between repetition of data set to be analyzed is removed by the window function.

window function modifies the weighting of the samples in the original time record



(samples on the edges get damped), the normalization factor  $1/N$  in eq. 5.2.1 of the DFT is not valid anymore.

In reference [140] a sum is defined, which allows a quantitatively correct calculation of the power spectral density (PSD) in  $V^2/\text{Hz}$ :

$$\Xi = \sum_{j=0}^{N-1} w(t_j)^2 \quad (5.13)$$

$$\text{PSD}(\omega_n) = \frac{2 \cdot |\tilde{f}_n(\omega_n)|^2}{F_S \cdot \Xi} \quad \text{with} \quad \omega_n = 2\pi\nu_n \quad (5.14)$$

## 5.2.5 Aliasing

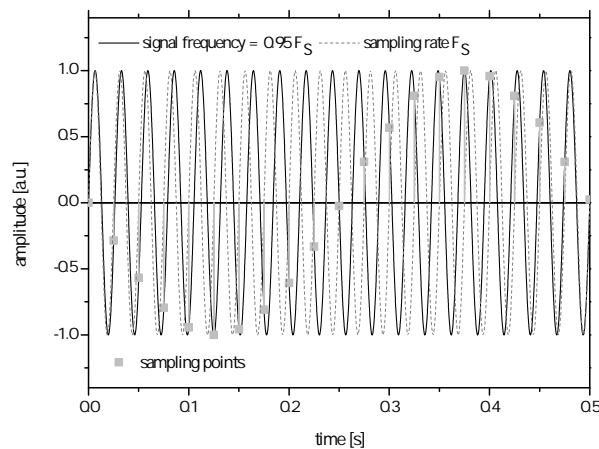


Fig. 5.14. – The aliasing phenomenon: If a signal should be sampled with a frequency  $\nu_S$  the signal itself must not contain any frequency components higher than  $\nu_S/2$ . Otherwise, these high frequency components are mistakenly sampled and cause unwanted artifacts (gray squares) in the digitized signal. Therefore, an analog low pass-filter is usually applied before sampling.

In sec. 5.2.3 the Shannon theorem was defined in eq. 5.2.3, that gives an upper limit for the maximum frequency that can be calculated by the DFT at a given sample rate. However, if the signal does contain components of frequencies higher than  $\nu_S/2$ , they will not be properly sampled and their contribution will occur at lower frequencies in the spectrum. This is called aliasing and can be prevented by low-pass filtering the signal before sampling. Fig. 5.14 shows the phenomenon for a signal with a frequency  $\nu_{\text{signal}} = 38 \text{ Hz}$  that is 95% of the used sampling frequency  $\nu_S = 40 \text{ Hz}$ . In gray, the sampling points are depicted, which are located on the sampled signal (solid line) at the zero-crossings of the sampling rate signal (dashed line). The gray points form a signal at the beating frequency  $\nu = \nu_S - \nu_{\text{signal}} = 2 \text{ Hz}$ .

## 5.3 Measurement Setup

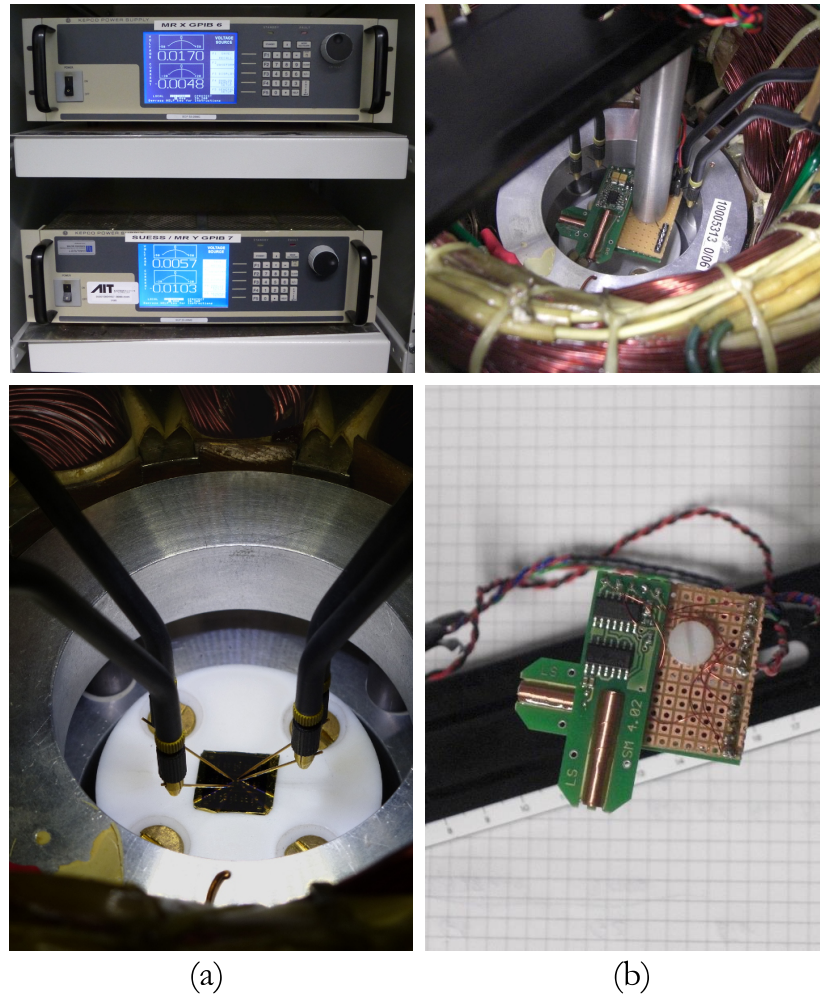


Fig. 5.15. – (a) Tip probe setup with electromagnet driven by a KEPCO current/voltage source for the application of magnetic fields between -80 and +80 mT. (b) Setup with commercial fluxgate sensor FLC100 [141] to test the the minimum field resolution

In this section, the measurement setup is described which is used to characterize the magnetic multilayers and test the TMR fluxgate sensors, which were fabricated by the process described in Sec. 5.1.5. First, the magnetic (Sec. 5.3.1) and electrical (Sec. 5.3.2) properties of the MTJs were characterized using a 4-probe measurement configuration. For the measurements in the TMR fluxgate operation mode with an alternating current passing through the current line for the generation of the switching field two probes were used for the top and backside contacts and two probes were used for contacting the current line.

Fig. 5.15 a) shows the tip probe setup with the surrounding electromagnet, that is driven by two separate bipolar power supplies (KEPCO Bipolar Operational Power Supply/Amplifier, BOP 20-10M with  $\pm 20$  V max. output voltage at max.  $\pm 10$  A). With the electromagnet, magnetic fields of up to  $\pm 80$  mT can be generated in the sample

plane. The setup is operated with a LabView program, which allows to perform field sweeps by controlling the KEPCOs via their GPIB interfaces. The field resolution of the setup was determined with a selfmade two-axis fluxgate magnetometer built with two commercially available fluxgate sensors - the FLC100 [141] (see Fig. 5.15 b)). The sensitive axes of the fluxgate sensors were aligned  $90^\circ$  to each other to measure the contributions of the currents in the electromagnet to the x- and y-fields separately. The sensors were mounted onto an aluminum rod using a PVC screw and suspended to the position of the sample. Then, the field value was increased in the programm in steps of  $1 \mu\text{T}$ . After an equilibration phase 20 subsequent values were measured and averaged. The results of this measurement are shown in Fig. 5.16. They show that the output current of the KEPCOs is effectively increased approx. after incrementing the software input value 6 times. From this we deduced that the field can be reliably increased when the field value in the software is at least changed by  $10 \mu\text{T}$ .

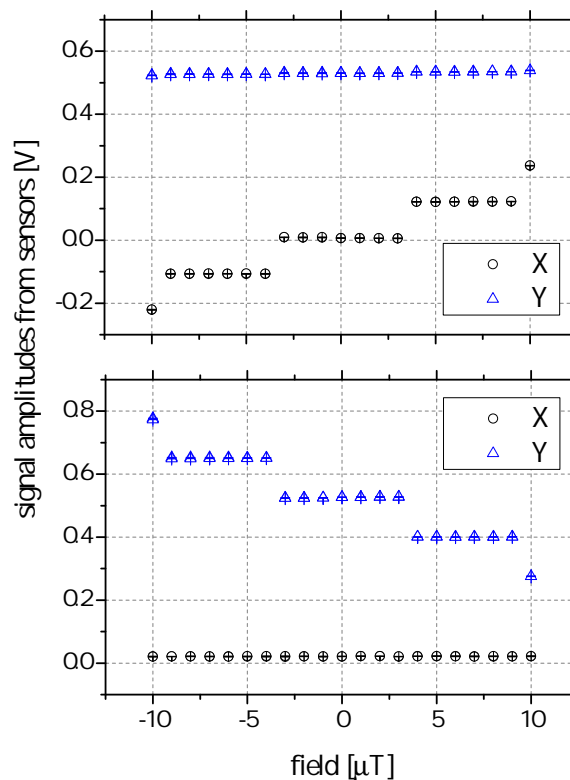


Fig. 5.16. – Measurement data from the self-built setup with two conventional fluxgate sensors [141] to define the minimum applicable field step.

### 5.3.1 Magnetoresistance measurements

The measurement setup described above was also used for two- and four-point measurements of patterned magnetic multilayers. A large number of magnetic

multilayers was fabricated by the methods described in sections 5.1 and 5.1.5 in order to find the multilayer design most suitable for application in a TMR fluxgate sensor. The most important criterion for selection was to have two stable magnetization states separated by a high TMR signal. Regarding the power that has to be applied to the current line the coercive field of the free layer should also be low. However, because the patterned MTJs used in the TMR fluxgates were relatively large (ellipses with dimensions  $a = 10 \mu\text{m}$  and  $b = 5 \mu\text{m}$ ) no significant constraint was expected here if CoFeB would be used for the free layer.

To meet the requirement of two stable magnetization states it is important to employ a mechanism that keeps the magnetization of one layer more rigid to an applied external magnetic field than the other. The “free layer” of the MTJ is supposed to rotate “freely” while the “fixed” layer’s magnetization should keep its orientation up to a certain field strength. This means, that the magnetization of the fixed layer either has a notably higher switching field or coercivity than the free layer ( $H_{C,\text{fixed}} \gg H_{C,\text{free}}$ ) or it is pinned by some physical mechanism, so that the switching loop gets biased to negative directions ( $H_{C,l,\text{fixed}} < H_{C,r,\text{fixed}} < H_{C,l,\text{free}} < H_{C,r,\text{free}}$ , indices l,r indicate left and right hand side coercivities, see Fig. 5.17). In the following, two common mechanisms employed in TMR and GMR sensors to pin the magnetization of one layer will be explained.

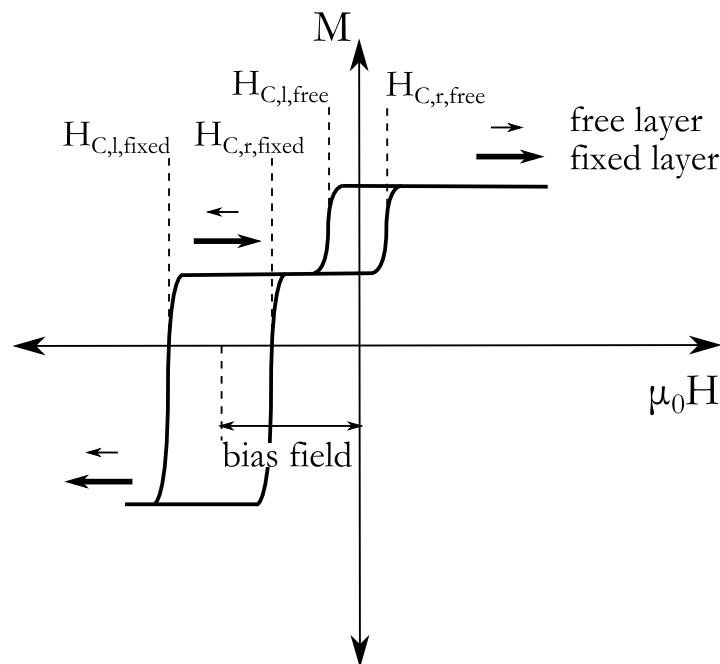


Fig. 5.17. – Illustration of a hysteresis loop of the free and the fixed layers’ magnetizations in a magnetic tunnel junction.

## Exchange Bias

The exchange bias effect is found in heterostructures composed of a ferromagnet (FM) and an antiferromagnet (AF) and manifests itself as an additional unidirectional anisotropy of the FM. This was first observed in 1956 by W. H. Meiklejohn and C. P. Bean [142] in a cobalt sample, where they identified the creation of antiferromagnetic cobalt oxide during annealing as the reason for a measured shift in the hysteresis loop with respect to zero field. They explained the microscopic origin of the effect by the interaction of the interfacial spins in the FM and the AF [143]. When the heterostructure is cooled down from a temperature above the ordering temperature of the AF  $T_N$  (Néel temperature) in an applied magnetic field  $H$ , the interfacial spins in the FM will align with the interfacial spins in the AF. This way the antiferromagnetic order provides an additional force to counteract the magnetization reversal which has its origin in the interfacial exchange. The Hamiltonian of the exchange biased FM can then be written as [144]

$$E = -HMt_F \cos \theta - J \cos \theta + K_F \sin^2 \theta. \quad (5.15)$$

Here the second term gives the energy originating from exchange bias with a coupling constant  $J > 0$ , i.e. an FM-type of interaction.  $H$  is the external field,  $M$  is the saturation magnetization,  $t_F$  is the thickness of the FM film,  $\theta$  is the angle of the applied external field with respect to the easy axis and  $K_F$  is the uniaxial anisotropy constant of the FM film.

The model provided by Meiklejohn and Bean is historically the first one to explain the exchange bias effect at perfectly flat interfaces with compensated AF spins. However, it yields exchange bias fields which are several orders of magnitude higher than the experimentally measured values. Further models have been developed, which can be categorized according to the interface properties (flat or rough) which are assumed and the compensation of the AF moments at the interface (uncompensated or compensated). The random-field model [145] assumes domain walls in the AF perpendicular to an interface with a random roughness profile. The AF domains have a small net magnetization along the magnetization direction in the FM, which causes the exchange bias coupling. Parallel domain walls are allowed in a model for uncompensated interfaces that assumes parallel spins in each AF layer, but allows spins in the neighboring layers to be tilted away from the direction of the first layer [146]. Similar results are obtained by assuming a polycrystalline AF, where in each AF grain partial domain walls are formed and the net moments of the domains couple to the FM [147]. It was possible to calculate realistic exchange bias fields for perfectly flat interfaces using a microscopic Heisenberg model, where single FM moments were replaced by AF moments [148]. Finally, the domain state model should be mentioned, which introduces non-magnetic defects into the AF (diluted AF) [149]. It is able to model a domain state of the whole AF layer (not only its

interface) that develops during a field cooling procedure. The magnitude of the exchange bias field can be explained by the degree of dilution of the AF layer.

### RKKY Coupling

Another effect which is used to achieve pinning of the magnetization in one of the layers in a MTJ is based on the fact, that localized magnetic moments in the unfilled inner shells of the atoms can interact over distances of several lattice constants by polarizing the conduction electrons. This interaction was described theoretically by M. A. Rudermann, C. Kittel, T. Kasuya and K. Yosida and hence named RKKY coupling [150–152]. It is an indirect interaction and its strength strongly depends on the distance from the polarizing magnetic moment. Its coupling constant can be expressed by [51]

$$J_{\text{RKKY}} \propto \frac{\cos(2k_{\text{F}}r)}{r^3}. \quad (5.16)$$

Here,  $k_{\text{F}}$  denotes the Fermi vector, which is related to the energy  $E_{\text{F}}$  of the electrons with effective mass  $m_{\text{eff}}$  at the Fermi level by  $E_{\text{F}} = \hbar^2 k_{\text{F}}^2 / 2m_{\text{eff}}$ . It should also be noted that  $J_{\text{RKKY}}$  has alternating signs oscillating with a wavelength of  $\pi/k_{\text{F}}$  and hence can be of ferro- as well as of antiferromagnetic nature. The observation of giant magnetoresistance in Fe-Cr-Fe sandwiches due to antiferromagnetic RKKY coupling in 1988 by the groups of A. Fert [153] and P. Grünberg [154] led to a technology breakthrough in hard disk industry and was awarded with the Nobel Prize for Physics in 2007. RKKY coupling depends very sensitively on the thickness of the non-magnetic spacer layer between the two ferromagnetic layers of only several Ångström and is also often referred to as interlayer exchange coupling.

In Fig. 5.18 magnetoresistance measurements on a top-pinned MTJ with CoFeB electrodes with the layer sequence (material and film thickness in nm)

$$\text{Ta5/Ru40/Ta5/CoFeB2.5/MgO2/CoFeB4/Ru1/CoFe2/IrMn15/Ru30/Au40}$$

are presented. The alloyed materials have compositions in atomic %

$$\text{CoFeB} \equiv \text{Co}_{40}\text{Fe}_{40}\text{B}_{20}, \text{CoFe} \equiv \text{Co}_{50}\text{Fe}_{50} \text{ and } \text{IrMn} \equiv \text{Ir}_{20}\text{Mn}_{80}.$$

The measurements were taken at 10 mV bias voltage after a field cooling procedure (30 min. annealing at 350°C and cooling down in a field of 220 mT) was applied. The field cooling establishes exchange bias between the IrMn and the CoFe layers, where the latter is coupled further to one CoFeB electrode of the MTJ via the RKKY coupling over the Ru spacer layer. The layers CoFe-Ru-CoFeB constitute a system of two antiferromagnetically coupled layers, which is also called a synthetic antiferromagnet (SAF). The intent was to reproduce the multilayer fabricated at the University of Bielefeld, which was used in the first TMR fluxgate structure presented in Ref. [86].

The initially sputtered sample (Fig. 5.18 a)) showed promising properties such as the highest TMR measured with the available sputtering and annealing facilities and satisfactory pinning of the magnetization in the upper CoFeB layer, which is manifested in a plateau at high TMR values for positive fields. However, the kink at about  $-40$  mT is an undesired feature, which can be explained by insufficient exchange bias between the CoFe and the IrMn layers. When the field is decreased to higher negative values the magnetization of the CoFe layer is rotated out of its easy axis alignment which also exerts a torque on the magnetization of the pinned CoFeB electrode due to the interlayer exchange coupling. The rotation away from parallel alignment with respect to the magnetization in the free layer is detected by an increase in the TMR signal. When the field is strong enough to overcome the interlayer exchange energy all magnetizations point along the field direction and the TMR signal goes back to its lowest value. Fig. 5.18 b) shows another sample where

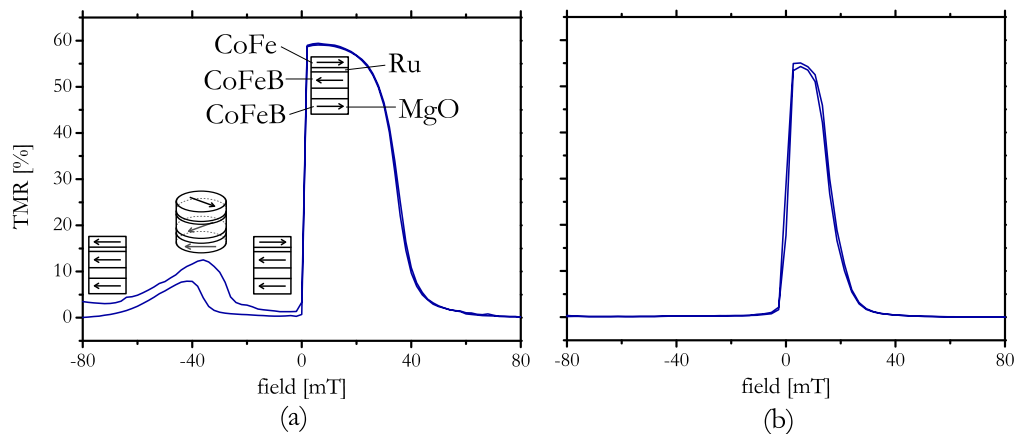


Fig. 5.18. – Top-pinned MTJ with synthetic antiferromagnet (SAF) with zero net magnetic moment: Ta5/Ru40/Ta5/CoFeB2.5/MgO2/CoFeB4/Ru1/CoFe2/IrMn15/Ru30/Au40, annealed 30 min. in a field of 220 mT. (a) highest TMR achieved of 60%, insufficient exchange bias between IrMn and CoFe causes the kink in the TMR signal. (b) no visible kinks in the TMR, but low exchange bias, possibly no coupling of the SAF

only a very weak interlayer exchange coupling is present that only exists around zero field. Exchange bias is not developed at all, and there is evidence that in top-pinned multilayers it is harder in general to achieve exchange bias than in bottom-pinned multilayers [155, 156]. The development of exchange bias at an AF/FM interface is suspected to strongly depend on the microstructure, which then determines the number of interfacial uncompensated spins [155]. These uncompensated spins couple to the spins in the FM layer and do not rotate in an external field, because they are locked to the AF lattice [157]. Hence, they provide the exchange bias field, that acts unidirectionally on the FM magnetization. In a polycrystalline film multiple parameters like grain size, roughness and defects act together that make it a big challenge to engineer a magnetic multilayer with particular properties [155, 158].

More reliable results regarding exchange bias and hence good pinning of one

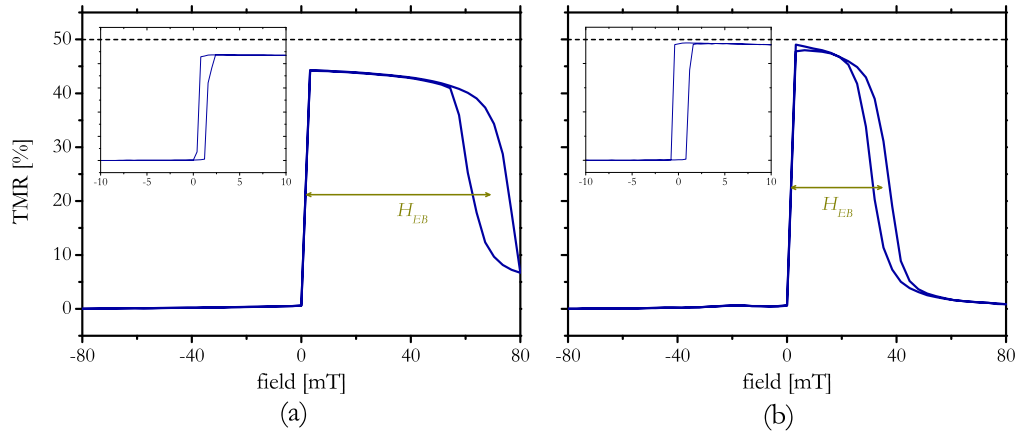


Fig. 5.19. – Comparison of two bottom-pinned MTJs with (a) 2 nm CoFeB on 2 nm CoFe and (b) 3 nm CoFeB only as fixed electrodes. The magnetization is pinned due to exchange bias to antiferromagnetic IrMn.

magnetization could be achieved with a bottom-pinned magnetic multilayer. The layer sequences were

Ta5/Ru40/IrMn15/(a) CoFe2/CoFeB2, (b) CoFeB3/MgO2/CoFeB6/Ta2/Ru10

for the magnetoresistance measurements presented in Fig. 5.19. The pinned electrodes in the samples have approximately the same total magnetic moment as  $M_{\text{CoFe}} \approx 2 \times M_{\text{CoFeB}}$  ( $M_{\text{S,CoFeB}} = 1.3 \text{ T}$  [159],  $M_{\text{S,CoFe}} = 2.4 \text{ T}$  [160]), so the stray field acting on the free electrode is the same in both samples. The system IrMn/CoFe was shown e.g. by Fernandez-Outon et al. [161] to exhibit large exchange bias and also in our case provides the largest measured exchange bias field  $H_{EB} \approx 70 \text{ mT}$ . This value cannot be determined accurately with the measurement setup because it was not possible with the available field strengths to fully reverse the pinned layer. The measurement and annealing conditions were the same as for the samples presented in Fig. 5.18, but the bottom-pinned layer showed a lower TMR ratio of  $\approx 50\%$ . Therefore the CoFe2/CoFeB2 electrode was replaced by a single 3 nm CoFeB layer with the expectation that this would increase the TMR ratio if the CoFe in the bottom electrode had induced the wrong texture to the CoFeB during annealing. In order to achieve high TMR ratios of  $> 100\%$  crystalline electrodes and a crystalline MgO barrier with (100) texture is required (see also Sec. 2.4.3). However, as shown by the measurement in Fig. 5.19 b) the TMR ratio did not change significantly compared to Fig. 5.19 a) and  $H_{EB}$  dropped to  $\approx 40 \text{ mT}$ . For example You et al. [156] found high exchange bias for a CoFeB/IrMn interface in a CPP-GMR spin valve, and this was attributed to the growth of (111)-textured IrMn on amorphous CoFeB. However, Kerr et al. [155] argued in their work that (111)-textured IrMn is not a necessary prerequisite for exchange bias. In their case of bottom-pinned spin valves



they showed that the magnetic field strength applied during the field cooling has a great influence on the exchange bias. Because in our case no structural data were available and the field could not be varied, no attempt was made by us to investigate these issues in more depth. The multilayer from Fig. 5.19 a) was chosen in the end as the best candidate for application as a TMR fluxgate sensors. This multilayer provided

- the largest exchange bias and hence good switching,
- relatively low electrical resistances (10 – 100k $\Omega$ ),
- and a high and reproducible TMR ratio.

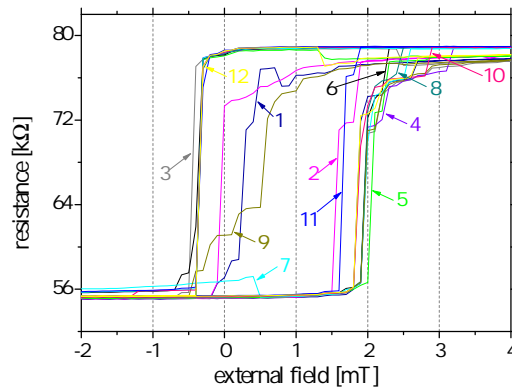


Fig. 5.20. – 12 consecutively measured easy axis magnetoresistance curves taken from the same MTJ.

In Fig. 5.20 12 subsequent field sweep measurements on a single patterned MTJ (ellipse with  $a = 10 \mu\text{m}$  and  $b = 5 \mu\text{m}$ ) are presented at very low sweep rates. The field was increased in steps of  $10 \mu\text{T}$  and held at a certain field value for 2 s. The resistance measurements were made 1 s after the desired field value was reached. The setup was operated by a LabView program which obtained the measurement data via the GPIB bus of the devices. The timing was chosen in a way to ensure that the field value was increased before the TMR was measured. It is remarkable that carrying out the same measurement on the exact same sample produces such a variation in the shape of the magnetoresistance curves. The numbers indicate the order in which the loops were measured. Loops 4, 6, 8 and 10 all start at the lowest and reach the maximum resistance for positive fields. The kinks originate from Barkhausen jumps of domain walls when they are released from pinning sites. The (spatial) sizes  $s$  of the jumps that correspond to the volume of magnetic material reversed during one jump and which are represented as sudden resistance changes in the MR loop, are expected to follow a power law distribution  $P(s) \propto s^{-\tau}$  where  $\tau$  is a critical exponent [162, 163]. The distributions depend on the field sweep rate as well as on the demagnetizing factor [164]. The theory, that domains in

magnetic thin film are a representation of a general physical phenomenon called criticality is further supported by magneto-optical experiments on polycrystalline Co [162] and on nanogranular CoCr(Pt) films, where it is shown that the domain walls move in a random-walk manner across the sample. Recently, also a theoretical work on Barkhausen jumps in thin films with uniaxial in-plane anisotropy was published [165], in which former models [163] are extended that were used for comparison to experimental data from bulk samples.

### 5.3.2 I-V measurements

Current vs. voltage measurements are a general means to characterize thin film and other complex electronic devices. I-V characteristics contain information about the electrical transport properties and using appropriate theoretical models material parameters can be extracted in order to optimize the performance of the device. Fig. 5.21 shows the TMR and the voltage versus the applied bias current of three different patterned magnetic tunnel junctions of the same multilayer:



The TMR is known to decay with increased bias current (or voltage) due to the hot electrons with energies above the Fermi energy. These electrons scatter at the interface of the ferromagnet with the tunnel barrier and excite magnons (magnetization fluctuations) that cause a quenching of the TMR ratio [166]. The shapes of the I-V curves in Fig. 5.21 b) for parallel (P) and antiparallel (AP) alignment deviate from a purely ohmic characteristic (i.e. a linear relation between current and voltage) to a degree which is related to the amount of coherent tunneling in the MTJ and hence a higher TMR. It is found in [167] that the TMR is higher for those junctions where the I-V characteristic in the P state is closer to ohmic behavior than in the AP state. This is because the dominant states for coherent tunneling in a CoFeB-MgO-CoFeB MTJ - the  $\Delta_1$  majority and the  $\Delta_2$  minority spin bands - alleviate the non-ohmic characteristics of incoherent tunneling up to a certain voltage. The data presented here qualitatively go in hand with the findings in [167]: The I-Vs for the parallel states are more linear than for the AP states and the sample with the least ohmic characteristic for both states also has the lowest TMR ratio. In Fig. 5.22 the differential conductances  $G = dI/dV$  of the same MTJs as presented in Fig. 5.21 are plotted. Because the conductance is a measure of the current transmitted through the tunnel barrier a physical model for describing the conductance with respect to bias voltage must include all relevant barrier parameters. Brinkman et al. [168] developed a model for the conductance based on the Wenzel-Kramers-Brillouin approximation for the solution of the 1D Schrödinger Equation for electron plane waves. It yields

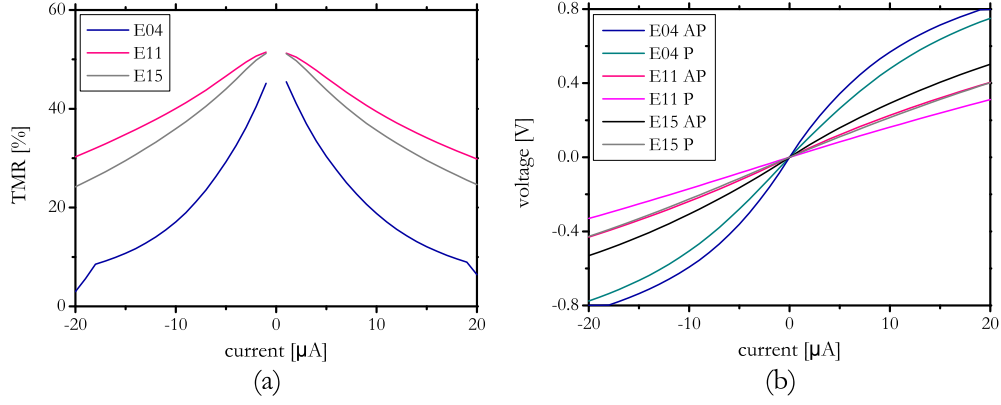


Fig. 5.21. – Data from three different MTJ elements on the same sample: (a) TMR ratio vs bias current, (b) MTJ voltage vs bias current. Pronounced deviations from ohmic behavior of the I-V characteristics correlate with a high portion of incoherent tunneling and hence reduced TMR [167].

the following relation for the differential conductance as function of the voltage  $V$ :

$$G(V) = G(0)A \left[ 1 - \left( \frac{A_0 \Delta \Phi}{16 \Phi^{3/2}} \right) eV + \left( \frac{9}{128} \frac{A_0^2}{\Phi} \right) (eV)^2 \right]. \quad (5.17)$$

Here,  $A$  denotes the junction cross sectional area,  $\Phi$  is the mean barrier height,  $\Delta \Phi$  is the barrier asymmetry  $A_0 = 4\sqrt{2}m_{\text{eff}}d/3\hbar$  with  $m_{\text{eff}}$  being the effective electron mass,  $e = 1.6 \cdot 10^{-19}$  C is the elementary charge and  $d$  the barrier width. The prefactor  $G(0)$  is given by  $3.16 \cdot 10^{10} \sqrt{\Phi}/d \exp(-1.025d\sqrt{\Phi})$  [168]. To fit the data in Fig. 5.22 the factors in Eq. 5.17 were rearranged to obtain a function  $G(V)$  with  $A$ ,  $d$ ,  $\Phi$ ,  $\Delta \Phi$  and  $\alpha = m_{\text{eff}}/m_e$  (ratio of the effective mass to the mass of the free electron  $m_e$ ) as the free parameters:

$$G(V) = A \cdot 10^{-8} \cdot 3.16 \cdot 10^{10} \sqrt{\frac{\alpha \Phi}{d}} \exp(-1.025\sqrt{\alpha \Phi}d) \times \left[ 1 - 2V \cdot 0.0213 \frac{\sqrt{\alpha}d\Delta \Phi}{\Phi^{3/2}} + 3V^2 \cdot 0.01094 \frac{\alpha d^2}{\Phi} \right] \quad (5.18)$$

The data from the fittings shown in Table 5.5 show that the element E04, which has the lowest conductance and also the lowest TMR as seen in Fig. 5.21, possesses the largest value for the effective barrier thickness  $d$ . The effective thickness of 19Å derived from the fitting procedure is close to the nominal barrier thickness of 20Å (2 nm). The barrier asymmetry  $\Delta \Phi$  is lowest in this junction element, whereas the mean barrier height  $\Phi$  is between the values of the other two junctions with higher conductivities. These values are the result of complicated processes at the interfaces during annealing and cannot be explained with the work functions of the materials alone [169]. Local defects as well as asymmetric oxidation of the interfaces play a crucial role for the barrier properties [170, 171].

It should be noted that the Brinkman model from Eq. 5.18 is an oversimplification

of the tunneling process that is taking place in a crystalline MgO barrier. As it was discussed in Sec. 2.4.3 spin-dependent tunneling through an MgO barrier is mediated by the  $\Delta_1$  Bloch states for parallel alignment of the magnetizations and by the  $\Delta_5$  states for antiparallel alignment. Because of this, the barrier parameters for parallel and antiparallel alignment should differ from each other. The barrier values and asymmetries reported here are higher than those reported in the literature, e. g. in Refs. [70, 172] despite comparable MgO barrier thickness. Also, the TMR is lower and the resistance-area product is higher for the MTJs fabricated within the scope of this work. This can be attributed to the incorporation of impurities in the MgO barrier or at its interfaces to the FM electrodes [170]. The sputtering device was not used exclusively for the fabrication of MTJs, so despite thorough cleaning by presputtering all targets after the chamber had been opened for target change, this is a likely explanation for the achieved TMR ratios and the large variance of the barrier parameters within the same sample (see Table 5.5). However, in a recent publication [173] it was pointed out that the intuitively plausible argument of more defects leading to lower TMR falls short of distinguishing among different types of defects, that might even promote coherent spin-dependent transport.

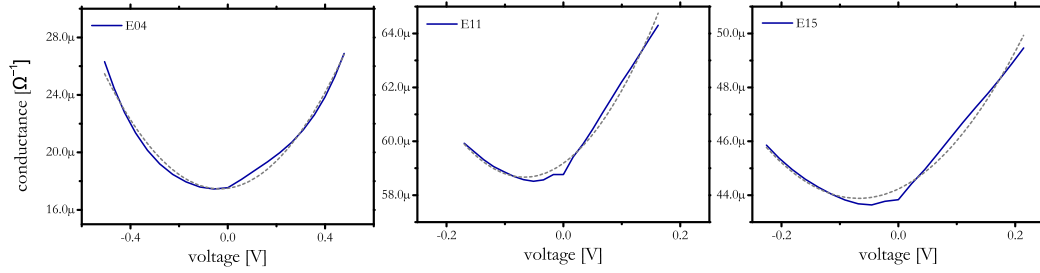


Fig. 5.22. – Conductances for the parallel state with fits using Eq. 5.18. The fit parameters are given in Table 5.5

element	$A$ [ $\mu\text{m}^2$ ]	$\alpha$	$\Phi$ [eV]	$\Delta\Phi$ [eV]	$d$ [ $\text{\AA}$ ]
E04	157	0.4	2.32	-0.94	19.0
E11	157	0.4	2.22	-1.77	18.2
E15	157	0.4	2.42	-1.83	17.8

Tab. 5.5. – Fit parameters for the Brinkman model of the MTJ conductance:  $A$  ... junction area,  $\alpha$  ... relative effective mass  $m_{\text{eff}}/m_e$  for the  $\Delta_1$  band electrons [68],  $\Phi$  ... mean tunnel barrier height,  $\Delta\Phi$  ... barrier asymmetry,  $d$  ... effective barrier thickness.

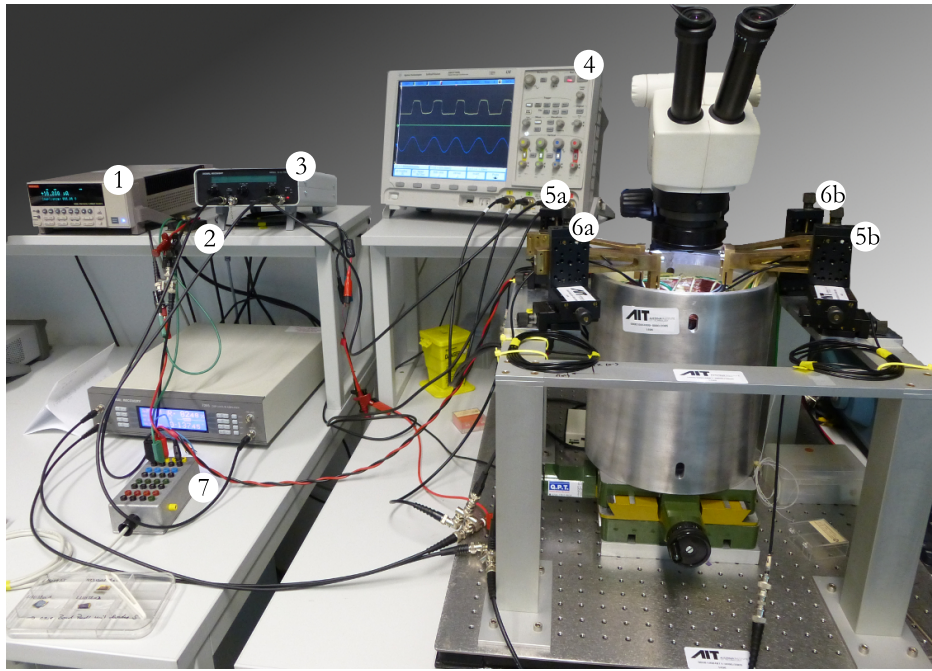


Fig. 5.23. – Measurement setup: 1 Keithley 6220 precision current source, 2 500 mΩ shunt resistor, 3 preamp with built-in low-pass filter, 4 Agilent Digital Signal 4-Channel GHz Oscilloscope, 5a+b probe contacts to current line, 6a+b probes to the top and backside contacts of the magnetic tunnel junction, 7 box with contacts to bypass the current through the current line

## 5.4 Fluxgate operation mode measurements

In Fig. 5.23 the measurement setup is shown to operate the MTJs in the fluxgate mode. Four tip probes are available to connect the bias voltage contacts and the current line which generates the driving field. Therefore, the MTJ voltage is measured in a two-point method, which only becomes a problem for low resistance devices. As the devices investigated in this thesis all had resistances in a range from 10 - 100 kΩ, the contact resistances could be considered negligible. The bias current to the MTJ is supplied using a Keithley 6220 precision current source and from the same tip probes two shielded cables are connected to the input of the preamplifier (Signal Recovery Model 5113 Low-Noise Voltage Prempplier). The preamp is operated in differential mode and a low pass filter with a cutoff frequency of 300 kHz (6 dB roll-off) is used to filter high-frequency noise. The output signal of the preamp is then fed to the oscilloscope or alternatively to the lock-in amplifier (LIA, Signal Recovery 7265 DSP). In the circuit scheme in Fig. 5.24 a) the voltmeter can represent both the scope's and the LIA's inputs. Additionally, the alternating current in the line patterned on top of the MTJ (see Sec. 5.1.5) is monitored via a shunt resistor of 500 mΩ with another scope channel. The current line circuit is given in Fig. 5.24 b). The current source for the driving current (not shown in Fig. 5.23) consists of an Agilent 33220A 20 MHz function generator and a constant current amplifier (Amp-Line Corp., ALC

Constant Current Source Model AL-50-CR-L/A with 50 W output power). A box providing the sockets to which the leads from the amplifier are plugged as well as the outgoing leads to the on-chip current line was constructed (number 7 in Fig. 5.23). The box also provided the possibility to plug and unplug a resistor in parallel to the current line circuit, so that a part of the current from the current source could be easily bypassed. This was needed especially when adjustments to the setup were made, so that there was a risk that the tip probes might accidentally lose contact to the sample. The sudden drop of the current and hence of the magnetic field it creates resulted in high induction voltages, which irreversibly damaged the device. It was found that a resistor of about the same resistance as the current line of  $5 \Omega$  was enough to prevent this from happening. Therefore, before each adjustment, the bypass resistor was plugged in and removed again, when the measurements were started. All data acquisition was realized using a LabView program to read out the scope and LIA data via their USB or GPIB interfaces.

In the following sections measurements will be presented on TMR fluxgate sensors that were carried out with the setup described here. First, dynamic magnetoresistance loops will be discussed, which are given by the time-domain MTJ voltage signals observed over several switching cycles. Second, the operation of the TMR fluxgate as intended for magnetic field measurements will be demonstrated by measuring the second harmonic voltage with the LIA.

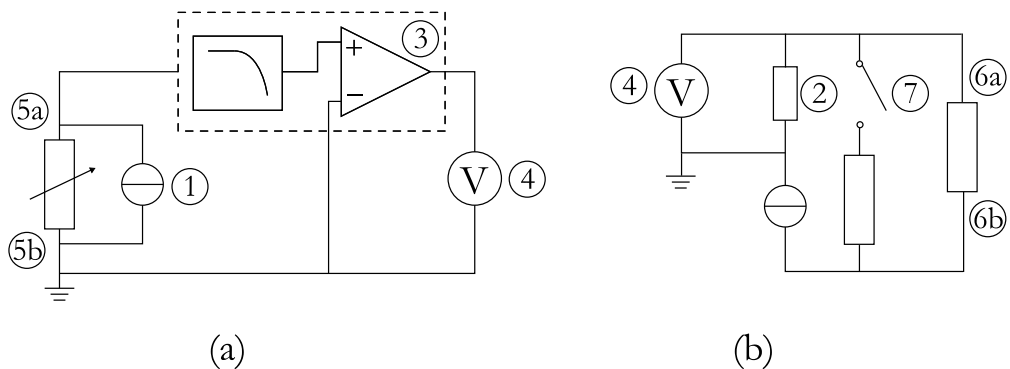


Fig. 5.24. – Circuit schemes for (a) the magnetic tunnel junction circuit and (b) the current line circuit

### 5.4.1 Dynamic magnetoresistance loops

In Figs. 5.25 and 5.26 dynamic magnetoresistance loops for varying switching frequencies are from 10 to 500 Hz are shown. Because of the sensor design, the MTJ is always switched along its easy axis. In Fig. 5.26 a bias field of 1 mT is applied along the hard axis. This has considerable influence on the shape and reproducibility of the switching of the free layer. As already shown in Fig. 5.20 where the external field was applied using the electromagnet from the tip probe setup

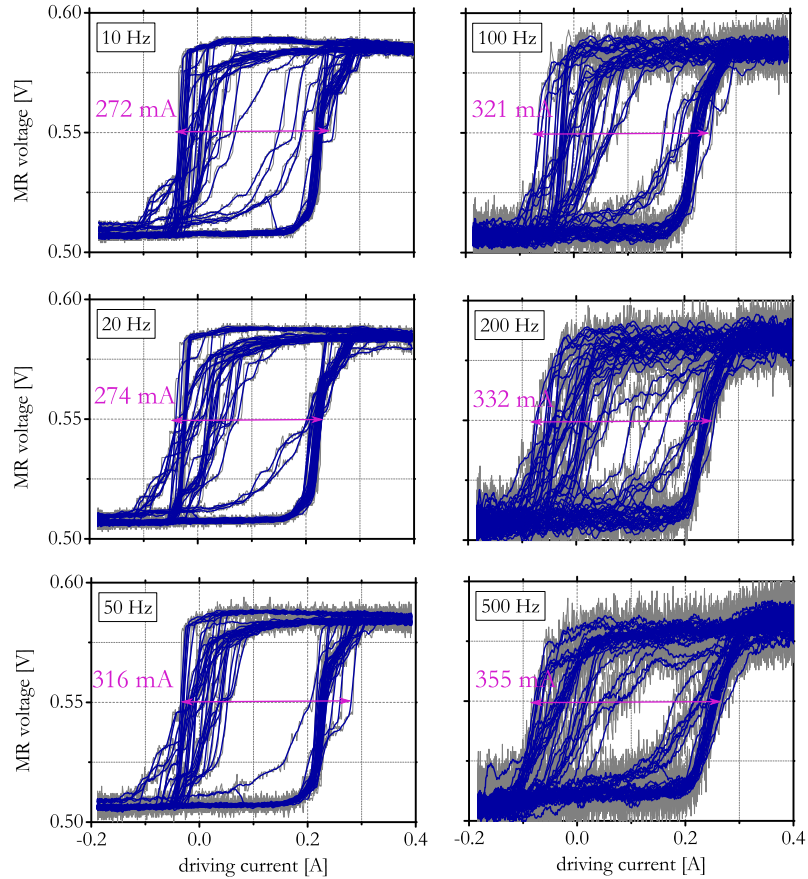


Fig. 5.25. – Dynamic magnetoresistance loops plotted as MTJ voltage over the current in the current line, that is measured via a shunt resistor. The gray signal is the unfiltered raw signal and each datapoint of the blue signal represents a 10 point average of the gray signal. No hard axis bias field is applied, and the field from the current line acts along the easy axis of the elliptical MTJ ( $a = 10 \mu\text{m}$  and  $b = 5 \mu\text{m}$ ). The bias current applied to the MTJ was  $10 \mu\text{A}$ .

(see Fig. 5.15), the switching along the easy axis exhibits variations during each switching cycle. Switching from the low resistance state (i.e. magnetizations in the free and pinned layer are parallel) shows less variation as compared to the opposite switching, where the field is decreased from the antiparallel state. Interestingly, some of the magnetization reversal paths disappear when the frequency of the alternating current that generates the periodic switching field is changed. This is most clearly seen when comparing the 20 Hz to the 50 Hz data. The chaotic switching behavior of micron-scaled magnetic elements ( $500 \times 3000 \times 5\text{nm}^3$ ) was recently modeled using a micromagnetic simulation at zero temperature [174]. Here, it is revealed that different residual domains are present depending on the field amplitude, when the particle is saturated along the hard axis. It should be noted, that the rate is kept constant and the element is always saturated, so the effect stems from the point from which the loop is run through. As the system investigated here differs in several points from the system discussed in Ref. [174] it can only be guessed to

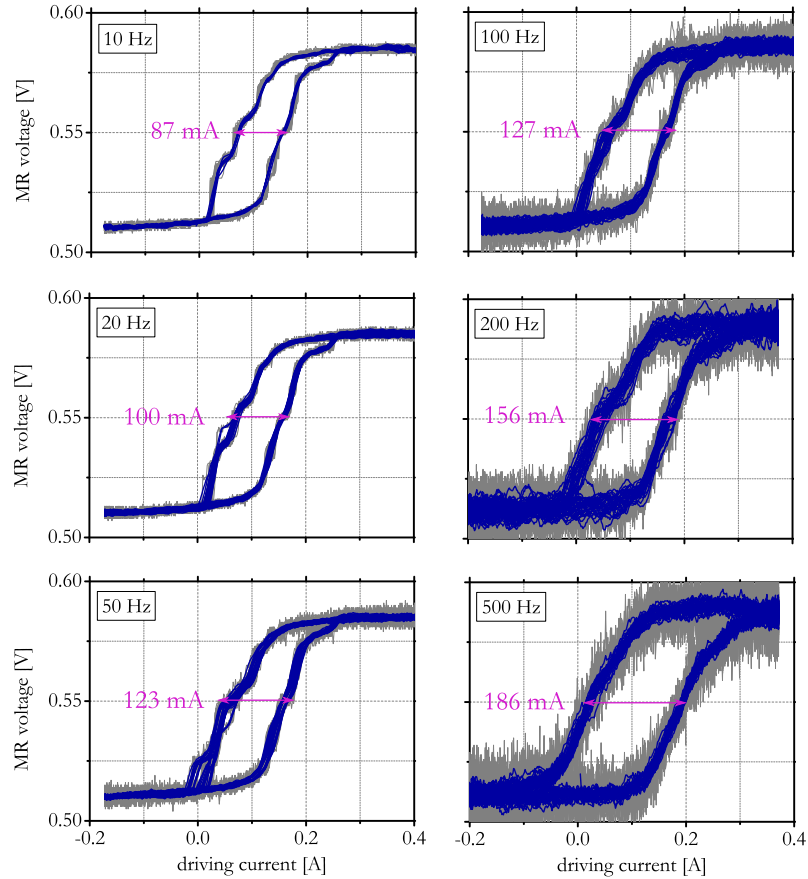


Fig. 5.26. – Same as Fig. 5.25, but with a bias field of 1 mT applied along the easy axis.

what extent the loops in Fig. 5.25 show signatures of deterministic chaotic behavior, that is modeled by the simulation. More detailed investigations using micromagnetic simulations and measurements of all parameters of the real system would be needed to come to a more conclusive explanation. Furthermore, it will also be important to include temperature into the simulation model in order to account for thermal activation.

The relevance of the temperature can be seen when comparing the hysteresis loop widths at different frequencies. As discussed in Sec. 4.2.1 the coercive field and hence the hysteresis loop width will increase with increasing field rate in the presence of thermal fluctuations. The widths of the hysteresis loops is given for each graph and was read from it by placing a data cursor at 0.55 V and at the outer edge of the loop as indicated by the arrows. The current values in Figs. 5.25 and 5.26 can be converted by using the coercivity from Fig. 5.20 ( $H_C \approx 1.2$  mT) and the width  $I_{cl} = 272$  mA of the 10-Hz-loop to compute a conversion factor  $c$  for the field generated by the current line

$$c = \frac{I_{cl}}{2H_C} = 113.3. \quad (5.19)$$



Using  $c$ , the currents from Figs. 5.25 and 5.26 can be converted to coercive fields, that depend on the field rate at which the loop is run through (see Fig. 5.27). It should be noted that additional statistics can be introduced by collecting several readings of the coercivities from each loop. The lines in Fig. 5.27 were drawn as a guide to the eye.

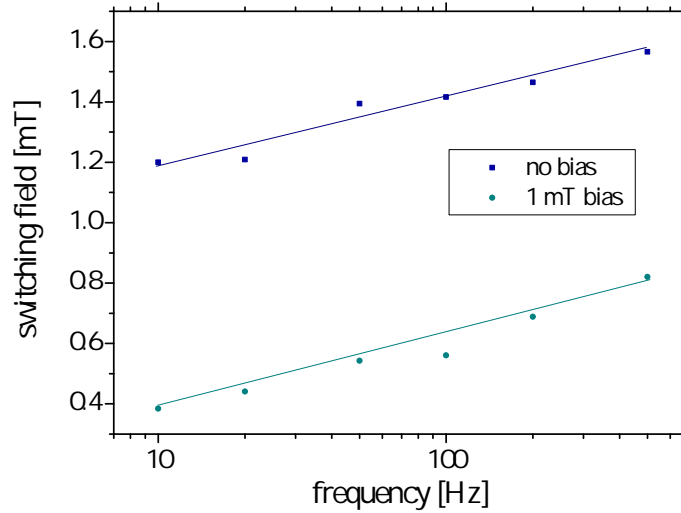


Fig. 5.27. – Dynamic coercivities as read from the loops in Figs. 5.25 and 5.26. The lines are a guide for the eye.

## 5.4.2 Sensor characteristics

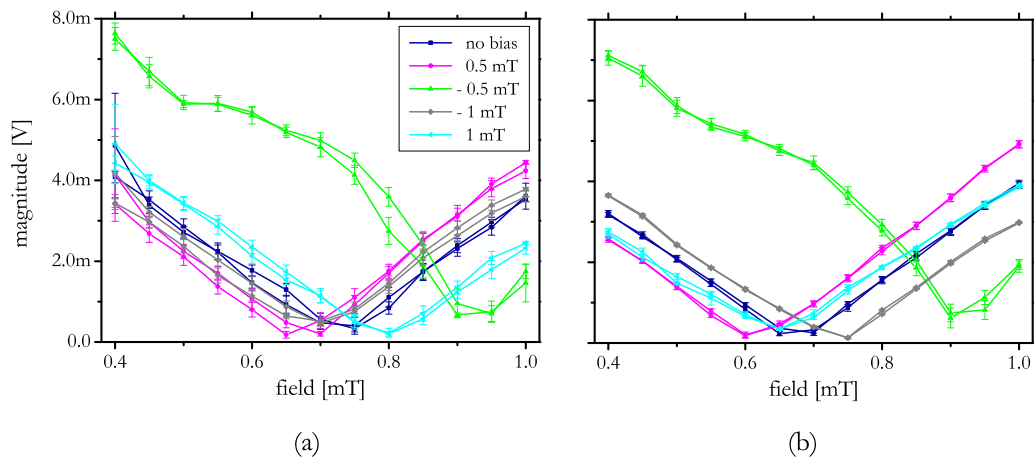


Fig. 5.28. – Sensor characteristics measured at switching frequencies of (a) 100 Hz and (b) 1 kHz

In Fig. 5.28 TMR fluxgate sensor characteristics are shown, where the second harmonic of the time domain signal was measured with a lock-in amplifier at switching frequencies of 100 Hz and 1 kHz. The magnetic field was increased in

steps of  $50\mu\text{T}$  and data were taken several seconds after the field value was set. The waiting time was at least twice the time constant  $T_C$  of the LIA, which also determines the equivalent noise bandwidth (ENBW) of the measurement. Depending on the roll-off rate  $\Delta L$  (in dB/decade or dB/octave (dB/8ve)) of the bandpass filter, which refers to the slope of the transfer function in the frequency domain (see also Eq. 5.2.2 in Sec. 5.2.2), we have [175]

$$\text{ENBW}_{\text{LIA}}(\Delta L = 6\text{dB}/8\text{ve}) = \frac{1}{4T_C}. \quad (5.20)$$

The sensor characteristics in Fig. 5.28 a) for a switching frequency of 100 Hz were obtained with a time constant  $T_C = 1$  s and for 1 kHz in Fig. 5.28 b) with  $T_C = 100$  ms. At each frequency, different hard axis bias fields ( $\pm 1$ ,  $\pm 0.5$  and 0 mT) were applied. As discussed before, a bias field significantly reduces the jitter in the time domain signal. Because the LIA works as a phase-sensitive detector, stable signal edges will be important for proper operation of the LIA. The most unstable signal is present at a bias field of  $-0.5$  mT, which is plausible from the raw scope data shown in Fig. 5.29. The time domain signal with a hard axis bias field of 1 mT has much more reproducible edges for both the 100 Hz and the 1 kHz signal.

The slopes of the sensor characteristics - i.e. the sensor sensitivities - at 100 Hz and

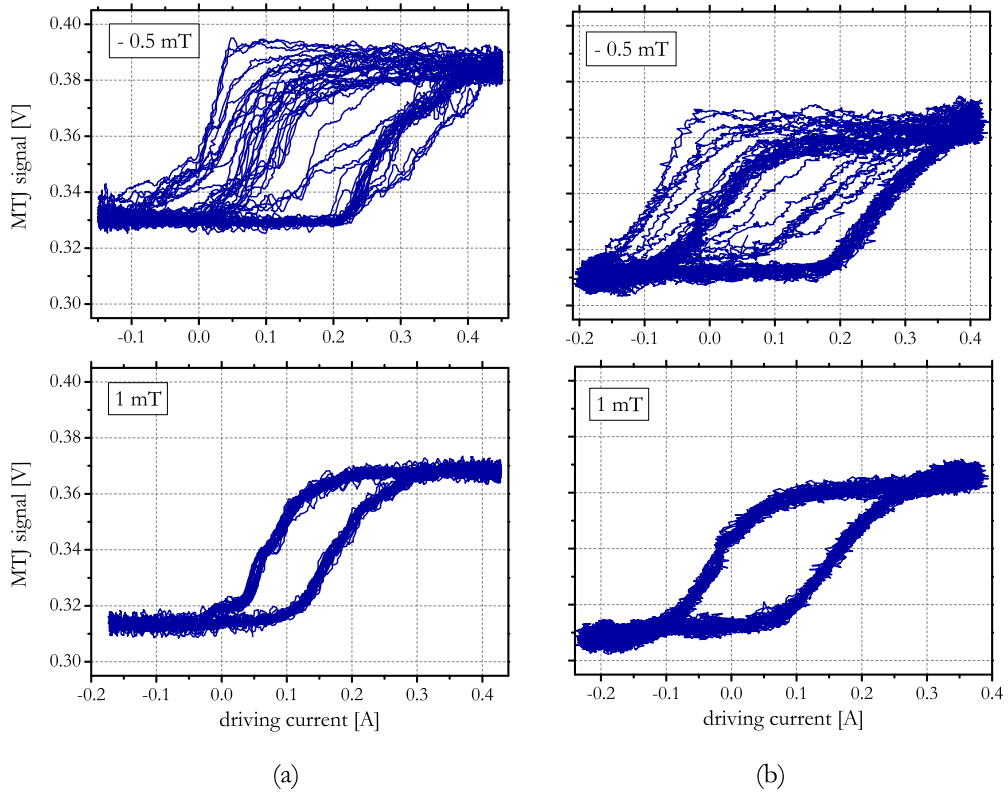


Fig. 5.29. – Time domain signals of the TMR fluxgate for (a) 100 Hz and (b) 1 kHz driving field frequency at  $-0.5$  mT and 1 mT hard axis bias, respectively

1 kHz do not significantly differ from each other. This is as expected, because the

frequency of the driving field does not occur in the analytical expression derived for the TMR fluxgate sensitivity  $(\Delta V_2/\Delta H_x)_{\text{analytical}} = (2/\pi)(\Delta V/H_0)$  (see Eq. 3.16), where  $\Delta V$  is the voltage difference originating from the TMR effect and  $H_0$  is the driving field amplitude of the field from the current line.

In Fig. 5.30 a) the real and imaginary parts of the second harmonic voltage are shown, which add up to the magnitude in Fig. 5.28 as

$$V_2 = \sqrt{\text{Re}(V_2)^2 + \text{Im}(V_2)^2}. \quad (5.21)$$

For 0 and 1 mT hard axis bias both the real and the imaginary part show very linear and hysteresis free behavior.  $\text{Re}(V_2)$  as well as  $\text{Im}(V_2)$  are both sensitive to whether the field is applied in the positive or negative direction. By “positive/negative” we refer to the fields to the “right/left” of the zero crossing of the characteristics. The fact that this is not the case at  $\mu_0 H_x = 0$  mT is due to the magnetic bias of the loop. When  $H_x$  reaches the size of the bias field the second harmonic becomes zero, which is the case at  $\approx 0.7$  mT for no hard axis bias. This is also clear from the static loop presented in Fig. 5.31 a).

The sensitivity of the sensor characteristics in Fig. 5.28 is

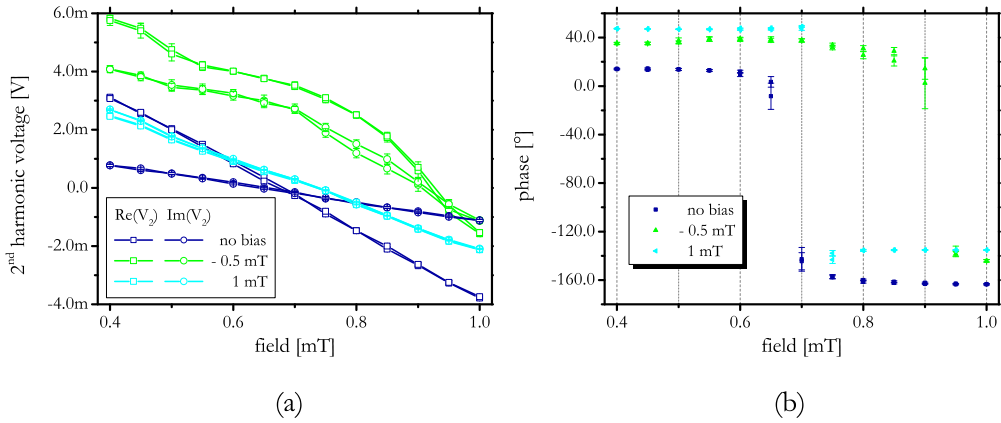


Fig. 5.30. – (a) Real (Re) and imaginary (Im) parts of the second harmonic voltage for -0.5, 0 and 1 mT hard axis bias. (b) Phase  $\phi = \frac{180}{\pi} \tan^{-1} \frac{\text{Im}(V_2)}{\text{Re}(V_2)}$  in degrees of the TMR fluxgate signal with respect to the LIA reference.

$$\frac{\Delta V_2}{\Delta H_x} = \frac{V_2(H_x = 0.4 \text{ mT}) - V_2(H_x = 0.5 \text{ mT})}{0.1 \text{ mT}} = \frac{1.22 \text{ mV}}{0.1 \text{ mT}} = 12.2 \text{ V/T}, \quad (5.22)$$

where  $V_2(H_x = 0.4 \text{ mT}) = 3.66 \text{ mV}$  and  $V_2(H_x = 0.5 \text{ mT}) = 2.44 \text{ mV}$  were read from the graph. For the analytical formula the driving field amplitude  $H_0$  has to be known. It can be estimated by noticing from Fig. 5.31 b) that the current range that covers twice the coercive field of the 100 Hz loop  $I_{c1} \approx 260 \text{ mA}$  corresponds to the

width of the hysteresis loop  $2 \times 1.3$  mT in Fig. 5.31 b). Hence, we have a conversion factor (see also Eq. 5.19)

$$c = \frac{260 \text{ mA}}{2 \cdot 1.3 \text{ mT}} = 100.$$

This leads to a driving field amplitude

$$\mu_0 H_0 = \frac{1}{2} \cdot \frac{I_{cl,0}}{c} \approx \frac{1}{2} \cdot \frac{600 \text{ mA}}{100} = 3 \text{ mT},$$

where  $I_{cl,0}$  denotes the current range during one switching cycle. The sensitivity according to the analytical expression from Eq. 3.16 amounts to

$$\frac{\Delta V_2}{\Delta H_x} = \frac{2}{\pi} \frac{60 \text{ mV}}{3 \text{ mT}} \approx 12.7 \text{ V/T}. \quad (5.23)$$

This is remarkably close to the measured sensitivity of 12.2 V/T, given the estimations made to derive the analytical result. It proves the validity of the step function approximation for the time domain TMR fluxgate signal and hence the derived sensitivity gives a valid model including relevant parameters for optimization. These are the magnetoresistive voltage change  $\Delta V$  and the driving field amplitude  $H_0$ , where the first parameter has to be as large as possible and the second as small as possible. However,  $H_0$  cannot be made arbitrarily small, because the MTJ has to be switched and hence  $H_0 > H_C$  is required. Therefore, a small coercive field  $H_C$  would be beneficial to the TMR fluxgate sensitivity. Optimizing  $\Delta V$  means to increase the TMR ratio, which can be achieved by optimizing the magnetic multilayer and also by minimization of the switching element. However, the minimization of the MTJ works against a small coercivity, so the two parameters are not completely independent from each other.

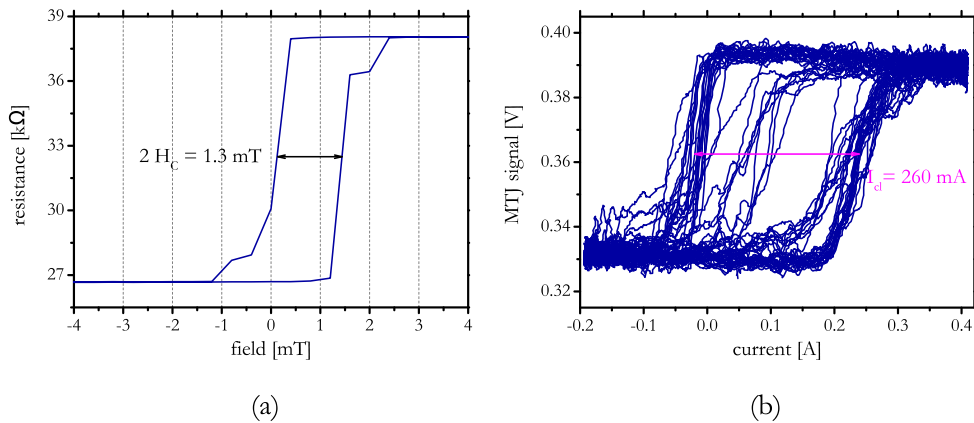


Fig. 5.31. – (a) static magnetoresistance loop measured without the current line in operation, (b) dynamic magnetoresistance loop measured at a driving field frequency of 100 Hz.

## Discussion of Results

In this section the experimentally obtained and the simulated results will be compared in order to determine a detection limit for the sensing principle. As described in Chapter 4 the fluctuations in the switching fields that are caused by thermal activation of the switching process lead to noise at frequencies in the vicinity of the second harmonic. Here, a detectivity (see Eq. 2.1) is derived based upon power spectral densities (PSDs) computed from measured and simulated time domain signals.

From the measurement data, two datasets with a switching frequency of 100 Hz

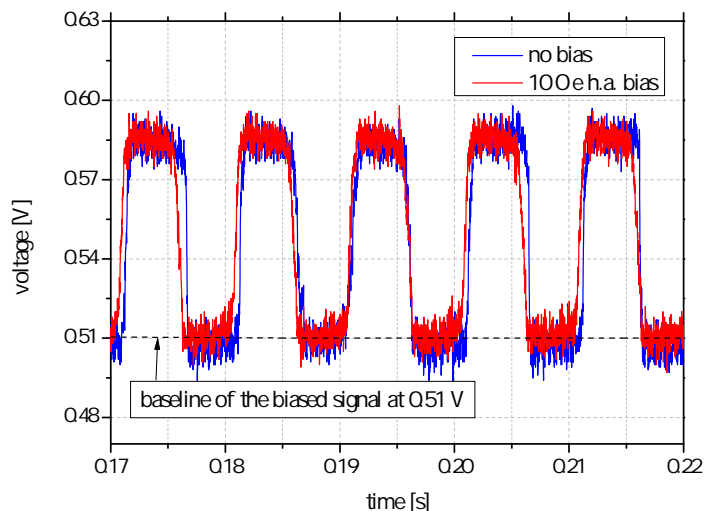


Fig. 6.1. – Raw time domain signals measured with the GHz oscilloscope at a sampling rate of 100 kHz.

were chosen (see Fig. 6.1) that represent different switching regimes. In one measurement an additional hard axis (h.a.) bias field of 1 mT is applied which leads to a more reproducible switching behavior than for the unbiased sensor (see also Sec. 5.4.1, where the signals are plotted with the time axis replaced by the external driving field). The signal from the biased sensor will be used to evaluate if the Monte Carlo simulation of the TMR fluxgate sensor signal can serve as a valid lower boundary for determining an ultimate detection limit for this sensing technology. In Fig. 6.2 the simulated signal is plotted together with the measurement for the biased sensor after applying a moving average filter with a window of 35 datapoints for better visibility. From the simulation a square wave-like signal is obtained, whereas the measured signal has notably less steep edges. In order to properly compare

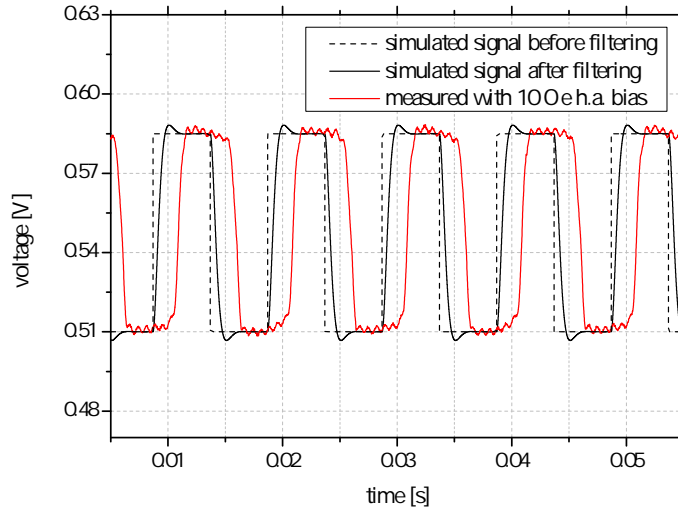


Fig. 6.2. – Low-pass filtered time domain representation of the simulated TMR fluxgate signal and the smoothed signal from the measurement with a 1 mT h.a. bias field applied.

the simulation to the measurement, it has to be assured that the edges of the two signals have the same slope at the transition from high to low. The slopes of the measurement data are determined by the oscilloscope’s anti-aliasing filter, so a digital filter needs to be found for the simulated signal, which models the behavior of the measurement setup. For the simulated TMR fluxgate signal the built-in Butterworth filter function from MATLAB<sup>®</sup> was used to model a second-order filter with a cutoff frequency of 1 kHz (see table 6.1). The exact cutoff frequency is not of great importance here, it should only be reasonably far away from the 200 Hz signal component where the noise floor will be determined.

After filtering, the Hann window function is applied to the time records, which have

	1	2	3
b	2.4619e-6	4.9239e-6	2.4619e-6
a	1.0000	-1.9956	0.9956

Tab. 6.1. – Coefficients for the second order Butterworth filter with a cutoff frequency of 1 kHz. They are used to compute the filter transfer function in the z-domain  $Y(z) = \frac{b(1)+b(2)z^{-1}+b(3)z^{-2}}{a(1)+a(2)z^{-1}+a(3)z^{-2}}$  (see also sec. 5.2).

each a length of 0.3 s. Then, the signal is zero-padded to a total length  $t_{\text{tot}}$  of 1 s in order to increase the frequency resolution to  $1/t_{\text{tot}} = 1$  Hz. The effects of these steps are described in detail in Sec. 5.2. The parameters used for the digital signal processing in MATLAB<sup>®</sup> are listed in table 6.2. In the next step, the power spectral

	simulation	measurement	
time record length [s]	0.3	0.3	input data
sampling frequency [Hz]	$10^6$	$10^5$	
thermal stability ratio	10000	-	
filter cutoff frequency [Hz]	1000	1000	filtering
applied window function	Hann	Hann	windowing
total signal length before FFT [s]	1	1	zeropadding
percentage of zeropadding [%]	70	70	

Tab. 6.2. – Parameters for the evaluation of the simulation and the measurement data.

density (PSD) is computed from measured and the low-pass filtered simulation signals according to eq. 5.14

$$\text{PSD}(f) = \frac{2 \cdot |\hat{x}(f)|^2}{F_S \cdot \Xi}$$

where  $\hat{x}(f)$  is the Fast Fourier-transformed input signal,  $F_S$  is the sampling frequency and  $\Xi$  is the modified normalization factor arising from the Hann window (see also sec. 5.2.4). The PSD is bandwidth-normalized, so the measurement and the simulation data can be compared to each other despite the different sampling rates of the time record. Fig. 6.3 shows the results in the frequency range of the lower

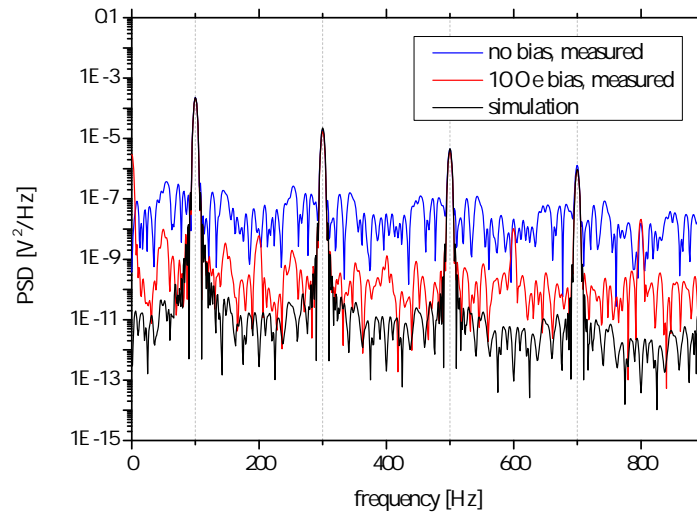


Fig. 6.3. – Comparison of the simulated to the measured PSDs. In one of the measurements a 1 mT hard axis bias field was applied.

harmonics of the 100 Hz TMR fluxgate signal. The PSD of the unbiased signal shows the highest noise level, which is due to the jitter caused by unreproducible switching behavior. This is further supported by the fact that applying a hard axis bias field reduces the noise floor of the PSD. Furthermore, it should be noted that the peaks at 100, 300, 500, ... Hz have the same values for all three data sets. This proves, that

the digital filtering applied in MATLAB<sup>®</sup> to the simulation data does not distort the amplitudes of the lower harmonics. Hence, no signal loss is expected in the second harmonic, which is the measure for an externally applied magnetic field.

The PSD of the simulated signal shows the lowest noise level, representing the ideal case where no other noise term than the noise originating from thermally activated switching is present. In the following section, the baseline value of this PSD will be used to compute a minimum field that can be detected by a TMR fluxgate sensor with a thermal stability given by the anisotropy parameters of the free layer in the magnetic tunnel junction.

## 6.1 Estimation of the detection limit

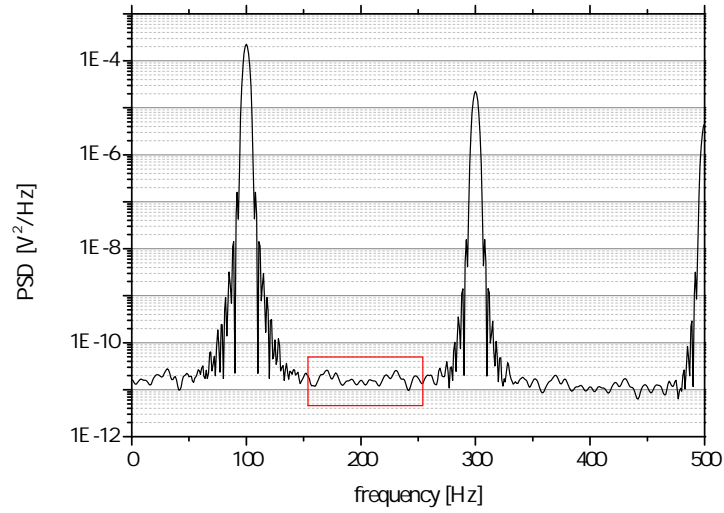


Fig. 6.4. – Zoomed view of the low frequency region. To compute the detectivity, the noise level at 200 Hz is of interest.

In Fig. 6.4 the simulated PSD is plotted after averaging 10 times. After averaging the theoretical noise level at the second harmonic peak at 200 Hz can be defined more accurately. To compute the detectivity (see also Eq. 2.1)

$$D = \frac{\sqrt{S_V(f) \left[ \frac{\text{V}^2}{\text{Hz}} \right]}}{\frac{dV}{dB} \left[ \frac{\text{V}}{\text{T}} \right]}$$

the sensitivity  $dV/dB$  has to be taken from the slope of the sensor characteristics, which is the magnitude of the second harmonic with respect to an external weak field along the easy axis of the MTJ. The sensor characteristic for the ideal theoretical limit can also be generated with the Monte Carlo simulation and is shown in Fig. 6.5.



The slope of the linear fit is  $32.5\text{V/T}$  and together with the PSD noise level from Fig. 6.4 of  $1.58 \cdot 10^{-11}\text{V}^2/\text{Hz}$  the detectivity results to

$$D = \frac{\sqrt{1.58 \cdot 10^{-11} \frac{\text{V}^2}{\text{Hz}}}}{32.5 \frac{\text{V}}{\text{T}}} \approx 122 \frac{\text{nT}}{\sqrt{\text{Hz}}}$$

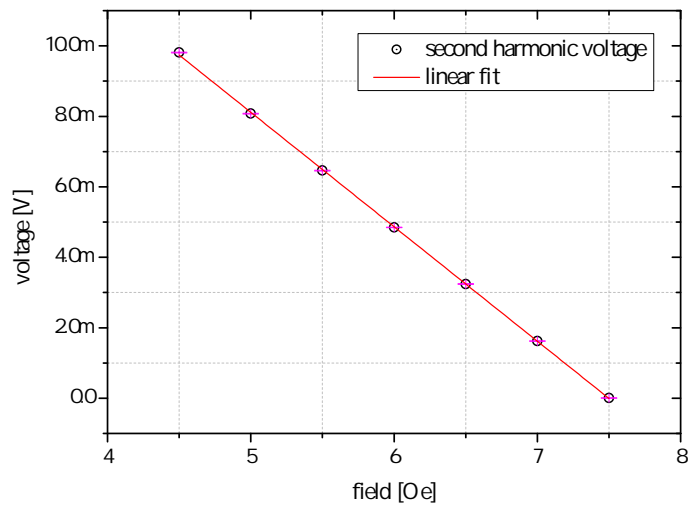


Fig. 6.5. – Simulated sensor characteristics for a 100 Hz driving field with 1 mT amplitude and a switching field of 0.7 mT.

## Outlook and Conclusion

In this thesis a sensor concept based on tunneling magnetoresistance (TMR) and the fluxgate measurement principle was presented, which was developed under the premise to detect weak magnetic fields down to the pico-Tesla range. Magnetic fields in this range occur as manifestations of neural activity of the human heart. The currently available methods to carry out magnetocardiographic measurements are based on SQUID sensors, which requires cooling to low temperatures of at least 77 K. Therefore, a sensor technology operating at room temperature that is compatible to standard CMOS fabrication processes would boost the availability of new diagnostic methods such as fetal magnetocardiography.

It was shown, that the fluxgate measurement principle can be applied to a magnetic tunnel junction (MTJ) and that the second harmonic can be calculated analytically (Chapter 3). Because this sensing principle relies on the reliable switching of the free layer's magnetization in a TMR element, thermal fluctuations affecting the switching process were considered to be a possible factor limiting the detectivity of TMR fluxgate sensors. In Chapter 4 the theoretical background of thermally activated switching of single domain magnetic particles was discussed and from this, a thermal switching field distribution (SFD) is derived based on a transition state theory model. The thermal SFD is a very general result and was derived in Ref. [87] for the first time. It reflects the impossibility of fully deterministic switching at finite temperature. Using the mathematical properties of the SFD as a probability density function a criterion for the validity of the applied model could be defined based on parameters such as the thermal stability of the magnetic particle and the field rate during the switching process. The SFD was also generated using a Monte Carlo simulation of a single macrospin written in MATLAB<sup>®</sup> and compared to a simulation of the stochastic Landau-Lifshitz-Gilbert equation, which validated the transition state theory based approach on the investigated time scale.

In Chapter 5 the experimental methods were presented reaching from the fabrication of TMR fluxgate sensors by optical lithography to digital signal processing for the evaluation of the measurement data. A tip probe measurement setup was used for the magnetic and electrical characterization of the MTJs fabricated for the TMR fluxgates. To test the sensing principle the setup was extended and time domain signals of the switching MTJ as well as second harmonic sensor characteristics were measured. The time domain data could be interpreted as rate-dependent magnetoresistance loops when currents of different frequencies were applied to the current line. The rate dependence of the switching fields is a consequence of

the thermal fluctuations that aid the switching process more effectively at lower field rates. The lock-in amplifier was used to measure the second harmonic and by varying the magnetic field from the coils of the tip probe setup TMR fluxgate sensor characteristics were obtained. The slope of the sensor characteristics, i.e. the sensitivity, was shown to agree well with the analytical result for the second harmonic signal.

Finally, in Chapter 6 time domain measurement data were evaluated together with the simulated signal based on the transition state theory model. The simulation represents an idealized case of the real switching behavior, which shows considerable jitter when the MTJ in the sensor is switched by the field from the current line along its easy axis. By applying a small hard axis bias field the time domain signal becomes stabilized and the switching gets closer to the coherent magnetization rotation used in the theoretical modeling. Therefore, the simulation data was used as an idealized limit representing the case where the noise originating from the thermal SFD is the only noise source present in the sensor. From the baseline of the spectrum of the the time domain signal the noise level at the second harmonic peak could be determined and by dividing with the sensor sensitivity a detectivity of approximately  $100 \text{ nT}/\sqrt{\text{Hz}}$  was estimated.

According to the reported detectivity, the TMR fluxgate sensing technology is not ready yet to compete in the quest for pico-Tesla field sensing. However, it was shown that MTJs can be operated as fluxgate sensors and deliver a linear field dependence in the second harmonic of their voltage signal. The fact that magnetization switching over high energy barriers at finite temperature is strongly non-deterministic is likely to obscure the benefit introduced by the possibility of using the lock-in measurement technique to reduce the equivalent noise bandwidth. As shown in the experiment, when the switching was stabilized with a small hard axis bias field the baseline of the spectrum of the measured TMR fluxgate signal dropped significantly. The exponent  $n$  of the energy barrier  $\Delta E = KV(1 - H/H_K)^n$  in the Stoner-Wohlfarth model for uniaxial anisotropy should differ in this case from the exponent derived for pure easy axis switching  $n = 2$ . It would be interesting to further investigate the role of the exponent and its interplay with the thermal fluctuations within a Monte Carlo simulation together with simulations of the stochastic Landau-Lifshitz-Gilbert equation, that models the equation of motion of a single spin in an effective field on a microscopic level. Also, the derived criterion for the breakdown of the transition state theory model seems to be worth of further investigation, as it tackles the question of how and to what extent the microscopic dynamics of a physical system can be coarse-grained.

If not yet applicable as a sensor for MCG, the fluxgate measurement principle applied to MTJs or GMR sensors could be used to measure the coercivities of the free layers by making use of the phase information that is delivered by the lock-in amplifier. This can also be done by applying the alternating field to switch the free layer periodically from an external coil and not necessarily from an integrated current line. With a

properly designed circuitry, where all possible phase shifters are known, this method could serve as a fast testing method for patterned sensor elements.

It was also shown, that the TMR effect can be used to investigate the rich switching behavior that is present in micron-scale patterned magnetic elements, which may give new insights into Barkhausen noise and critical phenomena. This will be of interest also for industrial sensor applications, where devices are required to operate at high reliability. It would be worth to further investigate the role of the bias field, that stabilized the switching, and investigate magnetic tunnel junctions, where the easy axis of the free layer is rotated with respect to the pinned layer's magnetization. The switching over large energy barriers has turned out to be very sensitive to thermal fluctuations, so modifying the magnetic energy landscape would open new paths for further exploring the application of the fluxgate principle to magnetoresistance sensors.

# Appendices

## A.1 Derivation of the Stoner-Wohlfarth astroid

$$\begin{aligned}
 \text{I: } \frac{\partial \eta}{\partial \varphi} &= \frac{1}{2} \sin 2(\varphi - \theta) + h \sin \varphi = 0 \\
 \text{II: } \frac{\partial^2 \eta}{\partial \varphi^2} &= \cos 2(\varphi - \theta) + h \cos \varphi = 0 \\
 \text{I} \cdot \cos \varphi - \text{II} \cdot \sin \varphi &: \frac{1}{2} \cos \varphi \sin 2(\varphi - \theta) + \cancel{h \sin \varphi \cos \varphi} \\
 &\quad - \sin \varphi \cos 2(\varphi - \theta) - \cancel{h \sin \varphi \cos \varphi} = 0 \\
 &\quad \frac{1}{2} \cos \varphi \sin 2(\varphi - \theta) = \sin \varphi \cos 2(\varphi - \theta) \\
 \varphi - \theta = \psi &: \tan 2\psi = 2 \tan(\psi + \theta) \\
 &\quad 2 \frac{\tan \psi}{1 - \tan^2 \psi} = 2 \frac{\tan \psi + \tan \theta}{1 - \tan \psi \tan \theta} \\
 \cancel{\tan \psi} - \cancel{\tan^2 \psi} \tan \theta &= \cancel{\tan \psi} + \tan \theta - \tan^3 \psi - \cancel{\tan^2 \psi} \tan \theta \\
 \Rightarrow \tan^3 \psi &= \tan \theta \tag{A.1}
 \end{aligned}$$

## A.2 Derivation of the switching field distribution with field-dependent attempt frequency

$$\begin{aligned}
 f_0 &= \frac{\alpha \gamma}{1 + \alpha^2} \sqrt{\frac{H_K^3 J_S V}{2\pi k_B T}} \left(1 - \frac{H}{H_K}\right) \left(1 - \frac{H^2}{H_K^2}\right) \\
 u &= \sqrt{\beta} \left(1 - \frac{H}{H_K}\right) \Rightarrow H = H_K \left(1 - \frac{u}{\sqrt{\beta}}\right) \\
 C &= \frac{\alpha \gamma}{1 + \alpha^2} \sqrt{\frac{H_K^3 J_S V}{2\pi k_B T}} \\
 \Rightarrow f_0(u) &= C \left(1 - 1 + \frac{u}{\sqrt{\beta}}\right) \left[1 - \left(1 - \frac{u}{\sqrt{\beta}}\right)^2\right] = C \frac{u^2}{\beta} \left(2 - \frac{u}{\sqrt{\beta}}\right) \tag{A.2}
 \end{aligned}$$

$$\begin{aligned}
\ln P_{\text{not}} &= -\frac{H_K}{R\sqrt{\beta}} \int_{u_0}^{\infty} f_0(u) e^{-u^2} du = -\frac{C}{\beta} \frac{H_K}{R\sqrt{\beta}} \int_{u_0}^{\infty} u^2 \left(2 - \frac{u}{\sqrt{\beta}}\right) e^{-u^2} du \\
&= -C' \int_{u_0}^{\infty} u^2 \left(2 - \frac{u}{\sqrt{\beta}}\right) e^{-u^2} du \quad \text{with } C' = \frac{C}{\beta} \frac{H_K}{R\sqrt{\beta}} \\
\text{with } \operatorname{erfc}(u_0) &= \frac{2}{\sqrt{\pi}} \int_{u_0}^{\infty} e^{-u^2} du = 1 - \operatorname{erf}(u_0), \quad \operatorname{erf}(u_0) = \frac{2}{\sqrt{\pi}} \int_0^{u_0} e^{-u^2} du \\
&= \frac{C'}{2\beta} e^{-u_0^2} (1 - 2\sqrt{\beta}u_0 + u_0^2) - \frac{C'\sqrt{\pi}}{2} \operatorname{erfc}(u_0) \\
\Rightarrow P(u_0) &= 1 - \exp \left\{ \frac{C'}{2\beta} e^{-u_0^2} (1 - 2\sqrt{\beta}u_0 + u_0^2) - \frac{C'\sqrt{\pi}}{2} \operatorname{erfc}(u_0) \right\} \quad (\text{A.3})
\end{aligned}$$

$$\begin{aligned}
\frac{dP}{dH_C} &= \frac{dP}{du_0} \frac{du_0}{dH_C} = -P_{\text{not}} \left( -\frac{\sqrt{\beta}}{H_K} \right) \left\{ \frac{C'}{2\sqrt{\beta}} e^{-u_0^2} (-2u_0) (1 - 2\sqrt{\beta}u_0 + u_0^2) \right\} \\
&\quad + \frac{C'}{2\sqrt{\beta}} e^{-u_0^2} (-2\sqrt{\beta} + 2u_0) + \frac{C'\sqrt{\pi}}{2} \frac{2}{\sqrt{\pi}} e^{-u_0^2} \\
\text{because } \frac{d}{du_0} \operatorname{erfc}(u_0) &= \frac{d}{du_0} [1 - \operatorname{erf}(u_0)] = -\frac{d}{du_0} \operatorname{erf}(u_0) \\
&= -\frac{d}{du_0} \left( \frac{2}{\sqrt{\pi}} \int_{u_0}^{\infty} e^{-u^2} du \right) = -\frac{2}{\pi} e^{-u_0^2} \\
&= \frac{\sqrt{\beta}}{H_K} P_{\text{not}} e^{-u_0^2} \left[ \frac{C'}{2\sqrt{\beta}} (-2u_0 + 4\sqrt{\beta}u_0^2 - 2u_0^3 - 2\sqrt{\beta} + 2u_0) + C' \right] \\
&= \frac{\sqrt{\beta}}{H_K} P_{\text{not}} e^{-u_0^2} C' \left[ 2u_0^2 - \frac{u_0^3}{\sqrt{\beta}} - \chi + \chi \right] \\
\text{with } C' &= \frac{\alpha\gamma}{1 + \alpha^2} \frac{H_K^2}{R\sqrt{\pi}\beta} \\
\Rightarrow \frac{dP}{dH_C} &= P_{\text{not}} \frac{\alpha\gamma}{1 + \alpha^2} \frac{H_K}{R\sqrt{\pi}\beta} \left( 2u_0^2 - \frac{u_0^3}{\sqrt{\beta}} \right) e^{-u_0^2}. \quad (\text{A.4})
\end{aligned}$$

## A.3 Monte Carlo Simulation Code

Listing A.1 – function to generate a driving field with constant rate

---

```

function [Ht, delta_H] = drive_field(f,H0, t, delta_t, N, p)

R = 4*H0*f;

for n = 1:1/2*N/p
    H(n) = H0 - R*t(n);
end

for n = 1/2*N/p+1:N/p+1

```

```
        H(n) = -3*H0 + R*t(n);  
    end
```

```
delta_H = R*delta_t;
```

```
for i=1:N/p:N  
    Ht(i:i+N/p) = H;  
end
```

---

Listing A.2 – test function for the driving field

---

```
clear all;  
f = 1e6;                % frequency of the driving field in Hz  
x = 1e3;                % discretization factor  
delta_t = 1/(x*f);     % sampling time interval in s  
H_0 = 10;               % amplitude of driving field in Oe  
%H_max = 0.2;  
H_x = 0;                % external weak magnetic field in Oe  
  
p = 100;                % number of observed cycles, i.e. periods  
t_obs = p*1/f;         % overall observation time in s  
  
T = 1/f;  
N = round(t_obs/delta_t); % number of data points  
  
t = (0:delta_t:t_obs);  
  
[H, delta_H] = drive_field(f, H_0, t, delta_t, N, p);  
  
figure()  
plot(t(1:2000), H(1:2000))
```

---



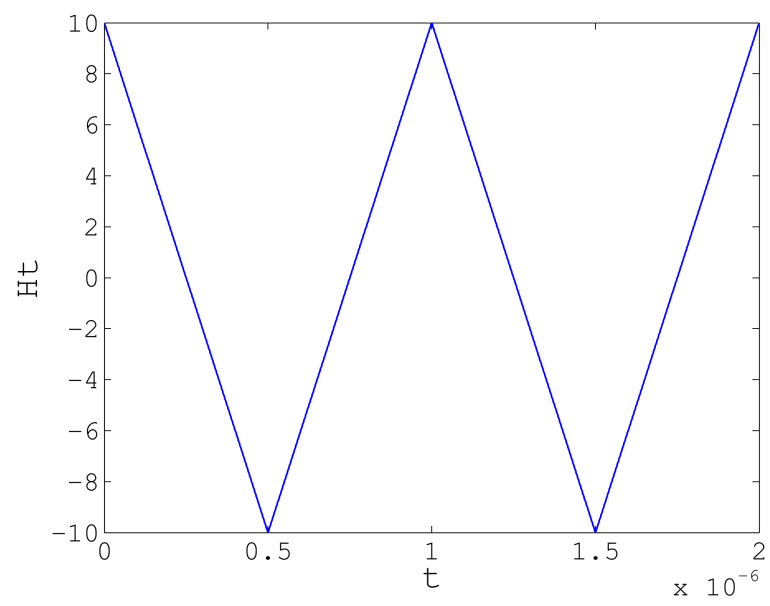


Fig. A.1. – Driving field function

## Fabrication details

## B.1 Photolithography Mask

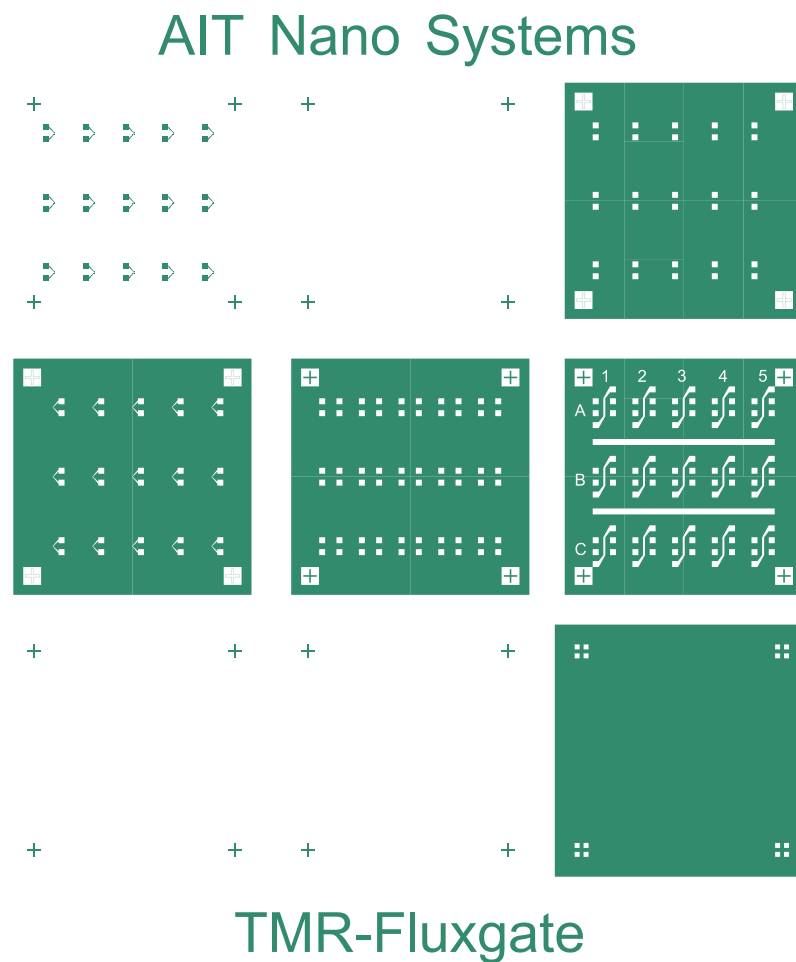


Fig. B.1. – Lithography mask for the TMR fluxgate fabrication process, lithography steps are arranged from upper left to bottom right: 1. backside contacts 2. magnetic tunnel junction elements (ellipses with  $a = 10\mu\text{m}$  and  $b = 5\mu\text{m}$ ) 3. vias for backside contacts and to tunnel junction top 4. top contacts 5. vias for backside and top contact pads 6. current line and contact pads.

## B.2 Sputter parameters

mat.	$d$ [nm]	rate [nm/s]	$p$ [ $\mu$ bar]	Ar flow [sccm]	power [W]	$t_{\text{pre}}$ [s]	$t_{\text{sputter}}$ [s]	$P_{\text{actual}}$ [W]	$V_{\text{actual}}$ [V]
Ta	5	0.347	1	10	115	30	14.41	117	280
Ru	40	0.335	1	10	115	30	119.4	118	313
IrMn	15	0.664	1	10	115	30	22.59	113	369
CoFe	2	0.303	1	10	115	30	6.60	118	342
CoFeB	2	0.214	1	10	115	30	9.35	118	364
MgO	2	0.022	2	6	150	30	90.91	$P_r = 7$ W	
CoFeB	2	0.214	1	10	115	180	28.04	118	360
Ta	2	0.347	1	10	115	30	5.76	117	288
Ru	10	0.335	1	10	115	30	29.85	118	314

Tab. B.1. – Sputter parameters for a magnetic multilayer deposited with a Leybold sputtering system. All materials are sputtered using Ar and use DC voltage targets, except MgO, which requires an RF voltage at a chamber base pressure of  $1 - 2 \cdot 10^{-7}$  mbar.  $d$  denotes the layer thickness,  $p$  the desired pressure during the sputtering process,  $t_{\text{pre}}$  and  $t_{\text{sputter}}$  are the (pre-)sputtering times. Presputtering is required to clean the targets before deposition.  $t_{\text{pre}}$  is higher directly after the MgO deposition to remove all oxidized material.  $P_{\text{actual}}$  and  $V_{\text{actual}}$  are the power and voltage that are actually present during the deposition and are monitored to measure the process stability. For MgO the power reflected back to the RF source  $P_r$  is available for this purpose.

## B.3 IBE Settings

angle	90° (step 1) or 25° (step 2)
sample holder rotation	3 rpm
Ar flow	10 sccm
Ar flow for cooling of the sample holder	1 sccm
beam current (regulated)	45 mA
nominal beam voltage	500 V
accelerator grid voltage	500 V
chamber base pressure	10 <sup>-6</sup> mbar
chamber process pressure	10 <sup>-4</sup> mbar
SIMS base pressure	10 <sup>-7</sup> mbar
SIMS process pressure	10 <sup>-6</sup> mbar

Tab. B.2. – Typical IBE parameters

## Bibliography

- [1] M. Pannetier et al. “Femtotesla Magnetic Field Measurement with Magnetoresistive Sensors”. *Science* 304 (2004): pp. 1648–1650.
- [2] A. S. Edelstein et al. “Progress toward a thousandfold reduction in 1/f noise in magnetic sensors using an ac microelectromechanical system flux concentrator (invited)”. *Journal of Applied Physics* 99 (8), 08B317 (2006).
- [3] S. Groeger et al. “A high-sensitivity laser-pumped Mx magnetometer”. *The European Physical Journal D - Atomic, Molecular, Optical and Plasma Physics* 38 (2) (2006): pp. 239–247.
- [4] W. F. Egelhoff et al. “Critical challenges for picoTesla magnetic-tunnel-junction sensors”. *Sensors and Actuators A* 155 (2009): pp. 217–225.
- [5] R. Ferreira et al. “Tuning of MgO barrier magnetic tunnel junction bias current for picotesla magnetic field detection”. *Journal of Applied Physics* 99 (8), 08K706 (2006).
- [6] R. C. Chaves et al. “Low frequency picotesla field detection using hybrid MgO based tunnel sensors”. *Applied Physics Letters* 91 (10), 102504 (2007).
- [7] D. Robbes. “Highly sensitive magnetometers - a review”. *Sensors and Actuators A: Physical* 129 (2006): pp. 86–93.
- [8] R. H. Koch and J. R. Rozen. “Low-noise flux-gate magnetic-field sensors using ring- and rod-core geometries”. *Applied Physics Letters* 78 (13) (2001): pp. 1897–1899.
- [9] N. A. Stutzke et al. “Low-frequency noise measurements on commercial magnetoresistive magnetic field sensors”. *Journal of Applied Physics* 97 (10), 10Q107 (2005).
- [10] P. Ripka. “Advances in fluxgate sensors”. *Sensors and Actuators A: Physical* 106 (2003). Proceedings of the 4th European Magnetic Sensors and Actuators Conference: pp. 8–14.
- [11] P. P. Freitas et al. “Magnetoresistive sensors”. *Journal of Physics: Condensed Matter* 19 (16), 165221 (2007).

- [12] L. E. Reichl. *A Modern Course in Statistical Physics*. 2nd Edition. Wiley-VCH, 2004.
- [13] R. Kubo. “The fluctuation-dissipation theorem”. *Reports on progress in physics* 29 (1) (1966): p. 255.
- [14] Wikipedia. *Fluctuation Dissipation Theorem*. June 2016. URL: [https://en.wikipedia.org/wiki/Fluctuation-dissipation\\_theorem](https://en.wikipedia.org/wiki/Fluctuation-dissipation_theorem).
- [15] H. Nyquist. “Thermal Agitation of Electric Charge in Conductors”. *Phys. Rev.* 32 (1928): pp. 110–113.
- [16] W. Schottky. “Über spontane Stromschwankungen in verschiedenen Elektrizitätsleitern”. *Annalen der Physik* 362 (1918): pp. 541–567.
- [17] Y.M. Blanter and M. Büttiker. “Shot noise in mesoscopic conductors”. *Physics Reports* 336 (2000): pp. 1–166.
- [18] T. Arakawa et al. “Sub-Poissonian shot noise in CoFeB/MgO/CoFeB-based magnetic tunneling junctions”. *Applied Physics Letters* 98, 202103 (2011).
- [19] T. Arakawa et al. “Low-frequency and shot noises in CoFeB/MgO/CoFeB magnetic tunneling junctions”. *Phys. Rev. B* 86, 224423 (2012).
- [20] K. Liu, K. Xia, and G. Bauer. “Shot noise in magnetic tunnel junctions from first principles”. *Phys. Rev. B* 86, 020408 (2012).
- [21] S. Yuasa and D. D. Djayaprawira. “Giant tunnel magnetoresistance in magnetic tunnel junctions with a crystalline MgO(001) barrier”. *Journal of Physics D: Applied Physics* 40 (21) (2007): R337.
- [22] J.P. Cascales Sandoval. “Conductance and noise in magnetic tunnel junctions with inorganic and organic barriers”. PhD thesis. Departamento de Física de la Materia Condensada, Universidad Autónoma de Madrid, Madrid, Spain, 2015.
- [23] F.N. Hooge, T. G. M. Kleinpenning, and L. K. J. Vandamme. “Experimental studies on 1/f noise”. *Reports on Progress in Physics* 44 (5) (1981): p. 479.
- [24] M. von Haartman and M. Östling. *Low-frequency noise in advanced MOS devices*. Ed. by Mohammed Ismail. ANALOG CIRCUITS AND SIGNAL PROCESSING SERIES. Springer, 2007.
- [25] S. Ingvarsson et al. “Low-Frequency Magnetic Noise in Micron-Scale Magnetic Tunnel Junctions”. *Phys. Rev. Lett.* 85 (2000): pp. 3289–3292.
- [26] A. McWorther. “1/f noise and germanium surface properties”. *Semiconductor Surface Physics*. Ed. by R.H. Kingston. Pennsylvania Press, 1957, pp. 207–228.
- [27] R. Stearrett et al. “Magnetic noise evolution in CoFeB/MgO/CoFeB tunnel junctions during annealing”. *Applied Physics Letters* 97 (24), 243502 (2010).

- [28] S. H. Liou et al. “Dependence of noise in magnetic tunnel junction sensors on annealing field and temperature”. *Journal of Applied Physics* 103, 07E920 (2008).
- [29] N. Smith and P. Arnett. “White-noise magnetization fluctuations in magnetoresistive heads”. *Applied Physics Letters* 78 (10) (2001): pp. 1448–1450.
- [30] H. Kamerlingh Onnes. “Further experiments with Liquid Helium. D. On the change of Electrical Resistance of Pure Metals at very low Temperatures, etc. V. The Disappearance of the resistance of mercury”. *Proceedings of the Royal Netherlands Academy of the Arts and Sciences* 14 I (1911): pp. 113–115.
- [31] D. van Delft and P. Kes. “The discovery of superconductivity”. *Physics Today* 16 (2010): pp. 38–42.
- [32] S. Bose. “Plancks Gesetz und Lichtquantenhypothese”. *Zeitschrift für Physik* 26 (1924): pp. 178–181.
- [33] M. Anderson et al. “Observation of Bose-Einstein condensation in a dilute atomic vapor”. *Science* 269 (5221) (1995): pp. 198–201.
- [34] K. Davis et al. “Bose-Einstein condensation in a gas of sodium atoms”. *Physical review letters* 75 (22) (1995): p. 3969.
- [35] L. N. Cooper. “Bound Electron Pairs in a Degenerate Fermi Gas”. *Phys. Rev.* 104 (4 1956): pp. 1189–1190.
- [36] J. Bardeen, L. N. Cooper, and J. R. Schrieffer. “Theory of Superconductivity”. *Phys. Rev.* 108 (5 1957): pp. 1175–1204.
- [37] J. G. Bednorz and K. A. Müller. “Possible high- $T_C$  superconductivity in the Ba-La-Cu-O system”. *Ten Years of Superconductivity: 1980–1990*. Springer, 1986, pp. 267–271.
- [38] T. Laegreid et al. “Specific heat anomaly at 220 K connected with superconductivity at 90 K in ceramic  $\text{YBa}_2\text{Cu}_3\text{O}_{7-\delta}$ ”. *Nature* 330 (1987): pp. 637–638.
- [39] D. Lathrop, S. Russek, and R. Buhrman. “Production of  $\text{YBa}_2\text{Cu}_3\text{O}_{7-\delta}$  superconducting thin films insitu by high-pressure reactive evaporation and rapid thermal annealing”. *Applied physics letters* 51 (19) (1987): pp. 1554–1556.
- [40] P. Ripka, ed. *Magnetic sensors and Magnetometers*. ARTECH HOUSE, INC., 2001.
- [41] C. Kittel. *Einführung in die Festkörperphysik*. Ed. by Prof. Dr. S. Hunklinger. Oldenbourg Wissenschaftsverlag GmbH, 2006.
- [42] R. Ochsenfeld W. Meissner. “Ein neuer Effekt bei Eintritt der Supraleitfähigkeit”. *Naturwissenschaften* 21 (1933): pp. 787–788.

- [43] F. London and H. London. “The electromagnetic equations of the supraconductor”. *Proceedings of the Royal Society of London A: Mathematical, Physical and Engineering Sciences*. Vol. 149. The Royal Society. 1935, pp. 71–88.
- [44] B. D. Josephson. “Possible new effects in superconductive tunnelling”. *Physics letters* 1 (1962): p. 251.
- [45] W. Jenks, I. Thomas, and J. Wikswo Jr. “Encyclopedia of Applied Physics”. Vol. 19. VCH Publishers, Inc., 1997. Chap. SQUIDS, p. 457.
- [46] R. Jaklevic et al. “Quantum interference effects in Josephson tunneling”. *Physical Review Letters* 12 (7) (1964): p. 159.
- [47] J. Clarke et al. *The SQUID Handbook*. Ed. by J. Clarke and A.I. Braginski. Vol. 1. Wiley-VCH, 2004.
- [48] F. Primdahl. “The fluxgate mechanism, part I: The gating curves of parallel and orthogonal fluxgates”. *IEEE Transactions on Magnetics* 6 (2) (1970): pp. 376–383.
- [49] P. M. Drljača et al. “Single core fully integrated CMOS micro-fluxgate magnetometer”. *Sensors and Actuators A: Physical* 110 (2004): p. 236.
- [50] T. O’Donnell et al. “Planar fluxgate current sensor integrated in printed circuit board”. *Sensors and Actuators A: Physical* 129 (2006): pp. 20–24.
- [51] S. Blundell. *Magnetism in Condensed Matter*. Oxford University Press, 2001.
- [52] P. Mohn. *Magnetism in the solid state: an introduction*. Vol. 134. Springer Science & Business Media, 2006.
- [53] N. F. Mott. “A discussion of the transition metals on the basis of quantum mechanics”. *Proceedings of the Physical Society* 47 (1935): p. 571.
- [54] N. F. Mott. “The electrical conductivity of transition metals”. *Proceedings of the Royal Society of London A: Mathematical, Physical and Engineering Sciences*. Vol. 153. The Royal Society. 1936, pp. 699–717.
- [55] Nobel Prize Committee. *Press Release, Oct 9 2007*. June 2016. URL: [http://www.nobelprize.org/nobel\\_prizes/physics/laureates/2007/press.html](http://www.nobelprize.org/nobel_prizes/physics/laureates/2007/press.html).
- [56] R. Q. Hood and L. M. Falicov. “Boltzmann-equation approach to the negative magnetoresistance of ferromagnetic-normal-metal multilayers”. *Phys. Rev. B* 46 (1992): pp. 8287–8296.
- [57] T. Valet and A. Fert. “Theory of the perpendicular magnetoresistance in magnetic multilayers”. *Phys. Rev. B* 48 (1993): pp. 7099–7113.
- [58] V.V. Ustinov and E.A. Kravtsov. “A unified semiclassical theory of parallel and perpendicular giant magnetoresistance in metallic superlattices”. *Journal of Physics: Condensed Matter* 7 (18) (1995): p. 3471.



- [59] I. Ennen et al. "Giant Magnetoresistance: Basic Concepts, Microstructure, Magnetic Interactions and Applications". *Sensors* 16 (6) (2016): p. 904.
- [60] E.Y. Tsymbal and D.G. Pettifor. "Perspectives of giant magnetoresistance". Ed. by Henry Ehrenreich and Frans Spaepen. Vol. 56. *Solid State Physics*. Academic Press, 2001, pp. 113–237.
- [61] S. S. P. Parkin, Z. G. Li, and David J. Smith. "Giant magnetoresistance in antiferromagnetic Co/Cu multilayers". *Applied Physics Letters* 58 (23) (1991): pp. 2710–2712.
- [62] M. Ye. Zhuravlev et al. "Reliable prediction of giant magnetoresistance characteristics". *Phys. Rev. B* 65, 144428 (2002).
- [63] A. Shoshi et al. "Magnetoresistive-based real-time cell phagocytosis monitoring". *Biosensors and Bioelectronics* 36 (1) (2012): pp. 116–122.
- [64] W. F. Egelhoff et al. "Magnetoresistance values exceeding 21% in symmetric spin valves". *Journal of Applied Physics* 78 (1) (1995): pp. 273–277.
- [65] M. Julliere. "Tunneling between ferromagnetic films". *Physics letters A* 54 (3) (1975): pp. 225–226.
- [66] J. S. Moodera et al. "Large Magnetoresistance at Room Temperature in Ferromagnetic Thin Film Tunnel Junctions". *Phys. Rev. Lett.* 74 (1995): pp. 3273–3276.
- [67] T. Miyazaki and N. Tezuka. "Giant magnetic tunneling effect in Fe/Al<sub>2</sub>O<sub>3</sub>/Fe junction". *Journal of Magnetism and Magnetic Materials* 139 (3) (1995): pp. L231–L234.
- [68] W. H. Butler et al. "Spin-dependent tunneling conductance of Fe|MgO|Fe sandwiches". *Phys. Rev. B* 63, 054416 (2001).
- [69] X.-G. Zhang and W. H. Butler. "Large magnetoresistance in bcc Co/MgO/Co and FeCo/MgO/FeCo tunnel junctions". *Phys. Rev. B* 70, 172407 (2004).
- [70] S.S.P. Parkin et al. "Giant tunnelling magnetoresistance at room temperature with MgO (100) tunnel barriers". *Nature materials* 3 (12) (2004): pp. 862–867.
- [71] D.D. Djayaprawira et al. "230 % room-temperature magnetoresistance in CoFeB/MgO/CoFeB magnetic tunnel junctions". *Applied Physics Letters* 86, 092502 (2005).
- [72] S. Yuasa et al. "Characterization of growth and crystallization processes in CoFeB/MgO/CoFeB magnetic tunnel junction structure by reflective high-energy electron diffraction". *Applied Physics Letters* 87, 242503 (2005).
- [73] E. E. Fullerton and J. R. Childress. "Spintronics, Magnetoresistive Heads, and the Emergence of the Digital World". *PP* (99) (2016): pp. 1–9.

- [74] G. Baule and R. McFee. "Detection of the magnetic field of the heart". *American Heart Journal* 66 (1963): p. 95.
- [75] D. Cohen, E. A. Edelsack, and J. E. Zimmerman. "Magnetocardiograms taken inside a shielded room with a superconducting point-contact magnetometer". *Applied Physics Letters* 16 (1970): pp. 278–280.
- [76] J. Malmivuo and R. Plonsey. *Bioelectromagnetism - Principles and Applications of Bioelectric and Biomagnetic Fields*. Oxford University Press, 1995.
- [77] STUDYBLUE. *Cardiac Conduction System*. July 2016. URL: <https://www.studyblue.com/#flashcard/view/5750010>.
- [78] T. F. Oostendorp and A. Van Oosterom. "Modelling the fetal magnetocardiogram". *Clinical Physics and Physiological Measurement* 12 (1991): p. 15.
- [79] H. Hamada et al. "Prenatal diagnosis of long QT syndrome using fetal magnetocardiography". *Prenatal Diagnosis* 19 (7) (1999): pp. 677–680.
- [80] M. Peters et al. "Monitoring the fetal heart non-invasively: a review of methods". *Journal of perinatal medicine* 29 (2001): p. 408.
- [81] H.J.M. Ter Brake et al. "Fetal magnetocardiography: clinical relevance and feasibility". *Physica C: Superconductivity* 368 (2002): p. 10.
- [82] R Stolz et al. "Integrated gradiometer-SQUID system for fetal magnetocardiography without magnetic shielding". *Superconductor Science and Technology* 16 (12) (2003): p. 1523.
- [83] K. Tsukada et al. "Newly Developed Magnetocardiographic System for Diagnosing Heart Disease". *Hitachi Review* 50 (2001): p. 13.
- [84] R. Sturm et al. "Multi-channel magnetocardiography for detecting beat morphology variations in fetal arrhythmias". *Prenatal diagnosis* 24 (1) (2004): p. 1.
- [85] M. DeMelis et al. "Magnetocardiographic signal analysis". *Proceedings of the 13th international conference on biomagnetismBIOMAG*. 2002, pp. 987–989.
- [86] L. Breth et al. "Fluxgate Principle Applied to a Magnetic Tunnel Junction for Weak Magnetic Field Sensing". *IEEE Transactions on Magnetics* 47 (6) (2011): pp. 1549–1553.
- [87] L. Breth et al. "Thermal switching field distribution of a single domain particle for field-dependent attempt frequency". *Journal of Applied Physics* 112 (2), 023903 (2012): p. 023903.
- [88] E. C. Stoner and E. P. Wohlfarth. "A Mechanism of Magnetic Hysteresis in Heterogeneous Alloys". *Philosophical Transactions of the Royal Society of London. Series A, Mathematical and Physical Sciences* 240 (826) (1948): pp. 599–642.
- [89] R. Skomski. *Simple Models of Magnetism*. Oxford University Press, 2008.

- [90] J. P. Sethna. *Statistical Mechanics: Entropy, Order Parameters, and Complexity*. Oxford University Press, 2006.
- [91] R. Wood. “Exact Solution for a Stoner-Wohlfarth Particle in an Applied Field and a New Approximation for the Energy Barrier”. *IEEE Transactions on Magnetism* 45 (1) (2009): pp. 100–103.
- [92] D. Jiles. *Introduction to Magnetism and Magnetic Materials*. Third Edition. CRC Press, 2015.
- [93] P. Hänggi, P. Talkner, and M. Borkovec. “Reaction-rate theory: fifty years after Kramers”. *Rev. Mod. Phys.* 62 (1990): pp. 251–341.
- [94] T. L. Gilbert. “A phenomenological theory of damping in ferromagnetic materials”. *IEEE Transactions on Magnetism* 40 (2004): pp. 3443–3449.
- [95] W. F. Brown. “Thermal Fluctuations of a Single-Domain Particle”. *Phys. Rev.* 130 (1963): pp. 1677–1686.
- [96] L. Néel. “Some theoretical aspects of rock-magnetism”. *Advances in Physics* 4 (14) (1955): pp. 191–243.
- [97] M. Sharrock and J. McKinney. “Kinetic effects in coercivity measurements”. *IEEE Transactions on Magnetism* 17 (1981): pp. 3020–3022.
- [98] D. Suess et al. “Reliability of Sharrocks equation for exchange spring bilayers”. *Phys. Rev. B* 75, 174430 (May 2007).
- [99] P. Gaunt. “Magnetic viscosity and thermal activation energy”. *Journal of Applied Physics* 59 (12) (1986): pp. 4129–4132.
- [100] R. H. Victora. “Predicted time dependence of the switching field for magnetic materials”. *Phys. Rev. Lett.* 63 (1989): pp. 457–460.
- [101] H. Pfeiffer. “Determination of anisotropy field distribution in particle assemblies taking into account thermal fluctuations”. *physica status solidi (a)* 118 (1) (1990): pp. 295–306.
- [102] R. W. Chantrell, G. N. Coverdale, and K. O’Grady. “Time dependence and rate dependence of the coercivity of particulate recording media”. *Journal of Physics D: Applied Physics* 21 (1988): pp. 1469–1471.
- [103] X. Feng and P. B. Visscher. “Sweep-rate-dependent coercivity simulation of FePt particle arrays”. *Journal of Applied Physics* 95 (2004): pp. 7043–7045.
- [104] Q. Peng and H.J. Richter. “Field sweep rate dependence of media dynamic coercivity”. *IEEE Transactions on Magnetism* 40 (4) (2004): pp. 2446–2448.
- [105] W. T. Coffey et al. “Effect of an oblique magnetic field on the superparamagnetic relaxation time. II. Influence of the gyromagnetic term”. *Phys. Rev. B* 58 (1998): pp. 3249–3266.

- [106] Y. P. Kalmykov. “The relaxation time of the magnetization of uniaxial single-domain ferromagnetic particles in the presence of a uniform magnetic field”. *Journal of Applied Physics* 96 (2) (2004): pp. 1138–1145.
- [107] M. El-Hilo et al. “The sweep rate dependence of coercivity in recording media”. *Journal of Magnetism and Magnetic Materials* 117 (3) (1992): pp. L307–L310.
- [108] J. Kurkijärvi. “Intrinsic Fluctuations in a Superconducting Ring Closed with a Josephson Junction”. *Phys. Rev. B* 6 (1972): pp. 832–835.
- [109] I. Klik, C.-R. Chang, and H.-L. Huang. “Dynamics of micromagnetic measurements”. *Phys. Rev. B* 47 (14) (1993): p. 8605.
- [110] O. Hovorka et al. “Distribution of switching fields in magnetic granular materials”. *Applied Physics Letters* 101 (18), 182405 (2012): p. 182405.
- [111] R. Dittrich et al. “A path method for finding energy barriers and minimum energy paths in complex micromagnetic systems”. *Journal of Magnetism and Magnetic Materials* 250 (2002): pp. 12–19.
- [112] D. Suess et al. “Calculation of coercivity of magnetic nanostructures at finite temperatures”. *Phys. Rev. B* 84, 224421 (Dec. 2011).
- [113] I. Klik, C.-R. Chang, and H. L. Huang. “Field-dependent prefactor of the thermal relaxation rate in single-domain magnetic particles”. *Phys. Rev. B* 48 (1993): pp. 15823–15828.
- [114] G.T. Landi. “Dynamic symmetry loss of high-frequency hysteresis loops in single-domain particles with uniaxial anisotropy”. *Journal of Magnetism and Magnetic Materials* 324 (2012): pp. 466–470.
- [115] N. Metropolis and S. Ulam. “The Monte Carlo Method”. *Journal of the American statistical association* 44 (247) (1949): pp. 335–341.
- [116] W. K. Hastings. “Monte Carlo sampling methods using Markov chains and their applications”. *Biometrika* 57 (1) (1970): pp. 97–109.
- [117] D.P. Landau and K. Binder. *A Guide to Monte Carlo Simulations in Statistical Physics*. Fourth Edition. Cambridge University Press, 2015.
- [118] N. Metropolis et al. “Equation of State Calculations by Fast Computing Machines”. *The Journal of Chemical Physics* 21 (6) (1953): pp. 1087–1092.
- [119] R. W. Chantrell et al. “Calculations of the susceptibility of interacting superparamagnetic particles”. *Phys. Rev. B* 63, 024410 (2000).
- [120] W. Scholz, T. Schrefl, and J. Fidler. “Micromagnetic simulation of thermally activated switching in fine particles”. *Journal of Magnetism and Magnetic Materials* 233 (3) (2001): pp. 296–304.

- [121] J. L. García-Palacios and F. J. Lázaro. “Langevin-dynamics study of the dynamical properties of small magnetic particles”. *Phys. Rev. B* 58 (22 Dec. 1998): pp. 14937–14958.
- [122] M. Kirschner et al. “Cell size corrections for nonzero-temperature micromagnetics”. *Journal of Applied Physics* 97, 10E301 (2005).
- [123] K. Wasa, I. Kanno, and H. Kotera, eds. *Handbook of Sputter Deposition Technology*. 2nd Edition. Elsevier Inc., 2012.
- [124] C. Mack. *Fundamental Principles of Optical Lithography - The Science of Microfabrication*. WILEY, 2007.
- [125] M. J. Madou. *Fundamentals of Microfabrication: the Science of Miniaturization*. 2nd Edition. CRC press, 2002.
- [126] K. R. Lee, K. B. Sundaram, and D. C. Malocha. “Studies on deposition parameters of siliconnitride films prepared by a silane-nitrogen plasma-enhanced-chemical-vapour-deposition process”. *Journal of Materials Science: Materials in Electronics* 5 (1994): pp. 255–259.
- [127] A. Wiersch et al. “Room-temperature deposition of SiN<sub>x</sub> using ECR-PECVD for III/V semiconductor microelectronics in lift-off technique”. *Journal of Non-Crystalline Solids* 187 (1995): pp. 334–339.
- [128] G. Gerlach and W. Dötzel. *Introduction to microsystem technology*. John Wiley & Sons, Ltd, 2008.
- [129] H. Jansen et al. “A survey on the reactive ion etching of silicon in microtechnology”. *Journal of Micromechanics and Microengineering* 6 (1996): pp. 14–28.
- [130] Wikipedia. *Wafer*. German. July 2016. URL: [https://de.wikipedia.org/wiki/Wafer#cite\\_note-3](https://de.wikipedia.org/wiki/Wafer#cite_note-3).
- [131] Semiconductor Engineering. *What Happened To 450mm?* July 2016. URL: <http://semiengineering.com/what-happened-to-450mm/>.
- [132] C. W. Gwyn et al. “Extreme ultraviolet lithography”. *Journal of Vacuum Science & Technology B* 16 (6) (1998): pp. 3142–3149.
- [133] E. Platzgummer and H. Loeschner. “Charged particle nanopatterning”. *Journal of Vacuum Science & Technology B* 27 (6) (2009): pp. 2707–2710.
- [134] Microchemicals. *AZ<sup>®</sup> MiR<sup>TM</sup> 701*. July 2016. URL: <http://www.microchemicals.com/micro/mir7011.pdf>.
- [135] G. Harman and J. Albers. “The ultrasonic welding mechanism as applied to aluminum-and gold-wire bonding in microelectronics”. *IEEE Transactions on parts, hybrids, and packaging* 13 (4) (1977): pp. 406–412.

- [136] P.D. Richard et al. “Low temperature deposition of amorphous silicon oxide and silicon nitride films”. *Journal of Non-Crystalline Solids* 77 (1985): pp. 925–928.
- [137] J. Ya-Min Lee, K. Sooriakumar, and M. M. Dange. “The preparation, characterization and application of plasma-enhanced chemically vapour deposited silicon nitride films deposited at low temperatures”. *Thin Solid Films* 203 (2) (1991): pp. 275–287.
- [138] MicroChem. *LOR and PMGI Resists*. June 2016. URL: <http://microchem.com/pdf/PMGI-Resists-data-sheetV-rhcredit-102206.pdf>.
- [139] C. Blatter. *Komplexe Analysis, Fourier- und Laplace-Transformation für Elektroingenieure*. German. ETH Zurich. Jan. 2006. URL: [https://people.math.ethz.ch/~blatter/complex\\_8.pdf](https://people.math.ethz.ch/~blatter/complex_8.pdf).
- [140] G. Heinzel, A. Rüdiger, and R. Schilling. *Spectrum and spectral density estimation by the Discrete Fourier transform (DFT), including a comprehensive list of window functions and some new at-top windows*. Max Planck Institute for Gravitational Physics. 2002. URL: <http://hdl.handle.net/11858/00-001M-0000-0013-557A-5>.
- [141] Stefan Mayer Instruments GmbH. *Miniatur-Magnetfeldsensor FLC 100*. German. Apr. 2016. URL: <http://www.stefan-mayer.com/de/produkte/magnetometer-und-sensoren/magnetfeldsensor-flc-100.html>.
- [142] W. H. Meiklejohn and C. P. Bean. “New Magnetic Anisotropy”. *Phys. Rev.* 102 (1956): pp. 1413–1414.
- [143] W. H. Meiklejohn and C. P. Bean. “New Magnetic Anisotropy”. *Phys. Rev.* 105 (1957): pp. 904–913.
- [144] R. L. Stamps. “Mechanisms for exchange bias”. *Journal of Physics D: Applied Physics* 33 (23) (2000): R247.
- [145] A. P. Malozemoff. “Random-field model of exchange anisotropy at rough ferromagnetic-antiferromagnetic interfaces”. *Phys. Rev. B* 35 (7 Mar. 1987): pp. 3679–3682.
- [146] D. Mauri et al. “Simple model for thin ferromagnetic films exchange coupled to an antiferromagnetic substrate”. *Journal of Applied Physics* 62 (7) (1987): pp. 3047–3049.
- [147] M. D. Stiles and R. D. McMichael. “Model for exchange bias in polycrystalline ferromagnet-antiferromagnet bilayers”. *Phys. Rev. B* 59 (5 Feb. 1999): pp. 3722–3733.
- [148] T. C. Schulthess and W. H. Butler. “Consequences of Spin-Flop Coupling in Exchange Biased Films”. *Phys. Rev. Lett.* 81 (1998): pp. 4516–4519.
- [149] U. Nowak et al. “Domain state model for exchange bias. I. Theory”. *Phys. Rev. B* 66, 014430 (2002).

- [150] M. A. Ruderman and C. Kittel. “Indirect Exchange Coupling of Nuclear Magnetic Moments by Conduction Electrons”. *Phys. Rev.* 96 (1954): pp. 99–102.
- [151] T. Kasuya. “A Theory of Metallic Ferro- and Antiferromagnetism on Zener’s Model”. *Progress of Theoretical Physics* 16 (1956): pp. 45–57.
- [152] K. Yosida. “Magnetic Properties of Cu-Mn Alloys”. *Phys. Rev.* 106 (1957): pp. 893–898.
- [153] M. N. Baibich et al. “Giant Magnetoresistance of (001)Fe/(001)Cr Magnetic Superlattices”. *Phys. Rev. Lett.* 61 (1988): pp. 2472–2475.
- [154] G. Binasch et al. “Enhanced magnetoresistance in layered magnetic structures with antiferromagnetic interlayer exchange”. *Phys. Rev. B* 39 (1989): pp. 4828–4830.
- [155] E. Kerr, S. van Dijken, and J. M. D. Coey. “Influence of the annealing field strength on exchange bias and magnetoresistance of spin valves with IrMn”. *Journal of Applied Physics* 97, 093910 (2005).
- [156] C. Y. You et al. “Exchange bias of spin valve structure with a top-pinned  $\text{Co}_{40}\text{Fe}_{40}\text{B}_{20}/\text{IrMn}$ ”. *Applied Physics Letters* 93, 012501 (2008).
- [157] H. Ohldag et al. “Correlation between Exchange Bias and Pinned Interfacial Spins”. *Phys. Rev. Lett.* 91, 017203 (2003).
- [158] K. O’Grady, L.E. Fernandez-Outon, and G. Vallejo-Fernandez. “A new paradigm for exchange bias in polycrystalline thin films”. *Journal of Magnetism and Magnetic Materials* 322 (8) (2010): pp. 883–899.
- [159] J. Hayakawa et al. “Current-Driven Magnetization Switching in CoFeB/MgO/CoFeB Magnetic Tunnel Junctions”. *Japanese Journal of Applied Physics* 44 (2005): p. L1267.
- [160] Y. Fu, X. Cheng, and Z. Yang. “Magnetically soft and high-saturation-magnetization FeCo films fabricated by co-sputtering”. *physica status solidi (a)* 202 (6) (2005): pp. 1150–1154.
- [161] L. E. Fernandez-Outon et al. “Large Exchange Bias IrMn/CoFe for Magnetic Tunnel Junctions”. *IEEE Transactions on Magnetics* 44 (11) (2008): pp. 2824–2827.
- [162] D.-H. Kim, S.-B. Choe, and S.-C. Shin. “Direct Observation of Barkhausen Avalanche in Co Thin Films”. *Phys. Rev. Lett.* 90, 087203 (2003).
- [163] S. Zapperi et al. “Dynamics of a ferromagnetic domain wall: Avalanches, depinning transition, and the Barkhausen effect”. *Phys. Rev. B* 58 (1998): pp. 6353–6366.
- [164] G. Durin and S. Zapperi. “Scaling Exponents for Barkhausen Avalanches in Polycrystalline and Amorphous Ferromagnets”. *Phys. Rev. Lett.* 84 (2000): pp. 4705–4708.

- [165] L. Laurson, G. Durin, and S. Zapperi. “Universality classes and crossover scaling of Barkhausen noise in thin films”. *Phys. Rev. B* 89 (10 Mar. 2014): p. 104402.
- [166] S. Zhang et al. “Quenching of Magnetoresistance by Hot Electrons in Magnetic Tunnel Junctions”. *Phys. Rev. Lett.* 79 (1997): pp. 3744–3747.
- [167] S. Ringer et al. “Conductance anomalies of CoFeB/MgO/CoFeB magnetic tunnel junctions”. *Phys. Rev. B* 90, 174401 (2014).
- [168] W. F. Brinkman, R. C. Dynes, and J. M. Rowell. “Tunneling Conductance of Asymmetrical Barriers”. *Journal of Applied Physics* 41 (1970): p. 1915.
- [169] H. Brückl et al. “Evolution of barrier asymmetry in magnetic tunnel junctions”. *Applied Physics Letters* 78 (8) (2001): pp. 1113–1115.
- [170] R. Jansen and J. S. Moodera. “Influence of barrier impurities on the magnetoresistance in ferromagnetic tunnel junctions”. *Journal of Applied Physics* 83 (11) (1998): pp. 6682–6684.
- [171] A. N. Chiamonti et al. “Effects of annealing on local composition and electrical transport correlations in MgO-based magnetic tunnel junctions”. *Applied Physics Letters* 93 (10), 103113 (2008).
- [172] G. X. Miao et al. “Disturbance of Tunneling Coherence by Oxygen Vacancy in Epitaxial Fe/MgO/Fe Magnetic Tunnel Junctions”. *Phys. Rev. Lett.* 100 (2008): p. 246803.
- [173] F. Schleicher et al. “Localized states in advanced dielectrics from the vantage of spin-and symmetry-polarized tunnelling across MgO”. *Nature communications* 5, 4547 (2014).
- [174] A. Bachleitner-Hofmann et al. “Unexpected Width of Minor Magnetic Hysteresis Loops in Nanostructures”. *IEEE Transactions on Magnetism* 52 (2016): pp. 1–4.
- [175] EG&G Princeton Applied Research. *Explore the Lock-In Amplifier*. July 2016. URL: [http://cpm.uncc.edu/sites/cpm.uncc.edu/files/media/Explore\\_1.pdf](http://cpm.uncc.edu/sites/cpm.uncc.edu/files/media/Explore_1.pdf).



# Acknowledgements

First of all, I would like to thank my supervisor Dieter Süss for his continued support during all these years. Thank you for keeping your patience! I could certainly learn a lot from your positive way of approaching new challenges.

Next, I have to thank Hubert Brückl, who was my boss at the Austrian Institute of Technology (AIT), where most of the work presented in this thesis was carried out. Thank you for giving me the chance to start this project by providing an inspiring environment and also the monetary funding, as well as promoting the spirit of motivation in the team! From the Nano Systems team at AIT, I would like to further thank Rudi for all kinds of lab support, Tom for introducing me to almost all of the clean room equipment and microfabrication techniques, Volker for great team work on magnetic tunnel junction fabrication and Theo for his wise comments and anecdotes that made working long hours in the lab great fun. An atmosphere that science can be fun was also present in our office, which I shared with Philipp, Astrit and Moritz. You guys made me laugh more than once, and I was told everyone on the floor could hear that. Kerstin and Shweta, I also want to thank you for making the Nano Systems group a good place to work. To all Nanos, I am grateful for our shared experiences, after-work beers, barbecues and birthday parties.

From the group at the Institute of Solid State Physics at the Vienna University of Technology I want to mention Bernhard, Christoph, Flo, Tom and Markus. We had lively and humorous discussions, lots of fun and drinks as well as a few lessons to teach each other. I must not forget Barbara and the umbrella tent we slept in when camping in the snow on top of the Grand Canyon. What an unforgettable experience! Last but not least of the TU colleagues, I want to thank Claas, who I had the chance to get to know as both a gifted musician and physicist. Maybe because of these mutual interests, or maybe because you are a German in Austria, I sometimes had the feeling that you understood me best of all.

Finishing a PhD thesis is not always something enjoyable, and so I would now like to give my acknowledgements to the people, that were not directly part of my scientific life, but who definitely shared emotions and the ups and downs with me.

I would like to thank my parents Thomas and Waltraud for their financial support throughout my education and times of unemployment and my sister Linda for being an inspiration for trying new paths instead of always going straight ahead. I thank

my brother Simon for being supportive to my technical and musical interests as long as I can remember.

From my closest friends, I would like to mention especially Vali, Niamh and Tom representatively for the Wednesday-“Stammtisch”. You provided something constant and reliable in a time when I sometimes had the feeling of losing control over important areas of my professional and private life.

Being the only girl in the physics “boys’ club” most of the time, I cannot underestimate the support from my smart, open-minded and gorgeous female friends Manu, Elena and Alicia, which consisted in sharing our experiences and by being a leading example to each other. You are real role models for me and I am so glad I know you! I had the opportunity to be part of a wonderful band for the past two years, during which I came back from preparing for the entrance exam for the University of Music and Performing Arts to writing up my PhD thesis. Patrick, Luci, Raffaella, the core members of “They Call It Pi” and Matthias, my drummer queen, you were a source of self esteem and emotions that almost compensated the dissatisfaction of an unfinished PhD thesis.

Fabian, I thank you for teaching me object oriented programming and making my time in a big multinational company a rewarding and useful experience.

Mühei, I thank you for asking why I do not just grab your friend Stefan. Stefan, thank you for not running away. I did grab you in the first place, but you stayed with me in the second place. Thank you for being my main source of mental support during these really tough years. This makes you the toughest guy on earth I think. Coming to an end, I also want to mention two inspiring teachers, that I had the chance to meet. I understood very clearly during the past year when attending Prof. Dellago’s lecture at the Vienna University that simply good teaching can be a truly rewarding experience and how important it can be to sustain or reactivate the motivation to pursue a certain goal. And this brings me to acknowledging the excellent work my high school physics teacher Helmuth Mayr did in the first place. Being just so curious about science and technology without having honest trust in my math skills he could really foster my ambitions to pursue a career in science by just doing his job right. Good teaching opens up doors to people who are not naturally pushed into a certain field. Being taught by good teachers is a very fortunate and most importantly enabling experience. I am sure I can pass on some of this positive experience in whatever professional setting I will find myself in the future.

## Curriculum Vitae

Surname	Breth
Given names	Leoni Henrike
Address	Chimanistraße 34/5 1190 Vienna, Austria
E-Mail	leoni.breth@gmail.com
Mobile	+43 650 908 3796
Date of birth	Nov 16, 1984
Place of birth	Düsseldorf, Germany
Nationality	German

## Education

10/2009 - 06/2014 and 10/2015 - 10/2016	Doctoral studies in Technical Physics	Vienna University of Technol- ogy, TU Wien
10/2003 - 06/2009	Diploma studies in Technical Physics	Vienna University of Technol- ogy, TU Wien
02/2007 - 07/2007	term abroad	Poly-technical University of Perm', Russian Federation
09/1999 - 06/2003	high school	BG/BRG IV Wiedner Gürtel, Vienna

## Professional Experience

08/2014 - 08/2016	Software engineer	Robert Bosch AG, Vienna
11/2013 - 04/2014	Project assistant	Institute of Solid State Physics Vienna University of Technology
09/2009 - 08/2013	Research fellow	AIT Austrian Institute of Technology Health and Environment Department
07/2008 - 08/2008	Intern	AIT Austrian Institute of Technology Nanosystems group
10/2005 - 01/2007	Tutor	Institute of Solid State Physics Vienna University of Technology

## Publications

### Articles

- L. Breth, D. Suess, C. Vogler, B. Bergmair, M. Fuger, R. Heer, H. Brueckl: *Thermal switching field distribution of a single domain particle for field-dependent attempt frequency*, Journal of Applied Physics 112, 023903 (2012)
- L. Breth, T. Dimopoulos, J. Schotter, K. Rott, H. Brückl and D. Suess: *Fluxgate principle applied to a magnetic tunnel junction for weak magnetic field sensing*, IEEE Transactions on Magnetics 47, 1549 (2011)
- D. Suess, C. Vogler, C. Abert, F. Bruckner, R. Windl, L. Breth, and J. Fidler: *Fundamental limits in heat-assisted magnetic recording and methods to overcome it with exchange spring structures*, Journal of Applied Physics 117, 163913 (2015)
- T. Huber, B. Bergmair, C. Vogler, F. Bruckner, L. Breth, W. Hetaba, G. Hrkac and D. Suess: *Ultra-Low-Cost RFID Based on Soft Magnetic Ribbons*, IEEE Transactions on Magnetics 50, 1 (2014)
- D. Suess, L. Breth, J. Lee, M. Fuger, C. Vogler, F. Bruckner, B. Bergmair, T. Huber, J. Fidler and T. Schrefl: *Calculation of coercivity of magnetic nanostructures at finite temperatures*, Phys. Rev. B 84, 224421 (2011)

### Talks

- L. Breth, R. Heer and H. Brueckl: *Fluxgate magnetometer based on a tunnelling magnetoresistance element*, talk at Mikroelektroniktagung ME2012 (Best Paper Award), Vienna, April 23 - 24 2012
- L. Breth, D. Suess, C. Vogler, B. Bergmair, M. Fuger, R. Heer, H. Brueckl: *Switching of single-domain magnetic particles under the influence of thermal fluctuations*, talk at the Spring Meeting of the German Physics Association (DPG Frühjahrstagung) in Berlin, March 25 - 30 2012
- L. Breth, D. Suess, R. Heer, T. Dimopoulos, H. Brueckl: *Thermally assisted switching on intermediate timescales in magnetic tunnel junctions*, talk at the Magnetism and Magnetic Materials Conference (MMM) in Scottsdale (USA), Oct 30 – Nov 3 2011
- L. Breth, T. Dimopoulos, R. Heer, J. Schotter, K. Rott, D. Süss, H. Brueckl: *Noise characteristics of magnetoresistive fluxgates for weak magnetic field sensing*, talk

at the Spring Meeting of the German Physics Association (DPG Frühjahrstagung) in Dresden, March 13 - 18 2011

## Posters

- L. Breth, D. Suess, R. Heer, T. Dimopoulos, H. Brueckl: *Effect of thermally assisted switching in a tunneling magnetoresistance fluxgate sensor*, IEEE Magnetics Society Summer School in New Orleans (USA), May 22 - 27 2011
- L. Breth, D. Suess, T. Dimopoulos, J. Schotter, H. Brueckl: *Ultrasensitive magnetometer for biomedical applications*, NANOSSENS Meeting, Vienna, Dec 2 - 3 2010
- L. Breth, D. Suess, T. Dimopoulos, J. Schotter, H. Brueckl: *Fluxgate principle applied to a magnetic tunnel junction for weak magnetic field sensing*, Symposium on Magnetic Multilayers (MML) in Berkeley (USA), Sept 19 - 24 2010

## Participation in Workshops

02/25/2013 - 03/01/2013	Winter School "Phase stability and phase transitions in soft and hard materials", St. Christoph (Austria)
05/22 - 05/27/2011	IEEE Magnetics Society Summer School, New Orleans (USA)
02/02 - 02/06/2011	PhD seminar of the Austrian Institute of Technology "Advanced Scientific Presentation", Hirschegg (Austria)